POLITECNICO DI MILANO

Facoltà di Ingegneria dei Sistemi

Corso di Laurea Magistrale in Ingegneria Biomedica

Influence of Hydration on Mechanical Properties of Bone measured by Nanoindentation

Relatore

Prof. Pasquale VENA

Correlatore

Prof. Philippe ZYSSET

Tesi di Laurea Specialistica di

Tiziana SPAMPATTI

Matricola 765965

Anno Accademico 2011-2012

Twenty years from now you will be more disappointed by
the things that you didn't do than by the ones you did do.
So throw off the bowlines.
Sail away from the safe harbor.
Catch the trade winds in your sails.
Explore. Dream. Discover.

Mark Twain

Acknowledgments

First of all, I would like to express my deep gratitute to Prof. Pasquale Vena and Prof. Philippe K. Zysset, who gave me the opportunity to perform this thesis at ISTB.

Especially, I would like to thank my supervisor Jakob Schwiedrzik for his constant and insightful supervision, for his suggestions and for his help in all situations.

A grateful thought goes to all the people at the ISTB (Institute for Surgical Technology and Biomechanics, University of Bern, Switzerland), especially Marta, Livia, Marcelo, Risto, George and Weimin. for the moments we shared in these months

Grazie ai miei genitori, per aver creduto in me sin dal primo battito, sin dal primo respiro.

Grazie ai miei fratelli e ai miei nipoti: senza di voi la mia vita sarebbe infinitamente piú noiosa!

Grazie a mia nonna Maria, persona semplice e coraggiosa. Grazie ai nonni Andrea, Luigi e Silvia, che sono sicura mi guardano dal cielo e che oggi sono orgogliosi di me.

Grazie a Vanni, che mi ama per quella che sono e come tale mai mi sostituirebbe.

Grazie alle mie amiche storiche: Linda, Sara e Cristina. Ognuno di noi ha preso la propria strada, ma nonostante ció so che potró sempre contare su di voi, come ho fatto finora!

Grazie ai miei colleghi e compagni di avventura: Michela, Alice, Raffaella, Massimiliano, Chiara, Alessio e Valentina.

Grazie a tutti coloro che hanno deciso di essere una costante nella vita: gli amici piú cari.

Contents

List of Figures

List of Tables

Abstract

Bone is a mineralized tissue that serves a wide range of structural, metabolic and biological function, including supporting the body, protecting the vital organs, allowing movements, storing bone marrow and calcium. Bone shows complex hierarchical organization from the nanometer to the macroscopic scale. The hierarchical structure provides maximum strength with a minimum of material, and is known to adapt to the biological function of the bone by changing the arrangement of the components at different sizes. The complexity of bone's properties critically depends on the interplay between different structural levels: from the molecular/nanoscale interaction between crystallites of calcium phosphate and an organic framework, through the micrometer-scale assembly of collagen fibrils, to the millimeter-level organization of lamellar bone. Bone contains three main phase: mineral, collagen and water, tightly interconnected at the nanoscale. The mineral phase controls the bone stiffness, whereas the collagen contributes to its strength and toughness. Bound and unbound water contributes to elasticity and ductility.

The mechanical characterization of bone is of the highest importance in clinical medicine and the field of biomaterials. However, there is a paucity of information regarding the role of tissue mechanic in disease progression, tissue repair, and remodeling mechanisms associated with medical treatments. Nanoindentation has been widely used as a means to measure the micromechanical properties of bone since it allows testing small volumes and excludes the effects of large-scale porosity. Moreover, it has become an increasingly popular technique to study a wide range of viscoelastic materials such as biological tissue and polymers. Because of the viscoelastic nature of collagen fibers in the bone matrix, bone itself has remarkable viscoelasticity, which has been correlated also with hydration state and mineral content.

The most readily observed effect of viscoelasticity on indentation is creep, or a sinking of the tip into the sample under a constant load. The creep depth as a function of time can be fit to rheological models in order to determine parameters that describe the viscoelastic behavior. In addition, many commercial nanoindenters have a dynamic testing option, where sinusoidal loads can be applied to measure storage and loss moduli and allowing direct measurements of time-dependent properties.

All nanoindentation experiments were carried out with an Ultra Nano Hardness Tester (CSM Instruments SA, Switzerland) with ultra low thermal drift, equipped with acoustic damping enclosure so as to minimize instabilities due to the ambient background noise. At any scale, the mechanical response of bone depends heavily on extrinsic factors that include preparation techniques, hydration state, and mechanical test type and tip shape. Bone specimens were obtained from the midshaft of one bovine femur (24 months old) without bone disease. In order to keep the samples in as close to physiological conditions as possible, they were kept hydrated throughout the preparation steps. In fact, the water content of bone ($10 \div 20\%$) plays an important role in determining its mechanical properties. All bone specimens were embedded in polymethylmethacrylate, which didn't reasonably infiltrated the bone tissue. Moreover, the sample preparation was performed without chemicals for cleaning and dehydration. In this way the mechanical properties of the microstructural features were kept as natural as possible. The sample surface was smoothed with an ultramiller system, while the polishing was avoided because it was found to introduce cracks in the bone surface. After milling, the specimens were not freeze again and they were not tested after being absorbed in saline solution for more than 15 hours. Axial and transverse specimens were cut from the bovine femur, but an optimized preparation protocol could not be found for the latter ones. It was therefore decided to focus on axial specimens. The dry and the wet specimens followed the same preparation procedure, but the former ones were then left air-drying in room conditions for 48 hours before testing. For hydrated nanoindentation tests, a fluid cell was used to keep the specimen submerged in a saline solution. However, specialized tips with long shafts were required and data acquisition was complicated by meniscus forces acting on the indenter. Two different indenter geometries were employed in the present study: Berkovich and spherical. Berkovich tips are "sharp" and cause significant plastic deformation at the onset of indentation due to the stress concentration near the material's surface. The spherical indenters are used to minimize plastic deformation and stress concentrations and avoid damaging the sample. Two kinds of configurations were tested: dry and wet indentations. Four sets of experiments have been carried out for each

configuration and the load-displacement curves have been acquired in load control mode. The first protocol employed a trapezoidal load history with a 30 s holding time at each peak load. Three different penetration depths have been explored: 1000, 1500 and 2000 nm with Berkovich tip, and 500, 750 and 1000 nm with spherical tip. In the five step procedure (protocol n°2), the indenter tip was loaded at each mean peak load calculated in the first set of experiments. A first 30 s holding phase at maximum load was followed by a second holding phase at 10% of this load. The third set of experiment used the DMA mode at 5, 25 and 50 Hz. The peak load was fixed to 50 000 µN for the Berkovich tip and to 80 000 µN for the spherical tip, and the sinus amplitude was set to the 10% of the peak load. The fourth protocol is called progressive multi-cycle because the indenter tip in incrementally loaded and unloaded into the bone over a preselected (7) number of intervals. At each maximum and minimum load level, a 30 s holding phase was included.

All indentation locations were selected within plexiform regions and with a 50 000 µm spacing using instrument's internal microscope.

From analysis of the indentation load-displacement curves, values of indentation modulus and hardness of the material can be derived using well-established equations based on elastic contact theory. Following the method of Oliver and Pharr [Oliver and Pharr, 1992], the 60% of the unloading curve was fitted with Python to a power function, which was then differentiated and evaluated at maximum displacement to determine the stiffness S. The contact area A is function of the contact depth and was determined through the use of an empirically derived indenter area function. The hardness H_{IT} and the reduced modulus E_r, follow from:

$$H_{IT} = \frac{P_{max}}{A}$$

and

$$E_r = \frac{\sqrt{\pi}}{2\beta}\frac{S}{\sqrt{A}}$$

where β is an indenter geometry-dependent constant. E_r is the result of combined elastic displacement of tested surface and indenter, so the indentation modulus E_{IT} follows from:

$$\frac{1}{E_r} = \frac{1}{E_{IT}} + \frac{1-\nu_i^2}{E_i}$$

where E_i (= 1141 GPa) and ν_i (= 0,07) are the Young's modulus and the Poisson's ratio of the diamond indenter. Indentation modulus and hardness were calculated in experimental set°1, 2 and 4. The ratio between the elastic

work and the total work was calculated from each P-h curve of those experimental sets. In the first set of experiments, two different analysis have been used to examine indentation with a standard linear solid model for a Berkovich and a spherical indenter. The viscoelastic solution derived by Vandamme and Ulm [Vandamme and Ulm, 2006] was employed for the Berkovich indenter, which is assimilated to a conical indenter of equivalent cone angle $\theta = 70.32°$. Whereas, the indentation of bone by a spherical tip was analyzed using the solution derived by Cheng et al. [Cheng et al., 2005]. The input parameters were the instantaneous elastic modulus E_1, which was assumed equal to the Young's modulus of the material, and the two Poisson's ratio ν_1 and ν_2, which were assumed equal to 0,3 and 0,5 respectively. The delayed elastic parameters, E_2 and η, were identified by fitting the holding response of the indentation test to the viscoelastic solutions mentioned above. In experimental set n°2 and 4, creep and recovery distances were measured as the change in depth of the indenter during the holding times at maximum and minimum load respectively. In case of DMA measurements, the dynamic mechanical analysis allows for a continuous acquisition of hardness, indentation modulus, storage and loss modulus data as a function of indentation depth.

The sample surface roughness after the final preparation protocol was checked with an Atomic Force Microscope. Moreover, after experiments, each bone sample surface was observed with help of optical microscopes at 5x and 100x magnification. Mean and standard deviations of each parameter calculated have been plotted as a function of the penetration depth. The results of the first two experimental set were compared using two-way ANOVA performed with R.

The penetration depths of 1000-2000 nm explored with the Berkovich tip correspond to a contact diameter of $\approx$ 6-11 µm, while the penetration depths of 500-1000 nm explored with the spherical tip correspond to a contact diameter of $\approx$ 14-20 µm. Thus, in the present study, the length scale probed is comparable with the size of one or more lamellae in a osteon (an average lamellar layer is between 3 and 7 µm), but the material properties reported at these specific penetration depths reflect the average material response from the initial point of contact down to the specific depth reported. Penetration depths lower than $\approx$ 500 nm were not explored due to the great influence of the surface roughness on the properties measured.

A constant value of E_{IT} with depth is expected for homogeneous elastic solid, but not for bone which has a intricate hierarchical structure. Significant differences of E_{IT} in dry and wet conditions were found in all the experimental set. For the Berkovich tip, E_{IT} ranged from 22 to 26 GPa in dry conditions, and from 15 to 20 GPa in wet conditions. The percentage difference between the results in dry and wet conditions was equal to

$\approx$ 36% at low penetration depth and it fell to $\approx$ 20% while increasing the depth. For the spherical tip, E_{IT} showed significantly lower values, it ranged from 13 to 16 GPa in dry conditions, and from 9 to 14 GPa in wet conditions. The percentage difference showed the same trend as in the previous case. At low penetration depth E_{IT} of the wet bone was $\approx$ 30% lower than the dry conditions, but it was $\approx$ 6% higher at 1000 nm depth. The change in the indentation modulus between wet and dry samples can be explained by the replacement of the weak hydrogen bonds with stronger inter-peptide bonds during dehydration. Moreover, the fact that the wet measurements presented lower force than their dry counter parts to reach the same penetration depth suggests a higher compliance for the former condition. An higher indentation modulus and hardness might also be partially explained by a greater degree of mineralization, which provides a rigid scaffold and prevents the collagen fibrils from contracting. For bone sample in liquid environment, mineral may be lost from the near-surface region. Nanoindentation is a surface-sensitive technique and this demineralization would result in a reduced elastic modulus and a more viscoelastic response from this region. Hardness values demonstrated trends comparable to indentation modulus in each test protocol. For both the indenter tips, the difference between dry and wet condition decreased from 62% to 24% while increasing the penetration depth. For the Berkovich tip, the mean H_{IT} values were found to be between 820 and 1000 MPa in dry conditions, and between 380 and 670 MPa in wet conditions. For the spherical tip, the mean H_{IT} values ranged from 230 to 350 MPa in dry conditions, and between 90 to 230 MPa in wet conditions. The E_{IT}/H_{IT} ratio is a quantitative measure of the relationship between a material's plastic and elastic deformation behavior. At higher penetration depths greater permanent deformations were observed, even if the spherical indenter produced smaller plastic deformations than the Berkovich tip. The ratio E_{IT}/H_{IT} was higher in dry state than in wet conditions, and this means the the wet bone was more affected by viscoelastic recovery.

Concerning the results for the viscoelastic analytical solutions, the hydration condition was the highly significant factor for all the parameters calculated. The elastic moduli and the viscosity were found to be higher in dry conditions, and the instantaneous elastic modulus was greater than the corresponding delayed elastic modulus. These results reflected a more significant time-dependent behavior of wet bone. However, all the differences reduced while increasing the penetration depth, suggesting a gain of plastic effects. In particular, the viscosity in wet conditions was found to be very small, thus the material response was mainly elastic.

Unfortunately, it hasn't been possible to analyze the storage and loss moduli from the DMA mode due to an internal error of the model imple-

mented in the software. Negative values of loss moduli were provided at each frequency and penetration depth, and this has no physical meaning.

The ratio W_{el}/W_{tot} is a measure of the reversible elastic contribution to the total work. This ratio ranged from 44 to 50% for the spherical indenter tip, and from 25 to 29% for the Berkovich tip. The results for the spherical tip was significantly influenced by the penetration depth, but not by the hydration condition. At higher contact depth, the spherical indent exhibited more plastic deformation. On the contrary, the hydration condition was found to be an highly significant factor for the Berkovich tip, and wet bone exhibited a ratio W_{el}/W_{tot} 10% higher than in dry conditions.

Creep and recovery are forms of time-dependent viscoelastic deformation. These factor were seen to be highly influenced by both the penetration depth and the hydration state. In dry conditions the recovery distance was lower than the corresponding creep distance at each indentation depth, while it was the opposite in wet conditions. This results agree with the greater viscoelastic behavior in wet bone.

It is suggested that nanoindentation in physiological conditions gives a better estimate of the mechanical properties of the microstructural components of bone in vivo rather than nanoindentation under conventional conditions.

This study investigated the effects of hydration on bone's properties using two different indenter shapes. The importance of bone viscoelasticity in physiological condition has been pointed out and it could help to further improve the understanding of the mechanical properties of bone.

Sommario

Il tessuto osso é un tessuto connettivo mineralizzato con importanti funzioni strutturali, metaboliche e biologiche, tra cui sostenere del corpo, proteggere organi vitali, permettere il movimento e fornire una riserva di midollo osseo e di calcio. L'osso possiede una complessa organizzazione gerarchica dal livello della nanoscala fino alla macroscala. Tale struttura gerarchica fornisce la massima resistenza con l'impiego della minore quantitá possibile di materiale ed é inoltre in grado di adattarsi continuamente alla funzione biologica richiesta variando la disposizione dei suoi costituenti ad ogni livello di scala. La complessitá delle proprietá ossee é strettamente legata alle influenze reciproche tra i vari livelli di scala: dalla nanoscala con le interazioni molecolari tra i cristalli di fosfato di calcio e le componenti organiche, attraverso l'assemblaggio delle fibrille di collagene alla scala micrometrica, fino all'organizzazione in osso lamellare a livello millimetrico. Il tessuto osseo é composto da tre costituenti essenziali strettamente interconnessi alla nanoscala: i minerali, il collagene e l'acqua. La fase minerale é responsabile della rigidezza dell'osso, il collagene contribuisce in modo significativo alla sua tenacitá e resistenza, mentre l'acqua fornisce elasticitá e duttilitá.

La caratterizzazione meccanica dell'osso é di estrema importanza per la medicina clinica e per il campo dei biomateriali. C'é, tuttavia, un'insufficienza di informazioni riguardanti il ruolo meccanico del tessuto osseo nello sviluppo di patologie, nel riparo tessutale, e nei meccanismi di rimodellamento associati con i trattamenti medici. La tecnica della nanoindentazione é stata largamente utilizzata come strumento per stimare le proprietá meccaniche dell'osso, tale tecnica permette, infatti, di investigare ridotti volumi di materiale, escludendo cosí gli effetti della porositá (ad eccezione di quella nanometrica). La nanoindentazione sta inoltre diventando sempre piú popolare

per studiare numerosi materiali viscoelastici come i polimeri e vari tessuti biologici. L'osso possiede notevoli proprietá viscoelastiche che sono state associate sia alla natura viscoelastica delle fibre di collagene presenti nella matrice ossea, sia al contenuto di minerali e all'idratazione. Il piú evidente effetto associato alla viscoelasticitá é il creep, che si manifesta come un continuo affondamento della punta dell'indentatore quando le viene applicato un carico costante. L'andamento della penetrazione in funzione del tempo puó essere interpolato con l'utilizzo di modelli reologici per estrarne parametri che descrivano il comportamento viscoelastico. Numerosi nanoindentatori sono inoltre in grado di effettuare test dinamici applicando un carico sinusoidale e fornendo direttamente i valori di "storage" e "loss" moduli.

Nel presente lavoro, tutte le prove di nanoindentazione sono state effettuate utilizzando un Ultra Nanoindentatore (CSM Instruments SA, Svizzera), con elevata stabilitá termica ed equipaggiato con una cabina d'isolamento acustico per minimizzare ogni instabilitá dovuta al rumore ambientale. Ad ogni livello di scala osservata, la risposta meccanica dell'osso é fortemente influenzata da una serie di fattori tra cui: le tecniche di preparazione dei campioni, il livello di idratazione, il protocollo di prova e la geometria della punta dell'indentatore. I campioni ossei utilizzati nel presente lavoro sono stati ottenuti dal tessuto osseo corticale della diafisi femorale proveniente da un bovino sano di 24 mesi. Per discostarsi il meno possibile dalle condizioni fisiologiche, i campioni sono stati mantenuti idratati attraverso tutti i passaggi previsti dal protocollo di preparazione. Il contenuto d'acqua del tessuto osseo ($10 \pm 20\%$) svolge un ruolo rilevante nel determinarne le proprietá meccaniche. I campioni ossei sono stati incastonati in polimetilmetacrilato ad elevata viscositá, che quindi non si é significativamente infiltrato nel tessuto osseo. La preparazione dei campioni é stata inoltre effettuata senza l'utilizzo di prodotti chimici, cosicché tutte le caratteristiche della microstruttura sono state mantenute nello stato piú naturale possibile. La superficie dei campioni é stata lisciata con un sistema di ultrafresatura. La procedura di lucidatura é stata evitata perché causa della formazione di micro-fratture nella superficie ossea. Dopo essere stati fresati, i campioni non sono stati congelati nuovamente, ma sono stati immediatamente testati. Nessuna prova di nanoindentazione é stata effettuata su campioni lasciati immersi nella soluzione salina per piú di 15 ore. Dal femore bovino sono stati tagliati sia campioni assiali che traversali, tuttavia per questi ultimi non é stato possibile determinare un protocollo di preparazione ottimale. Tutte le analisi si sono quindi concentrate sui campioni assiali. I campioni idratati e secchi sono stati sottoposti alla stessa procedura di preparazione, al termine della quale i secondi sono stati lasciati asciugare a temperatura ambiente per 48 ore. Per effettuare prove di nanoindentazione sui campioni idratati, una cella liquida é stata utilizzata in

modo da mantenere i campioni sempre immersi nella soluzione salina. Specifiche punte con supporti piú lunghi sono richieste e l'acquisizione dei dati viene complicata dalla presenza di un menisco che da origine a forze agenti sull'indentatore. Due punte con differenti geometrie sono state impiegate: l'indentatore di Berkovich e l'indentatore sferico. Il primo tipo di indentatore é appuntito e provoca importanti deformazioni plastiche anche a basso carico a causa di una concentrazione di sforzi. Il nanoindentatore sferico, invece, minimizza le deformazioni plastiche e la concentrazione di sforzi, evitando cosí ogni di danneggiare il campione. Le prove sperimentali sono state effettuate in due diverse configurazioni: in ambiente asciutto e in presenza di liquido. Quattro diverse serie sperimentali sono state realizzate per ogni configurazione e tutte le curve carico-penetrazione (P-h) sono state ricavate in controllo di carico. Il primo protocollo consisteva in una curva di carico trapezoidale con un tempo di hold di 30 s. Tre diverse profonditá sono state esplorate per ogni indentatore: 1000, 1500 e 2000 nm per la punta di Berkovich, e 500, 750 e 1000 nm per quella sferica. Il secondo protocollo é chiamato "a cinque step". L'indentatore viene caricato fino ad un carico massimo calcolato come media dalla prima serie sperimentale, dopo un tempo di hold di 30 s viene scaricato fino al 10% del carico massimo, a cui segue un ulteriore periodo di hold. Nella terza serie sperimentale viene utilizzata la modalitá DMA del nanoindentatore con tre diverse frequenze: 5, 25 e 50 Hz. Il carico massimo é stato fissato a 50 000 µN per la punta Berkovich e 80 000 µN per quella sferica, mentre l'ampiezza dell'oscillazione é stata impostata al 10% del carico massimo. L'ultimo protocollo ha previsto l'applicazione di carichi progressivamente crescenti nello stesso sito d'indentazione per 7 diversi livelli di forza. Un periodo di hold di 30 s é stato applicato sia ai massimi carichi, sia ai minimi.

Tutti i punti da sottoporre a nanoindentazione sono stati accuratamente selezionati all'interno delle regioni plessiformi del tessuto osseo attraverso il microscopio ottico montato sull'Ultra Nanoindentatore. Tra le diverse posizioni scelte é stata lasciata una distanza minima di 50 000 µm.

I valori del modulo di indentazione e della durezza sono stati calcolati dalle curve P-h attraverso un'equazione ampiamente utilizzata basata sulla teoria di Hertz e riguardante il contatto dei solidi elastici [Hertz, 1896]. Applicando il metodo proposto da Oliver e Pharr [Oliver and Pharr, 1992], il 60% della porzione di scarico della curva P-h é stata interpolata attraverso Python con una funzione di potenza, questa é poi stata differenziata e risolta nel punto di massima penetrazione per determinare la rigidezza S. L'area di contatto é invece funzione della profonditá ed é stata valutata attraverso l'utilizzo di funzioni derivate empiricamente per ogni geometria dell'indentatore. La durezza H e il modulo ridotto E_r sono stati calcolati dalle seguenti formule:

$$H = \frac{P_{max}}{A}$$

e

$$E_r = \frac{\sqrt{\pi}}{2\beta}\frac{S}{\sqrt{A}}$$

in cui β é una costante dipendente dalla geometria dell'indentatore. E_r contiene informazioni riguardanti non solo la deformazione del campione, ma anche quella dell'indentatore, quindi il modulo di indentazione E_{IT} puó essere ricavato da:

$$\frac{1}{E_r} = \frac{1}{E_{IT}} + \frac{1-\nu_i^2}{E_i}$$

in cui E_i (= 1141 GPa) e ν_i (= 0,07) sono il modulo di Young e il modulo di Poisson della punta del nanoindentatore costituita di diamante. Il modulo di Young e la durezza sono calcolati seguendo questa procedura nelle serie sperimentali n°1, 2 e 4. Nelle stesse serie, il rapporto tra il lavoro elastico e il lavoro totale é calcolato da integrazioni dell'area sottesa alle curve P-h. Nel primo protocollo sperimentale sono state inoltre implementate due diverse analisi per studiare le indentazioni attraverso il modello reologico del solido lineare standard (SLS). La soluzione viscoelastica studiata da Vandamme e Ulm [Vandamme and Ulm, 2006] é stata applicata per le indentazioni con la punta Berkovich, questa puó essere infatti assimilata ad una punta conica con angolo di cono $\theta = 70.32°$. La soluzione viscoelastica di Cheng [Cheng et al., 2005] é stata invece utilizzata per studiare le indentazioni effettuate con la punta sferica. Per ambedue i modelli i parametri di input sono stati il modulo elastico istantaneo E_1, assunto uguale al modulo di Young, e i due moduli di Poisson ν_1 e ν_2, assunti pari rispettivamente a 0,3 e 0,5. I parametri che esprimono il ritardo del comportamento, E_2 e η, sono stati calcolati attraverso il fitting della risposta del materiale durante il tempo di hold. Nei protocolli sperimentali 2 e 3, creep e recovery sono stati calcolati come la variazione di penetrazione dell'indentatore durante i periodi di hold ai carichi massimi e minimi rispettivamente. Per quanto riguarda le misure effettuate in modalitá DMA, l'analisi in modo dinamico restituisce la durezza, il modulo elastico, e "storage" e "loss" moduli in funzione della profonditá.

La rugositá superficiale dei campioni é stata controllata dopo la procedura di preparazione attraverso un microscopio a forza atomica. Due microscopi ottici con ingrandimenti 5x e 100x sono stati invece utilizzati al termine di ogni serie di prove per osservare le regioni indentate e la condizione della superficie del campione. Il valor medio e la deviazione standard di tutti i

valori calcolati sono stati rappresentati in grafici in funzione della profonditá di penetrazione. Le analisi statistiche sono state effettuate in R utilizzando la funzione per l'analisi della varianza a due vie (ANOVA a due vie).

Le profonditá 1000-2000 nm esplorate con la punta Berkovich, corrispondono a contatti di diametro $\approx$ 6-11 µm, mentre per quanto riguarda la punta sferica, le profonditá 500-1000 nm corrispondono a contatti di diametro $\approx$ 14-20 µm. Di conseguenza, nel presente lavoro le dimensioni delle aree di contatto sono confrontabili alla dimensione di una o piú lamelle (il loro spessore medio é infatti compreso tra 3 e 7 µm), ma le proprietá del materiale ad una specifica profonditá corrispondono a una risposta media del materiale dal punto d'inizio del contatto, fino alla profonditá massima. Non sono state effettuate prove a profonditá inferiori a circa 500 nm a causa dell'elevata influenza che la rugositá superficiale ha sui parametri calcolati.

Il valore di E_{IT} dovrebbe essere costante nei materiali omogenei ed elastici, ma questo non é evidentemente il caso del tessuto osseo che possiede una complicata struttura gerarchica. In tutte le serie sperimentali tra campioni ossei idratati e secchi sono state riscontrate notevoli differenze nel valore E_{IT}. Per i risultati ottenuti con la punta Berkovich, E_{IT} é stato osservato variare tra 22 e 26 GPa in condizioni asciutte, e tra 15 e 20 GPa in presenza di liquido. La differenza percentuale tra i valori di E_{IT} nei due stati é quindi di circa 36% a basse profonditá e circa 20% aumentando la profonditá. Per quanto riguarda la punta sferica, E_{IT} ha mostrato valori notevolmente inferiori al caso precedente, E_{IT} infatti varia tra 13 e 16 GPa in asciutto, e tra 9 e 14 GPa per campioni idratati. A basse profonditá E_{IT} é maggiore di circa il 30% per campioni asciutti, ma a 1000 nm il valore di E_{IT} dei campioni umidi supera quello dei campioni asciutti di circa il 6%. La differenza del modulo di indentazione dei campioni nelle due diverse condizioni di idratazione puó essere spiegata assumendo che la deidratazione porti ad una sostituzione dei deboli ponti idrogeno con legami peptidici molto piú forti. Una maggiore compliance dei campioni umidi é invece suggerita dall'osservazione che in tali campioni le profonditá prestabilite sono state raggiunte applicando un carico inferiore che nei campioni asciutti. Modulo di indentazione e durezza elevati possono anche essere correlati ad un maggiore grado di mineralizzazione, che fornisce una struttura rigida ed evita la contrazione delle fibrille di collagene. Particelle minerali possono staccarsi dalle regioni vicino alla superficie dell'osso quando questo é immerso in un liquido. La tecnica di nanoindentazione é sensibile alla superficie e tale demineralizzazione potrebbe portare ad una riduzione del modulo elastico calcolato e ad una maggiore risposta viscoelastica. In ogni serie di prova, i valori di durezza hanno mostrato andamenti confrontabili a quelli del modulo di indentazione. Per entrambe le geometrie dell'indentatore, la differenza tra le due condizioni di idratazione é aumen-

tata dal 62% al 24% aumentando la profonditá. Per la punta Berkovich, il valor medio di H varia tra 820 e 1000 MPa in condizioni asciutte, e tra 380 e 670 MPa in condizioni idratate. Per la punta sferica, lo stesso valore varia tra 230 e 350 MPa, e tra 90 to 230 MPa rispettivamente per campioni secchi e umidi. Il rapporto E_{IT}/H_{IT} é una misura della relazione tra il comportamento plastico ed elastico del materiale. Ad elevate profonditá sono state osservate maggiori deformazioni plastiche anche per l'indentatore sferico, che ha comunque dimostrato un comportamento plastico inferiore all'indentatore di Berkovich. Il rapporto E_{IT}/H_{IT} é stato osservato essere piú elevato per campioni idratati, che significa un maggiore recovery viscoelastico.

Per quanto riguarda i risultati ottenuti applicando le due soluzioni analitiche viscoelastiche, lo stato di idratazione é stato trovato essere il fattore piú significativo per tutti i parametri calcolati. I moduli elastici e la viscositá piú elevati si sono osservati in condizioni asciutte, inoltre il valore del modulo elastico istantaneo E_1 é sempre stato maggiore di quello del corrispondente modulo elastico E_2. Questi risultati riflettono un piú elevato comportamento tempo-dipendente del tessuto osseo idratato. Ad ogni modo, é stato notato che tutte queste differenze si affievoliscono aumentando la profonditá di penetrazione, suggerendo un'acquisizione di importanza di fenomeni di carattere plastico. In condizioni idratate, sono stati trovati valori di viscositá molto bassi, suggerendo una risposta del materiale di carattere prevalentemente elastico.

Non é stato, purtroppo, possibile analizzare "storage" e "loss" moduli calcolati in modalitá DMA a causa in un errore nel modello implementato dal software del nanoindentatore. Sono stati infatti forniti valori del "loss" modulo negativi che non hanno alcun significato fisico.

Il rapporto W_{el}/W_{tot} é una misura del contributo elastico al lavoro totale. Tale rapporto é stato osservato variare tra il 44 e 50% utilizzando una punta sferica, e tra il 25 e 29% utilizzando una punta Berkovich. I risultati utilizzando il primo tipo di punta sono stati significativamente influenzati dalla profonditá di penetrazione, ma non dallo stato di idratazione. Come aspettato, alle profonditá piú elevate la punta sferica ha causato maggiore deformazione plastica. Al contrario, lo stato di idratazione é stato un fattore di significativa importanza per quanto riguarda le prove di indentazione con la punta Berkovich, infatti il rapporto W_{el}/W_{tot} delle prove in condizioni umide é 10% di quello in condizioni asciutte.

Creep e recovery sono forme di deformazioni viscoelastiche. Questi fattori sono stati fortemente influenzati sia dalla profonditá di penetrazione che dalla condizione di idratazione. Nelle prove condotte su campioni asciutti, il recovery é stato inferiore al corrispondente creep, mentre il risultato opposto é stato osservato per i campioni umidi. Ancora una volta questi risultati

mostrano il piú elevato comportamento viscoelastico del tessuto osseo umido.

Il presente lavoro ha studiato l'influenza dell'idratazione sulle proprietá del tessuto osseo attraverso prove di indentazione con due punte di differente geometria. É stata evidenziata l'importanza della viscoelasticitá nel tessuto osseo e ció puó essere un punto di partenza per approfondire la conoscenza delle proprietá meccaniche e del comportamento di tale tessuto.

CHAPTER 1

Introduction

1.1 Function of bone

Bone is a mineralized tissue that serves a wide range of structural, metabolic and biological functions. Its structural properties include providing support for the body against gravity, protecting vital internal organs, storing bone marrow, and assisting in movement and locomotion serving point of attachment for most skeletal muscles. The primary metabolic function of the bone lies in its ability to serve as mineral storage, including calcium, which is necessary for nerve conduction, muscle contraction, clot formation, and cell secretion [Cowin, 1989].

Throughout life it undergoes processes associated with growth and reshaping in childhood and adolescence, called bone modeling, and lifelong process whereby skeletal tissue is continuously being resorbed and replaced in order to maintain skeletal integrity, called remodeling. The maintenance of a normal, healthy skeletal mass depends on interactions between osteoblasts (bone forming cells), osteoclasts (bone eating cells) and constituents of the bone matrix to keep the processes of bone resorption and formation in balance [Parsamian and Norman, 2001].

1.2 Bone composition and structure

Use of the terms mineralized and calcified arises from the fact that, in addition to the principle protein, collagen, and other proteins, glycoproteins,

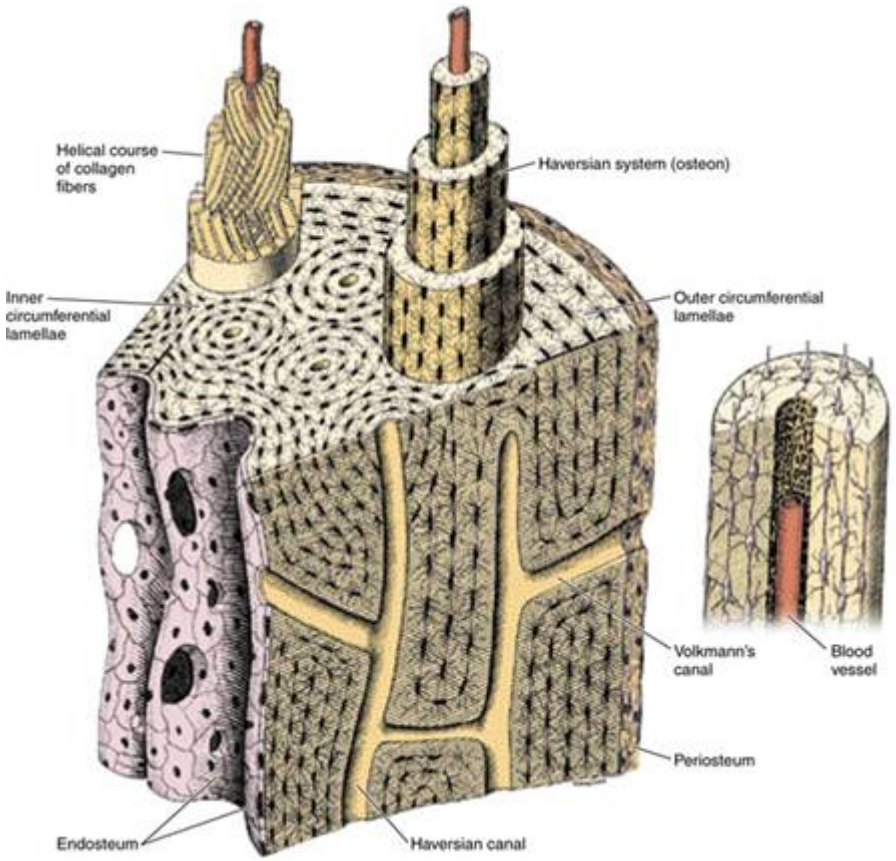

Figure 1.1: Sectioned cortical bone showing the tubular and circumferential arrangement of osteon. In the center of each osteon is a canal, called the Haversian canal. Each Haversian canal contains blood vessels, nerve endings and lymphatic vessels [Khurana, 2009].

and protein-polysaccherides, comprising about 50% of the volume, the major constituent of bone is a calcium phosphate (thus the term calcified) in the form of a crystalline carbonate apatite (thus the term mineralized) [Bronzino, 2000].

Bone is self-assembling, self-maintaining and self-repairing. Through cellular activities, bone adapts to alteration in mechanical loading by changing its shape and size [Oyen, 2011].

Bone is a multihierarchical, heterogeneous, and anisotropic hard tissue, in which the primary constituents are collagen fibers and hydroxyapatite (HA)-like mineral crystals [Franzoso and Zysset, 2009]. The hierarchical structure provides maximum strength with a minimum of material, and is known to adapt to the biological function of the bone by changing the arrangement of

the components at different sizes. The variability at the nanometer level is in the shape and size of mineral particles, at the micron level in the arrangement of mineralized collagen fibres into lamellar structures and beyond in the inner architecture, the porosity and the shape of the bone. While its structure is extremely complex and variable, its basic building block, the mineralized collagen fibril, is rather universal. It consists of staggered arrays of collagen molecules reinforced by nanometer sized mineral platelets. The mechanical properties of bone depends strongly on all these parameters [Fratzl, 2004, Fratzl and Gupta, 2007].

1.2.1 The types of bone tissue

Bone has a hierarchical structure that requires interpretation of mechanical behaviour at multiple length-scale. At macroscopic length-scales, one can readily see that bone exists in different shapes and sizes.

At the macrostructural level there are two major architectural structures of bone tissue, called cortical bone and cancellous bone. It is important to note that the material and structural organization of collagen-apatite crystallites making up compact bone are the same as the material forming cancellous bone. The location of these bone types in a femur is illustrated in Figure 1.2. The external surface of bone is smooth and is called the periosteal surface or periosteum. The periosteum is a specialized membrane, a layered and highly vascularized structure, covering most of the external surface of a bone. It consists of an outer dense layer of collagenous fibers and fibroblasts. This relatively impermeable fiber stocking is attached to the exterior surface of bone and is always under tension. The longitudinal central tubular passage in a long bone is called the medullary canal. The surface of this canal is called the endosteal surface or the endosteum and it is mainly a cell layer. The diaphysal region of a long bone is the midshaft and the epiphysial regions are the ends of the bone. The flared regions in between are called the metaphysial regions [Cowin and Doty, 2007].

Cortical *vs.* Cancellous bone

Cortical bone is found primarily in the shaft of long bones and the outer shell around cancellous bone at the proximal and distal ends of bones and the vertebrae, whereas cancellous bone is located within the cortical tissue, in medullary cavities at the ends of long bones, and in the interior of short bones, such as spinal vertebrae [Wang et al., 2010].

Cancellous bone represents the 20% of the total skeleton mass and it has a porosity in the range of 45–95%, while cortical bone accounts for the

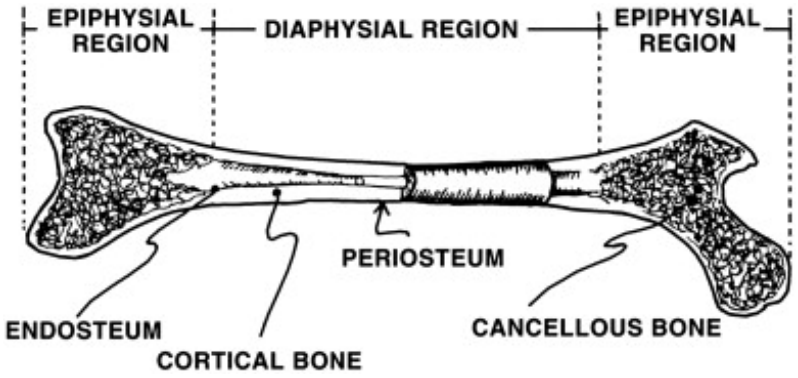

Figure 1.2: Longitudinal section of the femur illustrating cancellous and cortical bone types.The diaphysis (shaft) of a long bone contains a large marrow cavity surrounded by thick-walled tube of cortical bone. The proximal and distal ends, or epiphyses, of the long bone consist of cancellous bone with a thin outer shell of compact bone. The outer surface of the bone is covered by a fibrous layer of connective tissue called periosteum [Cowin and Doty, 2007].

remaining 80% of skeleton mass and possesses a small porosity (5–10%). It is important to remember that bone is a dynamic porous structure: its porosity may change as the result of a pathologic condition or in a normal adaptive response to a mechanical or physiologic stimulus. Trabecular bone may become more compact, or compact bone may become more porous. Such changes strongly affect bone's mechanical properties [Cowin, 1989].

In cortical (compact) bone, several complex cylindrical structures called osteons (or Haversian systems) are mixed with interstitial bone (Figure 1.3). Osteons look like cylinders of about 200–250 μm in diameter running roughly parallel to the long axis of the bone. Two kinds of osteons can be recognized: primary and secondary. Primary osteons are structures formed around blood vessels in the initial growing phase of bone. Secondary osteons form after remodeling. During this process, bone cells first excavate a tubular path through the hard tissue, and then deposit the osteon layer by layer. Interstitial tissue is that between osteons. Depending on the amount of remodeling that has occurred, the interstitial tissue may be a mixture of primary bone or the remnants of primary and secondary osteons [Cowin, 1989, Cowin, 1999, Cowin and Doty, 2007, Martin et al., 1998].

Cortical bone is much denser than cancellous bone, and therefore it has a less concentration of blood vessels. The porosity of cortical bone is mostly contributed by Haversian canals, Volkmann canals and resorption cavities.

- Haversian canals are approximately aligned to the long axis of the bone,

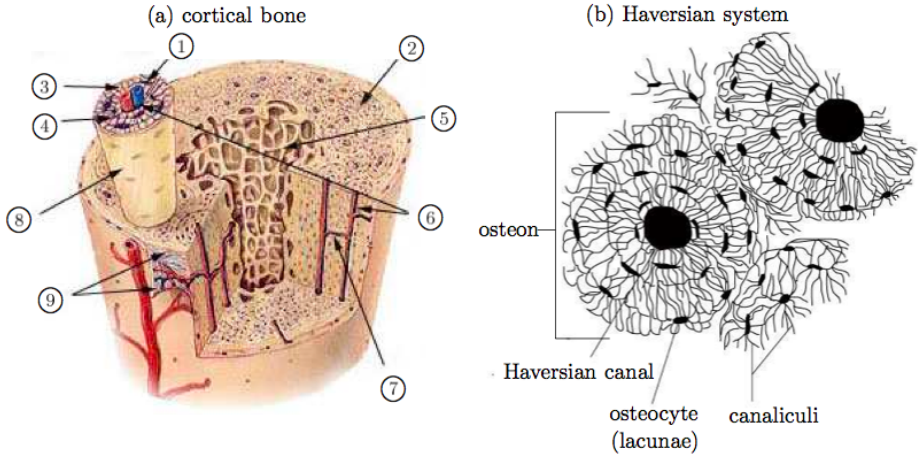

Figure 1.3: (a) a graphical sketch of cortical bone hosting osteons: 1. Lacunae containing osteocytes, 2. Osteon of compact bone, 3. Lamellae, 4. Canaliculi, 5. Trabeculae of spongy bone, 6. Haversian canal, 7. Volksmann canal, 8. Osteon, 9. Periosteum. (b) on a smaller observation scale, the Haversian system, containing osteocytes embedded in lacunae interconnected via canaliculi [Scheiner et al., 2010].

contain capillaries and nerves, and are about 50 μm in diameter.

- Volkmann canals are short, transverse canals connecting Haversian canals to each other and to the outside surfaces of the bone. These canals also contain blood vessels and nerves.

- Resorption cavities are the temporary spaces created by bone-removing cells (osteoclasts) in the initial stage of bone remodeling.

Cancellous bone generally exists only within the confines of the cortical bone coverings. Cancellous bone is also called trabecular and spongy bone, because it is composed of short interconnected struts of bone called trabeculae which give its a spongy appearance. Due to his high porosity, it is lighter and less dense than compact bone, has vast surface area and allows a higher concentration of blood vessels and bone marrow. The pores are interconnected and their diameter may be from few micrometers to millimeters (Figure 1.4). The millimeter-sized spaces in between trabeculae house bone marrow and are much more metabolically active than cortical bone due to their high surface-to-volume ratio. Trabeculae are organized to provide maximum strength, they follow the lines of principal stress and can realign if the direction of stress changes [Wolff, 1986, Murugan and Ramakrishna, 2005, Rho et al., 1998, Wang et al., 2010].

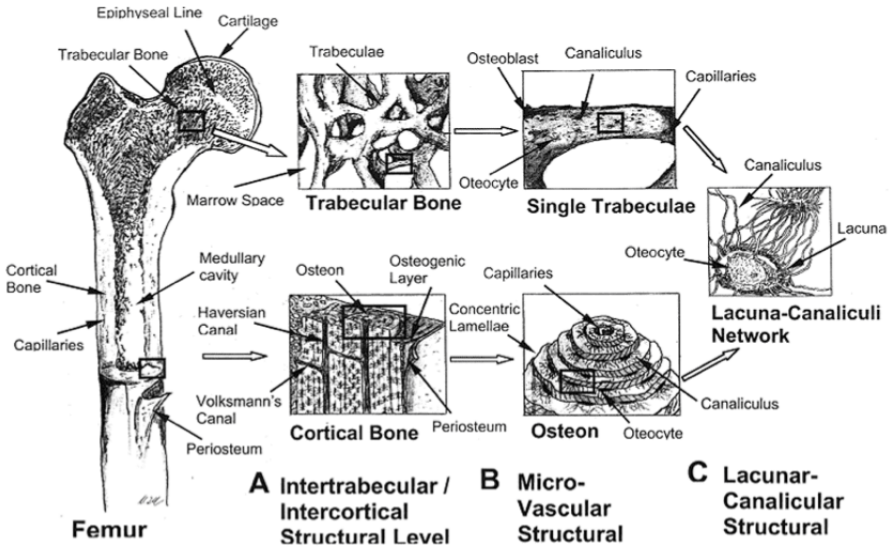

Figure 1.4: Bone Hierarchy. This cartoon depicts several of the levels of the hierarchy that makes up bone. A: The top level is the whole bone structure which is shown with the femur. B: The next lower level is the structural or architectural level which is shown by the osteons in cortical bone and the rods and plates for trabecular bone. C: The drawing depicts the next level, the tissue level, and shows one separate osteon and a single trabeculae. Within both of these structures lay the lacunae with the encapsulated osteocytes [Liebschner and Wettergreen, 2003].

Woven *vs.* Lamellar bone

Bone tissue can be classified based on collagen fiber arrangements into two different types: woven bone and lamellar bone. To repeat from above, bone is also classified into cortical and cancellous bone.

Woven bone consists of randomly oriented collagen fibers, with large numbers of osteoblasts and osteoprogenitors cells alongside (Figure 1.5). Under polarized light, it has a haphazard structure which is in great contrast to lamellar bone (see below). Woven bone is the only type of tissue that can be formed de novo, it does not need to form on existing bone or cartilage tissue. The disorganization of woven bone results from the speed at which it forms, which precludes the orderly deposition of collagen fibrils. The net result is bone tissue that possesses enhanced flexibility at the cost of stiffness. Woven bone contains relatively more cells per unit area than mature bone. Although woven bone is the major bone type in the developing fetus and it is often found in young growing skeletons, and lamellar (mature) bone is the

major bone type in the adult, areas of immature bone are also present in adults, especially where bone is being remodeled, around bone fracture sites in cases of trauma and disease. Early formation of woven bone enhances early restoration of skeletal mechanical integrity before its replacement by lamellar bone.

Lamellar bone is the mature form of adult bone. It is readily identified on polarized light microscopy as parallel lines of deposited bone (Figure 1.5). Lamellar bone is a more slowly forming tissue that characteristically contains collagen fibrils and mineral crystals arranged in sheets (lamellae). In general, it is formed only on pre-existing bone, either woven or lamellar. The control mechanisms involved in the formation of lamellar bone are still under investigation [Cowin, 1989, Khurana, 2009].

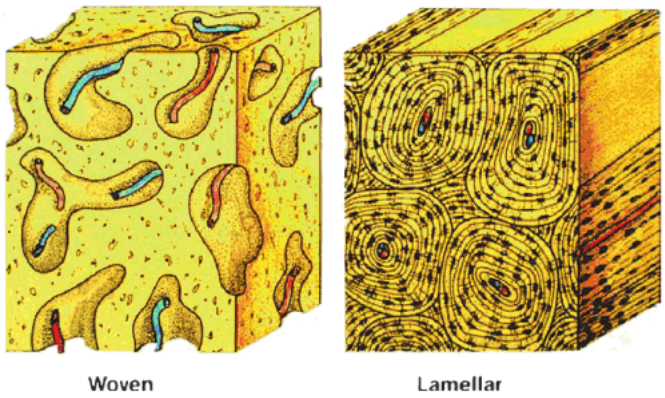

Figure 1.5: Diagram of immature and mature bone. Immature (woven) bone displays a disorganized lamellar appearance because of the interlacing arrangement of collagen fibers. The cells (osteoblasts and osteocytes) tend to be randomly arranged, whereas the cells in the mature bone are organized in circular fashion that reflects teh lamellar structure of the Haversian system. Resorption canals in mature bone have their long axes in the same direction as the Haversian canals [Khurana, 2009].

1.2.2 Hierarchical structure of bone

The complexity of bone's properties arises from the complexity in its structure. In order to fully understand the mechanical properties of bone material, it is important to understand not only the mechanical properties of its component phases, but also the structural relationship between them at the

various levels of hierarchical structural organization. These levels and the corresponding structures are:

- the macrostructure (> 0.5 mm): cancellous and cortical bone;
- the microstructure (from 10 to 500 μm): Haversian systems, osteons, single trabeculae;
- the sub-microstructure (1–10 μm): lamellae;
- the nanostructure (from a few hundred nm to 1 μm): collagen fibrils and fibers, and embedded mineral;
- the sub-nanostructure (below a few hundred nm): molecular structure of constituent elements, such as mineral, collagen, and non-collagenous organic proteins.

The resulting structure has an irregular, but optimized, arrangement and orientation of the components, making the bone heterogeneous and anisotropic (Figure 1.6) [Rho et al., 1998].

These hierarchical levels are discussed in detail in the following subsection.

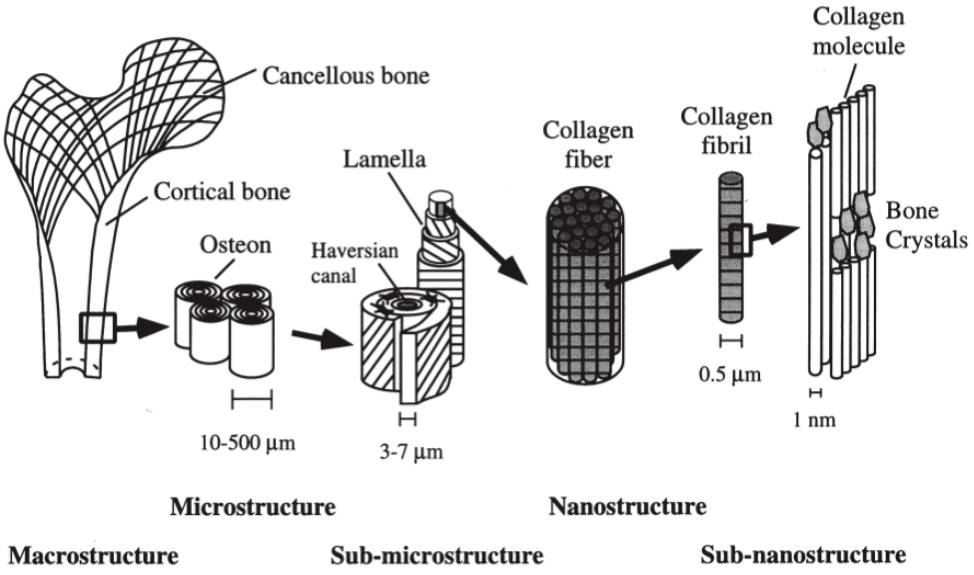

Figure 1.6: Hierarchical structural organization of bone: (a) cortical and cancellous bone; (b) osteons with Haversian systems; (c) lamellae; (d) collagen fiber assemblies of collagen fibrils; (e) bone mineral crystals, collagen molecules, and non-collagenous proteins [Rho et al., 1998].

Macrostructure

At the macrostructural level, the matured bone can be distinguished into two types, varying in density, and namely cancellous bone and cortical bone. They are organized with multi–level pores, macro to nano, for the achievement of multiple functions, including transportation of nutrients, oxygen, and body fluids. The adult human skeleton mass is composed of 80% cortical bone and 20% trabecular bone overall, but different bones and skeletal sites within bones have different ratios of them. The cortical bone functions mechanically in tension, compression, and torsion, whereas cancellous bone functions mainly in compression [Murugan and Ramakrishna, 2005, Rho et al., 1998]. See above Section 1.2.1.

Microstructure

At the microstructural level, mineralized collagen fibers are either randomly arranged (woven bone) or organized into planar arrangements called lamellae (3–7 μm wide).

In cortical bone 3–8 lamellae wrap in concentric layers around a central canal to form an osteon or Haversian system. In contrast, cancellous bone contains no such osteon units, but it is made of an interconnecting framework of trabeculae, each of which is approximately 200 μm thick.

Haversian systems are cylindrical in shape, and vary in size with an average diameter of 200 μm. The lamellae are often arranged in alternating layers of differing collagen orientation (0°–90°), which appear as "bright" or "dark" layers using circular polarized light microscopy (PLM), as shown in Figure 1.7. Gebhardt [Gebhardt, 1906] has been one of the first researchers to propose a detailed model able to explain the experimental evidences. He reported that parallel fibrils alternate between 0° and 90° in osteons. He called those with the collagen fibrils orientation predominantly transverse to the axis of osteons, which appear bright under PLM, as the thick lamellae, and those with the fibrils orientation in the longitudinal direction (along the axis of osteons), seen as dark under PLM, as the thin lamellae. Through electron microscopic analysis, Giraud-Guille [Giraud-Guille, 1988] observed that in addition to the orthogonal model of Gebhardt there is also a "twisted plywood" arrangement in which parallel layers of collagen fibrils rotate continuously through 180° cycles. Weiner et al. [Weiner et al., 1997] refined this to a "rotated plywood" configuration, where the fibrils not only rotate with respect to the osteon axis, but also around their own axis across the width of the lamella. There is, however, no consensus on the arrangement and orientation of the substance of a lamella.

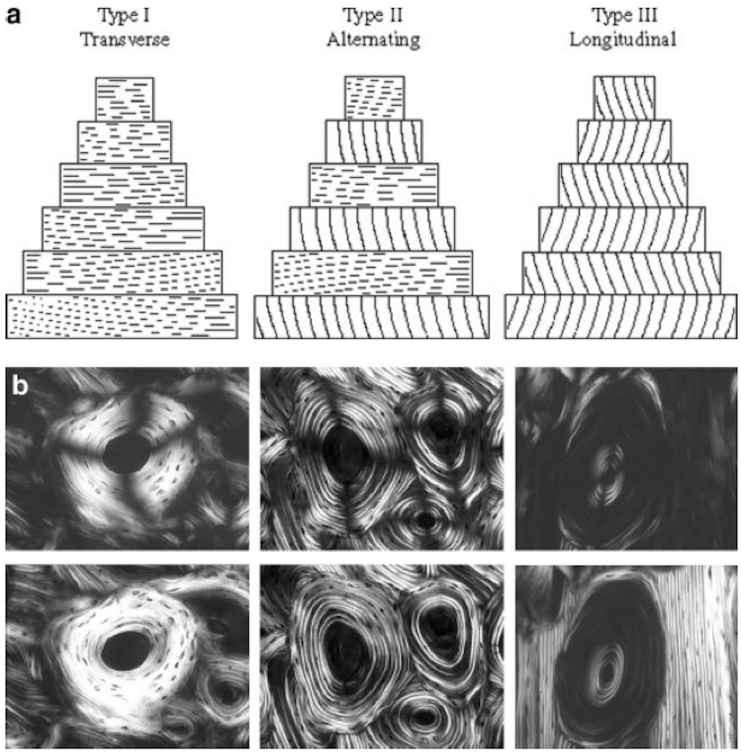

Figure 1.7: a. Secondary osteons may be generated along a continuum of lamellar organization representing extremes of collagen fiber orientation (horizontal and vertical hatching). Concentric lamellae are represented from the innermost (top) to the outermost (bottom) lamella. b. Top row: linearly polarized light (LPL) images. Bottom row: circularly polarized light (CPL) images. Left: Transverse osteons contain lamellae composed of collagen fibers transverse to the osteon axis and are bright in CPL. Middle: Alternating osteons contain lamellae composed of collagen fibers that alternate between transverse and longitudinal to the osteon axis, and which are bright and dark in CPL, respectively. Right: Longitudinal osteons contain lamellae composed of collagen fibers parallel with the osteon axis and are dark in CPL. Images of transverse and alternating osteons derive from modern human femoral midshaft, and images of the longitudinal osteon derive from the femoral midshaft of a brown-headed spider monkey. Field width of each frame = 475 μm [Bromage et al., 2003].

Two kinds of osteons can be recognized: primary and secondary. Primary osteons are structures formed around blood vessels in the initial growing phase of bone. Secondary osteons form after remodeling. During this process, bone cells first excavate a tubular path through the hard tissue, and then deposit the osteon layer by layer [Wang et al., 2010].

In contrast, cancellous bone contains no such osteon units, but it is made of an interconnecting framework of trabeculae, each of which is approximately 200 μm thick and 1 mm long. Lamellar layers located within trabeculae do not always run parallel with the trabecular surface, but exhibits a more random orientation than lamellae in Haversian system [Currey, 2002]. However, as is generally evident, the lamellar layers closest to the trabecular surface tend to follow the surface approximately. The trabeculae have three types of cellular structures: rod–rod, rod–plate, or plate–plate. A trabecular rod is about 50–300 μm in diameter. Unlike osteons, trabeculae in general do not have a central canal with a blood vessel. The porosity of trabecular bone may vary between 50% and 90%, with an average value of 75% [Rho et al., 1998].

Sub–microstructure

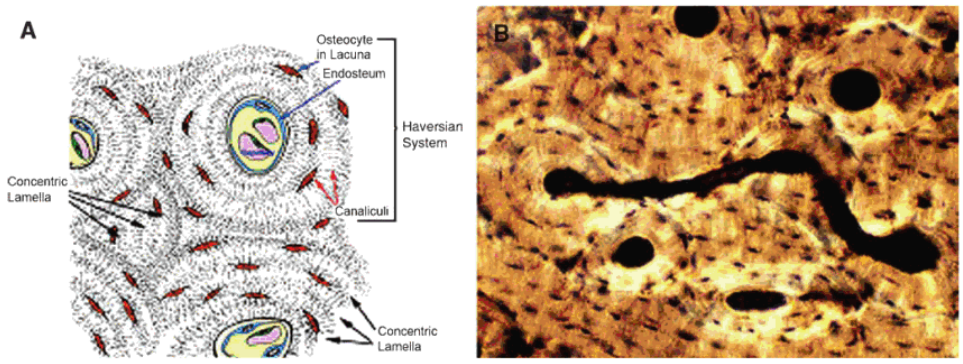

Figure 1.8: Cartoon and a microscopic photograph depicting the lamellar organization of bone. A. Cartoon representing a Haversian system with interstitial lamellae, osteocytes and canaliculi. B. Histological representation of Volkmann canal connecting Haversian canals of adjacent osteons [Khurana, 2009].

At the next hierarchical level, collagen fibrils, reinforced with crystals, are arranged in a roughly parallel manner and form lamellae with an average thickness range of approximately 3 to 7 μm [Rho et al., 1998]. Within each lamella, collagen fibrils are predominantly oriented in the same direction

[Ascenzi et al., 1978], allowing a high density of collagen per unit volume. The collagen fibrils form bundles 1–2 μm in diameter lying in the plane of the lamella.

Each lamella contains ellipsoidal cavities, called lacunae, that are typically 0.1 μm in diameter and 1–3 μm in long axis; they lie with their long axis parallel to the lamella long axis (Figure 1.8). Lacunae are cavities where osteocytes (bone cells buried in the matrix) are located. It is well accepted that osteocytes are the "mechano–sensory cells", responsible for the coordination of related cell activities. Each osteocyte has several (perhaps as many as 80) cytoplasmic processes. These processes are approximately 15 μm long and are arrayed three dimensionally in a manner that permits them to interconnect with similar processes of up to 12 neighbouring cells. These processes lie within small channels (order 0.1 μm radius), known as canaliculi, which provide passageways through the hard matrix and radiate from the lacunae to the Haversian canal. This network is commonly referred to as the lacunae–canaliculi network (LCN), and providing the ability of bone cells to respond to changes of the mechanical loading regime. It is agreed that mechanical signals are transmitted to the osteocyte cytoskeleton, either directly through deformation of the solid bone matrix, and/or indirectly via fluid motion in the LCN. The potential direct mechanisms include sensing of the strain magnitude, strain gradients, strain rates, strain energy density, and loading frequency as well as cycle number. The potential indirect mechanisms, in turn, include sensing of fluid pressure, shear stresses, and streaming potentials [Scheiner et al., 2010, Cowin and Doty, 2007]. The total volume of lacunae and canaliculi is relatively small, contributing to 10% of the total porosity [Wang et al., 2010].

Nanostructure

Similar for both cortical and cancellous bone, organic matrix, apatite mineral and water together make up the nanostructure of bone, which can be characterized as a composite of mineral crystals and collagen fibrils. While bone mineral is stiff and brittle, the protein is much softer and tougher. Both the individual characteristics of mineral crystals and collagen as well as the interaction between them are crucial for the mechanical performance of bone [Fratzl, 2004].

At this structural level, groups of collagen molecules aggregate to form mineralized collagen fibrils ($\approx$ 100 nm in diameter [Landis et al., 1996]), which group together with other fibrils to eventually form mineralized collagen fibers (Figure 1.9) [Rho et al., 1998].

Fibril formation is inherent in the nature of tropocollagen. Tropocollagen

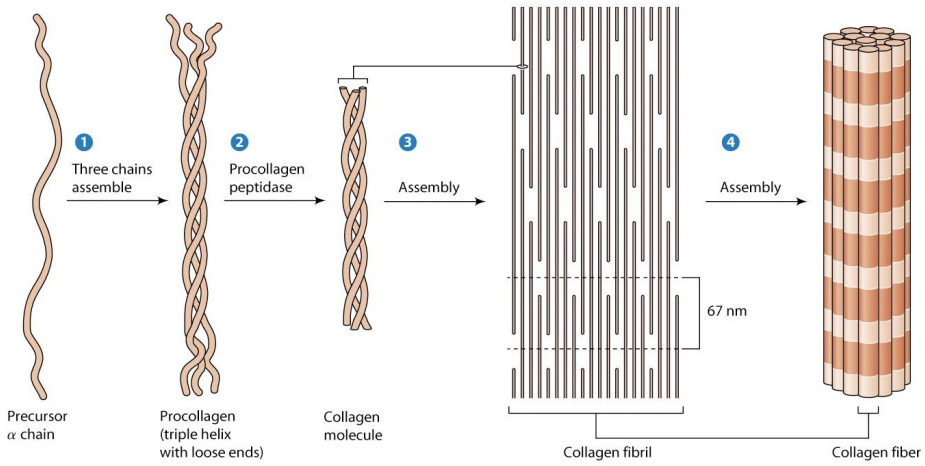

Figure 1.9: Collagen assembly. 1. Collagen precursor chains are assembled to form triple–helical procollagen molecules. 2. After secretion from the cell, procollagen is converted to collagen in a peptide–cleaving reaction catalyzed by the enzyme procollagen peptidase. 3. The molecules of collagen, also called tropocollagen, then bind to each other and self-assemble into collagen fibrils. 4. The fibrils assemble laterally into collagen fibers. In striated collagen, the 67–nm repeat distance is created by packing togheter rows of collagen molecules in which each row is displaced by one–fourth the length of a single molecule [Hardin et al., 2011].

is a highly reactive molecule, which easily undergoes spontaneous fibrillogenesis to create a supramolecular structure [Ottani et al., 2002]. The formation of these fibrillar structures is inherently linked with collagen cross-linking [Rho et al., 1998]. The longitudinal distribution of polar and hydrophobic residues along the length of the tropocollagen helix results in a staggered, lateral intermolecular interaction through the process of cross–linking during fibrillogenesis. This method of self–assembly results in the frequently observed molecular axial stagger within collagen fibrils, approximately 67 nm in magnitude. The axial stagger results in the 40 nm wide gap regions between the tropocollagen ends that are vital for the healthy mineralization process (Figure 1.9) [Ottani et al., 2002]. Initial fibril formation is stabilised by polar, hydrophobic, non-covalent interactions. These are commonly referred to as an immature cross-link and these chemical interactions bond specific amino acid residues within adjacent collagen molecules. One side of this bond is created within the tropocollagen telopeptide and the other lies within the helical region of the molecule. These immature non–covalent bonds are eventually superseded by stronger, mature covalent cross–links. These form by spontaneous reaction with the existing intermolecular immature cross–links to form this more stable mature form of cross–link [Bailey et al., 2002].

As alluded earlier within this Section, the gap regions formed between the telopeptide ends of the collagen molecules are of significant importance with regard to the process of mineralization. These gap regions become centres for ossification [Landis et al., 1996]. The specific nature of these residue sequences is believed to encourage the spontaneous precipitation of mineral out of the extracellular matrix onto an existing mineral nucleus. The mineralization process is predominantly intrafibrillar [Ottani et al., 2002, Weiner and Traub, 1989] and begins with the appearance of multiple simultaneous independent nucleation sites based at the ossification centres. The mineral crystal platelets formed at these sites eventually grow to form the observed mineral plates and extend along the fibril surface, forming a kind of reinforcing ring of apatite around the fibrils [Ottani et al., 2002]. The thickness of the platelets ranges from 2 to 7 nm, the length from 15 to 200 nm and the width from 10 to 80 nm [Fratzl, 2004, Rho et al., 1998]. The mineral crystals that form on and within these fibrils tend to grow exhibiting a specific crystalline orientation. The c-axes of the mineral crystals tend to run approximately parallel with the long axis of the associated fibrils [Weiner and Traub, 1989, Rho et al., 1998].

Mineralization enhances the stiffness of the fibrils by two mechanisms: firstly, the intrafibrillar mineral platelets strengthen the collagen fibrils in tension/compression along the fibril axis and in shear in the platelets' plane,

while the increase in its bending rigidity is less pronounced, thus preserving the fibril's flexibity. The extrafibrillar mineralization further strengthens the fibrils in all remaining deformation modes except those already stiffened by the intrafibrillar minerals [Nikolov and Raabe, 2008].

Sub–nanostructure

At the smallest unit of structure there are collagen, non–collagenous organic proteins, and mineral crystals.

The organic matrix consists of more than 90% of type I collagen and non–collagenous proteins [Wang et al., 2010]. The repetitive amino acid sequence of type I collagen allows three individual left–handed helical polypeptide (α) chains to fold into a right–handed triple helix of tropocollagen (or collagen molecule). The system of opposing helical twists gives the resulting tropocollagen molecule a significant advantage. The opposing twists reduce subsequent twisting of the collagen molecule when subjected to externally applied tensile forces. Twisting of the helical molecule, caused by externally applied tensile force, creates a residual stress within the structure, reducing the effective amount of load the molecule can carry prior to failure. The overall result is the reduction of tropocollagen's breaking or yield strength due to the presence of this residual stress [Gillham et al., 1997].

The 300 nm long and 1.5 nm thick collagen molecules are deposited by the osteoblasts into the extracellular space. Adjacent molecules are staggered along the axial direction by a distance of 67 nm, generating a characteristic pattern of gap zones with 35 nm length and overlap zones with 32 nm length within the fibril (Figure 1.10) [Fratzl, 2004]. The molecular packing is quasihexagonal, and the intermolecular spaces are filled with water and contain a small amount of noncollagenous proteins such as proteoglycans [Nikolov and Raabe, 2008]. The structural functions of non-collagenous proteins, such as osteocalcin, osteonectin, osteopontin, etc., are not very clear at present. These proteins may influence the events associating with bone remodelling, such as recruiment, attachment, differentation, and activity of bone cells [Wang et al., 2010]. Human bone mineral is primarily composed of calcium phosphate and is intimately associated with bone's organic matrix. Bone mineral (called dahllite) is composed of extremely impure form of hydroxyapatite, $Ca_{10}(PO_4)_6(OH)_2$ which forms nanometer-sized crystals. A substantial amount of carbonate (CO_3^{2-}) is commonly substituted into the apatite lattice for OH^- or PO_4. Additionally, apatite bone mineral contains a common Ca^{2+} ion vacancy, which often contains sodium, potassium, magnesium, and zinc substitutions [Weiner and Traub, 1986, Weiner and Price, 1986].

The porosity associated with the spaces between the collagen and the crystallites of the mineral apatite (order = 10 nm radius) is called the collagen-apatite porosity. The movement of the bone fluid in the collagen-apatite porosity is negligible because most of the bone water in that porosity is bound by interaction with the ionic crystal. This portion of the bone water is considered to be part of the collagen-apatite structure [Cowin, 1999].

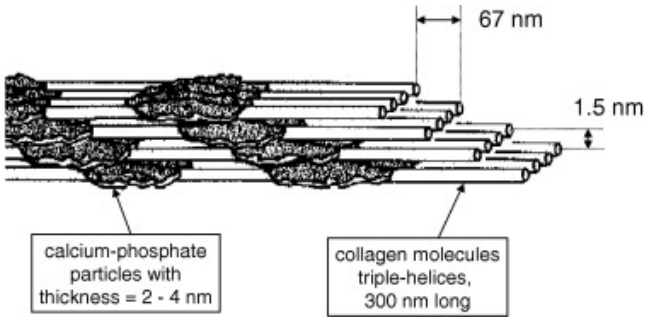

Figure 1.10: The mineral crystals are arranged parallel to each other and parallel to the collagen fibrils in the bone composite, in a regularly repeating, staggered arrangement. The staggering of the crystals is most likely due to the nucleation of mineral particles inside the gap zone of collagen fibrils [Fratzl and Gupta, 2007].

1.2.3 Composition of bone

The composition of bone depends on a large number of factors: the species, which bone, the location from which the sample is taken, and the age, sex, and type of bone tissue, *e.g.*, woven, cancellous, cortical [Bronzino, 2000]. However, a rough estimate for overall composition by volume is 50% mineral, 20% water, and 30% organic [Mow and Huiskes, 2004].

Bone contains two types of water: unbound and bound. Unbound water, which exists mostly in the interstitial fluid within larger (~ 0.1 μm to millimeter-sized) pore spaces, contributes significantly to the time-dependent mechanical properties of bone. It is well known that interstitial water molecules play a major role in stabilizing both collagen and mineral. The collagen and ground substance of the organic matrix contain many charged sites that facilitate interactions with unbound water. Bound water may stabilize the mineral crystallites by occupying OH^- and Ca^{2+} vacancy sites [Oyen, 2011, Garner et al., 2000]. The water content of bone tissue decreases with age and is associated with a reduction in biomechanical properties that are critical to the function of bone [Zioupos and Currey, 1998]. Early studies demon-

strated that the stiffness, tensile strength, and hardness increases, whereas the strain at fracture and energy to fracture decreases, following the dehydration of bone tissues [Dempster and Liddicoat, 1952, Evans, 1973, Evans and Lebow, 1951, Sedlin and Hirsch, 1966, Smith and Walmsley, 1959, Yamada and Evans, 1970, Nyman et al., 2006]. In addition, as trabecular bone loses water, its buckling behavior changes from ductile to brittle [Townsend et al., 1975]. Lastly, dehydration affects the viscoelasticity of bone: compared with wet bone, dry bone has less anelastic deformation (*i.e.*, less recoverable strain from creep) [Currey, 1965] and lower loss factor $\tan(\delta)$ (*i.e.*, a dimensionless measure of the viscoelastic damping) [Yamashita et al., 2001, Yamashita et al., 2002]. Despite the documented effects of drying on bone properties, the underlying mechanisms including structural changes in the matrix protein and mineral, and changes in their interactions brought about by dehydration are unclear.

1.2.4 Differences between species

Differences in the composition and structure between species are the most important factors that need to be discussed when choosing an animal model. The most often used animal models in bone studies include the rat, mouse, dog, cow, pig, sheep, rabbit etc. An ideal model that can be perfectly mimic human body does not exist. However, the animal is selected according to a series of criteria such as: availability, biological homogeneity of individual specimen, ease of handling and experimentation on, purchase price, cost for maintenance and cultural sensitivity, which may exclude the use of a given species in some countries.

Bone structural differences between human and cow are more important at microscale levels, and are more obvious in cortical bone than in trabecular bone. The cortical bone of human femur consists of secondary osteons and interstitial tissue, whereas the basic structure of bone from the cow is primary vascular plexiform bone. Thus bovine bone is more homogeneous than human bone. Plexiform bone must offer increased mechanical support for long periods of time, because of this, it is primarily found in large rapidly growing animals like cows and is an indicator of non-human bone [Martin et al., 1998, Manilay et al., 2012]. Katz and Yoon [Katz and Yoon, 1984] showed that plexiform areas are significantly stiffer than osteonal regions. Irregular Haversian bone tissue is sparsely found at the periosteal border and the posterior aspect of the femur from cows. On the other hand, the trabecular bone of these species is similar. Compositional differences of bone exist among different species. The ash content of cortical bone samples from all of the species is very similar, whereas the amount of the organic phase is

significantly different between the species [Wang et al., 2010]. Some data in the literature for the composition of adult human and bovine cortical bone are given in Table 1.1.

Species	% H_2O	% apatite crystal	% dry weight collagen	% GAG
Bovine	9,1	76,4	21,5	not available
Human	7,3	67,2	21,2	0,34

Table 1.1: Composition of human adult and bovine cortical bone. GAG means glycosaminoglycans [Herring, 1977].

1.3 Viscoelasticity of bone

Compact bone has proven to be a highly complex material. It is inhomogeneous, anisotropic, viscoelastic and exhibits detailed structure on all levels of scale [Lakes and Katz, 1979b]. Viscoelasticity in bone has been shown to correlate with hydration state and mineral content [Oyen, 2011] More structural materials are nearly linearly elastic under small strain as they retain linearity between load and deflection. Viscoelastic materials retain linearity between load and deflection, but the linear relationship depends on a third parameter, time. For this class of materials, the present state of deformation cannot be determined completely unless the entire loading history is known. The load-deflection relationship of a viscoelastic material is given by means of a convolution integral. Convolution of two functions is mathematically defined as:

$$C(t) = f(t) * g(t) = \int_0^t f(\epsilon) g(t - \epsilon)\, d\epsilon \tag{1.1}$$

Some characteristic phenomena in viscoelastic materials are (i) if the stress is held constant, the strain increases with time (creep); (ii) if the strain is held constant, the stress decreases with time (relaxation); (iii) the effective stiffness depends on the rate of application of the load; (iv) if the cyclic loading is applied, hysteresis (a phase lag) occurs, leading to a dissipation of mechanical energy.

Rauber [Rauber, 1876] was the first to demonstrate viscoelasticity in bone by studying creep as well as anisotropy and strength of bone. Lakes and Katz [Lakes and Katz, 1979b] applied the Boltzman superpositional integral

$$\sigma_{ij}(t) = \int_{-\infty}^{t} C_{ijkl}(t - \tau) \frac{d\epsilon_{kl}(\tau)}{d\tau}\, d\tau \tag{1.2}$$

as a constitutive equation for describing viscoelastic behaviour of bone in compression and concluded that it does not apply to bone for the entire frequency range. They extended this work in a series of papers of torsional and biaxial loading conditions [Lakes et al., 1979, Lakes and Katz, 1979b] concluding that non-linear viscoelastic constitutive equations are the best description of nonlinear effects observed experimentally.

The complex hierarchical structure of bone can cause viscoelastic behaviour rising from various processes occurring at various length scales. Sasaki et al. [Sasaki et al., 2002] argued that collagen, being proteinaceous, could give rise to significant viscoelastic behaviour. Earlier studies of Lakes and Saha (1979) have demonstrated that at a grosser scale, many interfaces such as cement lines and boundaries between lamellae could be responsible for viscoelastic behaviour. Throughout a microscopic examination of bone fracture surfaces, they observed that slowly moving cracks, in particular, tend to propagate along the cement lines. This observation had let some authors to postulate that the "cement-line" material, primarily composed of protein-polysaccharides, behaves as a zone of weakness. If this material exhibits a large compliance or is in fact viscous at small macroscopic stresses, then motion along these interfaces can result in large mechanical relaxations.

With regard to the mineral phase of bone, thermoelastic coupling, which is a result of damping from stress-induced heat flow from the material to its environment or the heat flow in between different heterogeneities in the material, could also be a casual mechanism of viscoelastic behaviour. This piezoelectric coupling however was shown to have a negligible contribution [Lakes and Katz, 1979b].

Finally, and very importantly, viscoelasticity in bone could be the result of fluid flow in a porous medium [Cowin, 1999]. There are three levels of bone porosity within cortical bone and within the trabeculae of cancellous bone, all containing a fluid. Thus a significant dissipation of mechanical energy can result from the motion of fluids in connected pores.

When a viscoelastic solid is subjected to mechanical strain, part of the strain-energy is converted to other forms and ultimately degraded into heat. What happens to this energy in living bones can be of considerable biological importance. For example, bone is known to remodel itself in response to mechanical stress in such a way as to more effectively support the stress (Wolff's law). A variety of mechanisms have been proposed to account for this activity and, in each of them, mechanical energy is transformed into other forms before being dissipated. An investigation of these and other viscoelastic mechanisms can elucidate the role of strain energy dissipation in living tissues.

1.4 Viscoelastic phenomena

Most solid materials are described, for small strains, by Hooke's law of linear elasticity: stress σ is proportional to strain ϵ. In one dimension, Hooke's law is as follows:

$$\sigma = E\epsilon \tag{1.3}$$

with E as Young's modulus. Hooke's law for elastic materials can also be written in terms of compliance J:

$$\epsilon = J\sigma \tag{1.4}$$

Consequently, the elastic compliance J is the inverse of the modulus E:

$$J = \frac{1}{E}. \tag{1.5}$$

In contrast to elastic materials, a viscous fluid under shear stress obeys

$$\sigma = \eta \frac{d\epsilon}{dt}, \tag{1.6}$$

with η as the viscosity. Viscoelastic materials are those for which the relationship between stress and strain depends on time.

1.4.1 Creep

Creep is a progressive deformation of a material under constant stress. In one dimension, suppose the history of stress σ as it depends on the time t to be step function with the magnitude σ_0, beginning at time zero:

$$\sigma(t) = \sigma_0 H(t). \tag{1.7}$$

$H(t)$ is the unit Heaviside step function. The strain $\epsilon(t)$ in a viscoelastic material will increase with time. The ratio,

$$J(t) = \frac{\epsilon(t)}{\sigma_0} \tag{1.8}$$

is called the creep compliance. In linearly viscoelastic materials, the creep compliance is independent of stress level. If the load is released at a later time, the strain will exhibit recovery or a progressive decrease of deformation. Strain in recovery may or may not approach zero, depending on the material.

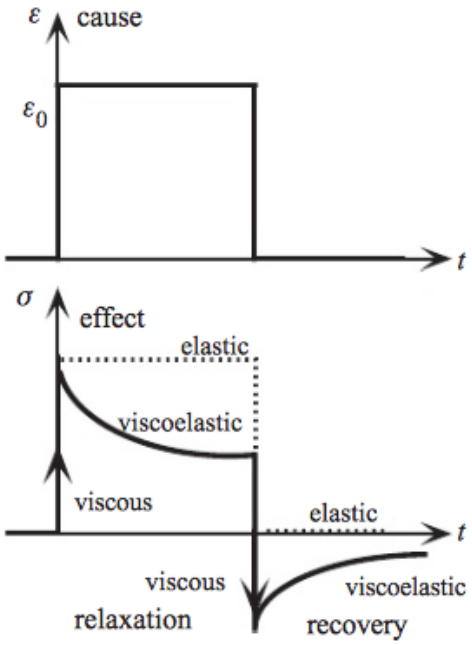

Figure 1.11: Creep and recovery. Stress σ and strain ϵ versus time t [Lakes, 2009].

1.4.2 Relaxation

Stress relaxation is the gradual decrease of stress when the material is held at constant strain. If we suppose the strain history to be a step function of magnitude ϵ_0 beginning at time zero:

$$\epsilon(t) = \epsilon_0 H(t), \tag{1.9}$$

the stress $\sigma(t)$ in a viscoelastic material will decrease as shown in Figure 1.12. The ratio,

$$E(t) = \frac{\sigma(t)}{\epsilon_0} \tag{1.10}$$

is called the relaxation modulus. In linear materials, it is independent of strain level, so $E(t)$ is a function of time alone.

Creep and deformation can occur in shear or in volumetric deformation as well. The relaxation function for shear stress is called $G(t)$. For volumetric deformation, the elastic bulk modulus is called B (also called K). A corresponding relaxation function $B(t)$ may be defined as above, but with the stress as a hydrostatic stress. A similar distinction is made in the creep

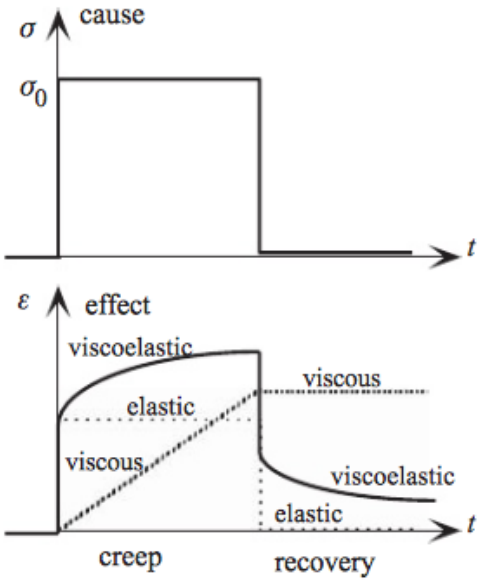

Figure 1.12: Relaxation and recovery. Stress σ and strain ϵ versus time t [Lakes, 2009].

compliances, $J_G(t)$ for creep in shear, $J_E(t)$ for creep in extension, and $J_B(t)$ for creep in volumetric deformation.

1.4.3 Dynamic response to sinusoidal load: E^*, $\tan\delta$

Suppose the stress $\sigma(t)$ is varying (Figure 1.13) sinusoidally in time t, as follows:

$$\sigma(t) = \sigma_0 \sin(2\pi\nu t) \tag{1.11}$$

The frequency (in cycles per second or Hertz) is called ν. The strain response of a linearly viscoelastic material is also a sinusoidal in time, but the response will lag the stress by a phase angle δ

$$\epsilon(t) = \epsilon_0 \sin(2\pi\nu t - \delta). \tag{1.12}$$

The period T of the waveform is the time required for only on cicle: $T = 1/\nu$. The phase angle is related to the time lag Δt between the sinusoids by $\delta = 2\pi\Delta t/T$. The resulting phase lag is therefore between 0 and $\pi/2$. As a result of the phase lag between stress and strain, the dynamic stiffness can be treated as a complex number E^*:

$$\frac{\sigma}{\epsilon_0} = E^* = E' + iE''. \tag{1.13}$$

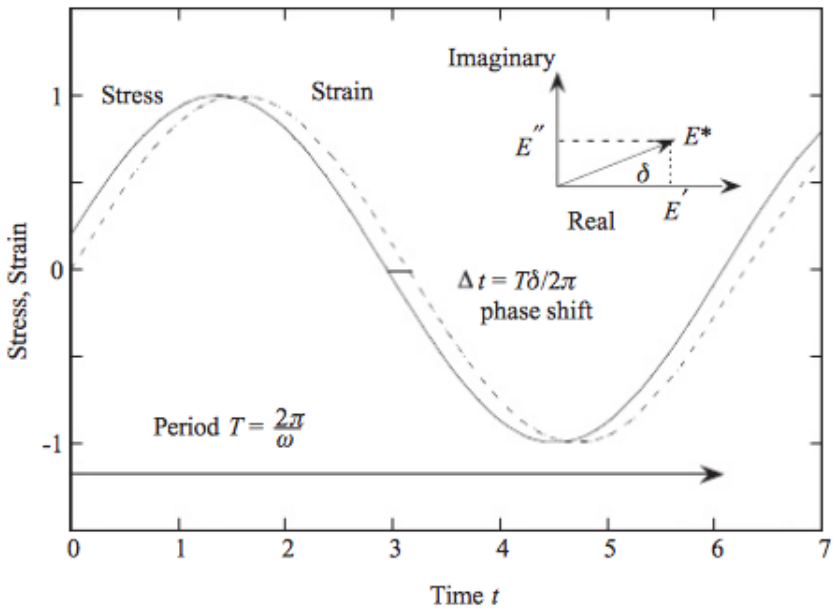

Figure 1.13: Stress σ and strain ϵ versus time t in dynamic loading of a viscoelastic material [Lakes, 2009].

The single and double primes designate the real and imaginary parts. The storage modulus E' characterizes elastic behavior while the loss modulus E'' characterizes viscous behavior. The loss angle δ is a dimensionless measure of the viscoelastic damping of the material. The dynamic functions E', E'' and δ depend on frequency. The tangent of the loss angle $\tan\delta$ is called loss tangent (dimensionless) and is:

$$\tan\delta(2\pi\nu) = \frac{E''(2\pi\nu)}{E'(2\pi\nu)}. \tag{1.14}$$

The physical meaning of the loss tangent is associated with the ratio of energy dissipated to the energy stored in dynamic loading. This is why it is considered a measure of "internal friction" or mechanical dissipation. Friction, a surface effect that always has a threshold and is always non-linear, is different from internal friction that represents energy dissipation per volume and usually refers to a linear or perhaps weakly non-linear effect. Ideal elastic materials show no $\tan\delta$, whereas viscous materials exhibit high values of $\tan\delta$ [Yamashita et al., 2001, Lakes, 2009].

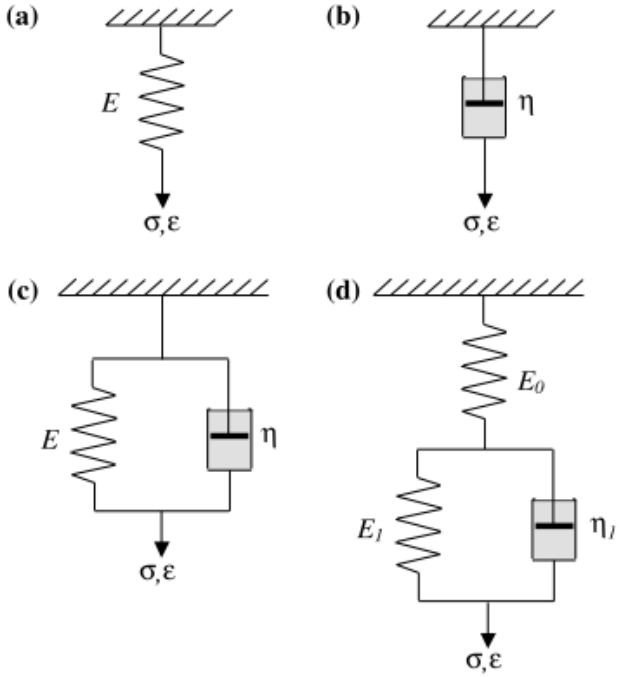

Figure 1.14: Elements used for viscoelastic models. (a) linear spring element; (b) dashpot element; (c) Kelvin-Voigt model; (d) simple Standard Linear Solid model [Kruijer et al., 2006].

1.4.4 Prediction of response to arbitrary stress history

A linear viscoelastic material obeys to the principle of time invariance and therefore superposition can be applied. If a stress $\Delta\sigma_1$ is applied at time t_1 and an additional stress $\Delta\sigma_2$ at time t_2, then the strain response is the sum of the individual responses,

$$\epsilon(t) = J(t - t_1)\Delta\sigma_1 + J(t - t_2)\Delta\sigma_2 \tag{1.15}$$

An arbitrary stress history can be considered as a sequence of infinitesimal steps. The summation sign then changes to an integral,

$$\epsilon(t) = \int_{-\infty}^{t} J(t - \tau)\frac{d\sigma}{d\tau}\, d\tau \tag{1.16}$$

If the role of strain and stress are interchanged a complementary relation may be obtained:

$$\sigma(t) = \int_{-\infty}^{t} E(t - \tau)\frac{d\epsilon}{d\tau}\, d\tau \tag{1.17}$$

The integrals are referred to as the hereditary integrals or the Bolzmann convolution integrals. An appropriate engineering method to describe $J(t)$ is by means of spring and dashpot models. Ideal springs and dashpot are combined to arrive at models of realistic viscoelastic materials, and see how they respond to stimuli that vary with time [Herman, 2008] The spring and dashpot, see Figure 1.14 a and b, obey the following equations, respectively:

$$\sigma = E\epsilon (1.3) \tag{1.18}$$

$$\sigma = \eta \frac{d\epsilon}{dt} (1.6) \tag{1.19}$$

These two elements can be placed in series to form the Maxwell model. Because deformation is assumed to be quasistatic, inertia is neglected and the stress is the same in both elements; the total deformation is the sum of the strains. If we input step stress, the creep response is:

$$J(t) = \frac{1}{E} + \frac{t}{\eta}. \tag{1.20}$$

This form is unrealistic for primary creep because the predicted creep response versus time is a straight line, in contrast to curves that are observed experimentally. The Kelvin-Voigt (KV) model consists of a spring and dashpot in parallel, as shown in Figure 1.14 c. The spring and the dashpot experience the same deformation and the total stress is the sum of the stresses in each element. The creep response of the Voigt model is:

$$J(t) = \frac{1}{E}(1 - e^{-\frac{t}{\tau_c}}), \tag{1.21}$$

in which $\tau_c = \eta/E$ is referred to as the retardation time. However the relaxation response is a constant plus a delta function. More realistic behavior involving a single exponential in both creep and relaxation can be modeled by the standard linear solid (SLS) model (see Figure 1.14 d), where the KV model is placed in series with a spring element. The spring with Young modulus E_0 describes the instantaneous elastic deformation, while the parallel combination of a spring with Young modulus E_1 and a dashpot with viscosity η_1, which describes the delayed elastic deformation. Since the elements are connected in series, the stresses in both the branches are the same, while the strains in the two parts are additive. By considering equilibrium of stresses and compatibility of strains, the governing equation of the SLS model is found to be the following first-order differential equation [McCrum et al., 1997]:

$$\eta E_0 \frac{d\epsilon}{dt} + E_0 E_1 \epsilon = \eta E_0 \frac{d\sigma}{dt} + (E_0 + E_1)\sigma \tag{1.22}$$

When eq. is solved by integration for the conditions of creep at a constant stress σ_0, the creep compliance $J(t)$ is found to be:

$$J(t) = \frac{\epsilon(t)}{\sigma_0} J(t) = \frac{1}{E_0} + \frac{1}{E_1}(1 - e^{-\frac{t}{\tau_1}}) \tag{1.23}$$

Where $\tau_1 = \eta_1/E_1$. The solution of the simple SLS eq., however, includes only a single retardation time (τ_1), whereas real viscoelastic materials tend to have a relatively broad retardation spectrum, spreading over several time decades [Kruijer et al., 2006]. This behavior can be modeled by combining a number of elements into a multi mode model. Four-parameter and higher order models may also be constructed. There are two standard patterns for systematically designing higher order models. N Kelvin-Voigt units in series lead to the generalized Kelvin model, while in the generalized Maxwell model N Maxwell units are assembled in parallel [Mase and Mase, 1999]. The creep compliance, $J(t)$, for the generalized Kelvin model is found to be:

$$J(t) = \frac{\epsilon(t)}{\sigma_0} J(t) = \frac{1}{E_0} + \sum_{i=1}^{N} \frac{1}{E_i}(1 - e^{-\frac{t}{\tau_i}}) \tag{1.24}$$

where τ_i is the retardation time of the i'th KV element. The viscoelastic expressions above are valid for a simple stress state in which a specimen is subjected to uniaxial tension. However, the information obtained from such a test must be cast into a form that is applicable to the multi-axial stress states. For multi-axial viscoelastic problems it is more convenient to use the shear modulus G and bulk modulus K, rather than E and Poisson's ratio ν which are normally used for linear elastic problems. G and K are defined as:

$$K = \frac{E}{3(1 - 2\nu)} \tag{1.25}$$

$$G = \frac{E}{2(1 + \nu)} \tag{1.26}$$

In three dimensions, Boltzman convolution integral becomes:

$$\sigma_{ij}(t) = \int_{-\infty}^{t} C_{ijkl}(t - \tau) \frac{d\epsilon_{kl}(\tau)}{d\tau} \, d\tau \tag{1.27}$$

This equation is sufficiently general to accommodate any degree of anisotropy. Each independent component of the modulus tensor can have a different time dependence. Many practical materials are approximately isotropic. For isotropic materials, the constitutive equation is:

$$\sigma_{ij} = \lambda \epsilon_{kk} \delta_{ij} + 2\mu \epsilon_{ij}, \tag{1.28}$$

in which λ and μ are the two independent Lamé elastic constants, $\delta_i j$ is the Kronecker delta (1 if $i = j$, 0 if $i \neq j$), and $\epsilon_k k = \epsilon_1 1 + \epsilon_2 2 + \epsilon_3 3$. Alternatively, the stress tensor σ_{ij} can be split into a deviatoric stress tensor $s_i j$ and a hydrostatic part $\sigma_k k$:

$$\sigma_{ij} = s_{ij} + \frac{1}{3}\sigma_{kk}\delta_{ij}. \tag{1.29}$$

Subsequently, also the linear strain tensor, ϵ_{ij} can be split into a deviatoric and a volumetric part:

$$\epsilon_{ij} = e_{ij} + \frac{1}{3}\epsilon_{kk}\delta_{ij}, \tag{1.30}$$

where e_{ij} and ϵ_{kk} denote the deviatoric and the volumetric strain part, respectively. The relation between the strain and the stress tensor is described by Hooke's law for isotropic linear elastic materials:

$$\epsilon_{ij} = \frac{1}{2G}s_{ij} + \frac{1}{9K}\sigma_{kk}\delta_{ij}. \tag{1.31}$$

Both G and K can be considered to be time dependent functions for an isotropic linear viscoelastic material. Engineering constants, such as Young's modulus E, Poisson's ratio ν, shear modulus G, bulk modulus K can be extracted from these tensorial constant. Specifically:

$$\begin{aligned} G = \mu\,, \qquad & K = \frac{2G(1+\nu)}{3(1-2\nu)}\,, \\ E = \frac{G(3\lambda+2G)}{\lambda+G}\,, \qquad & \nu = \frac{\lambda}{2(\lambda+G)}\,. \end{aligned} \tag{1.32}$$

As for interpretation of C_{1111} for isotropic elastic materials, we note that:

$$C_{1111} = E\frac{1-\nu}{(1+\nu)(1-2\nu)} \tag{1.33}$$

In isotropic viscoelastic solids,

$$\sigma_{ij}(t) = \int_{-\infty}^{t} \lambda(t-\tau)\delta_{ij}\frac{d\epsilon_{kk}}{d\tau}\,d\tau + \int_{-\infty}^{t} 2\mu(t-\tau)\frac{d\epsilon_{ij}}{d\tau}\,d\tau \tag{1.34}$$

There are two independent viscoelastic functions that can have different time dependence. As in the case of elasticity, we may consider engineering functions rather than tensorial ones, for example $E(t)$, $G(t) = \mu(t)$, $\nu(t)$ and $B(t)$ [Kruijer et al., 2006, Lakes, 2009].

1.5 Contact Mechanichs and Indentation Testing

Nanoindentation is an evolution of the basic mechanical engineering hardness test. This test involves probing a sample using a diamond tipped indenter and quantifying the resulting impression left on the material's surface. From this measurement, the sample hardness or resistance to plastic deformation can be assessed. Nanoindentation involves a similar idea but advances the technique through the use of recent improvements in measurement technology and indentation theory.

Nanoindentation involves an axisymmetric indenter of arbitrary profile being driven into a material's surface. The material directly beneath the indenter tip deforms both plastically and elastically. The tip is then unloaded, resulting in recovered elastic deformation as it is removed from the surface. A permanent residual impression is left on the sample,Äôs surface, but unlike conventional hardness testing, the impression is not assessed visually. Instead, load and corresponding displacement data are recorded as a function of time throughout the testing phase. From the measurements, mechanical characteristics of the material can be derived at the point of tip unloading. Hardness and indentation modulus are the most commonly derived mechanical characteristics, but fracture toughness can also be determined using nanoindentation.

1.5.1 History

Traditional hardness tests have been used for decades to measure the resistance of a material to deformation. In the late 18^{th} and early 19^{th} century several attempts were made to rank the deformation of materials by scratching one material with another. The technique has its origins in Mohs hardness scale of 1822 in which materials that are able to leave a permanent scratch in another were ranked harder material with diamond assigned the maximum value of 10 on the scale. While this was useful for comparative purpose (and is still referred to in the Mohs hardness scale), there remained the problem of quantifying hardness.

In the late 19^{th} century work by Hertz [Hertz, 1896] and Auerbach [Auerbach, 1893] brought about early examples of static indentation testing. In these cases, the samples were probed with a ball of a given material, and the deformation was measured by considering the contact area between the ball and sample.

It was not until the early $1900s$ that [Brinell, 1900] presented a standard

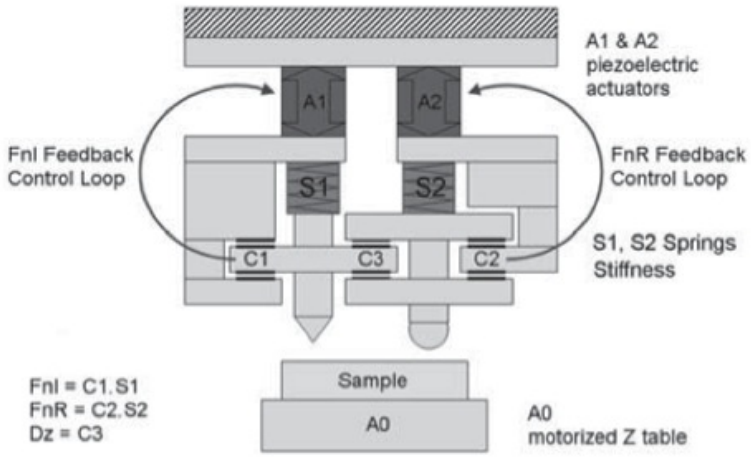

Figure 1.15: Two-axis Ultra Nanoindentation Tester (UNHT): A0 represents the displacement of the motorized Z table, A1 and A2 are the piezo actuators used for the application of the active reference force (FrR) and the indenter normal force (FnI). S1 and S2 represent the springs used in the system for measurement of the forces involved. The indentation depth (Dz) of the indenter tip is directly measured via the differential capacitive sensor C3.

method of evaluating hardness, based on applying a fixed load to a hard spherical indenter tip into a flat plate. After $15-30\,\mathrm{s}$, the load was removed and the diameter of the impression was measured using optical microscopy. Note that this method evaluates the load applied to the surface area of the residual impression. However, the Brinell test has shown to be affected by both the applied load and diameter of the ball used for indenter. The idea that hardness should be a materials property, and not dependent on the test method, led to the observations that the parameter which remains constant for large indentations appears to be the mean pressure, defined as the load divided by the projected contact area of the surface. Meyer suggested in 1908 that the hardness should therefore be defined as

$$H = 4\frac{P}{\pi d^2} \tag{1.35}$$

where H is the hardness, P the applied load and d the chordal diameter of the residual impression [Hoyt, 1924].

Both the Brinell and the Meyer hardness methods require each indentation to be observed with an optical microscope to measure the diameter of the indentation. This makes the testing slow and requires a skilled operator to carry out the test. The Rockwell hardness test focused on measuring the

depth an indenter penetrated into a sample under load. As the depth would correspond to an area of contact if the geometry of the indenter was known, it was thought that measuring the depth would provide an accurate and automatic measurement of hardness. For a detailed description of history of the development of hardness testing, the reader is referred to the work of [Lys, 1949].

The development of the Vickers indentation test, and determination of the angles used during pyramidal indentation [Smith and Sandland, 1925], followed the basic method of the Brinell test, but replaced the steel ball with a diamond pyramid ground. Other indenter geometries have been developed, in particularly the asymmetric pyramid (Knoop) and the three-sided pyramid (Berkovich). The driving force towards using the conical geometry over pyramids is that fabricating diamond tips with extremely small root radii is challenging and even the most finely fabricated diamond tips do not reach the pyramidal geometries at their apex, and commonly are approximated by an effective tip radius [Sharpe, 2008].

1.5.2 Theory

It is common practice to condense the indentation data into two quantities, the hardness H and the indentation modulus M, which are related to measured indentation data, namely the maximum indentation force P_{max}, the initial slope (or indentation stiffness) S of the unloading curve, and the projected contact area A_c by:

$$H = \frac{P_{max}}{A_c}, \tag{1.36}$$

$$S = \left.\frac{dP}{dh}\right|_{h=h_{max}} = \frac{2}{\sqrt{\pi}} M \sqrt{A_c}. \tag{1.37}$$

It is generally agreed today that combining accurate indentation data (F_{max}, S, A_c) and relations (2.6) and (1.37) is a convenient way to extract intrinsic mechanical properties of materials that can be described by time independent constitutive relations [Tabor, 1951, Doerner and Nix, 1986, Oliver and Pharr, 1992].

The time dependence of the constitutive relations complicates indentation analysis. The most readily observed effect of viscoelasticity on indentation is creep, or an increase of the indentation depth h under a constant load, which leads to an increase in the contact area A_c and a decrease in the hardness H (2.6) with time. Moreover, the time dependence of the constitutive behavior of the indented material may also affect the loading and unloading parts,

when the time scales of loading and unloading interfere with the characteristic time scales of the time dependent material behavior.

Based on the adaptation for indentation analysis of the method of functional equations [Lee and Radok, 1960], closed-form solutions for indentation in various linear viscoelastic solids became recently available for a variety of indenter shapes: flat punch indentation [Cheng et al., 1999], spherical indentation [Cheng et al., 2005, Oyen, 2006], and conical indentation [Vandamme and Ulm, 2006, Oyen, 2006]. The method of functional equations consists in solving the viscoelastic problem from the elastic solution by replacing the elastic moduli with their corresponding viscoelastic operators. For indentation problems, the method of functional equations remains valid as long as the contact area (or, equivalently for viscoelastic materials, the penetration depth) increases monotonically [Lee and Radok, 1960].

A full physical and mechanistic model for viscoelastic behavior remains elusive; for engineering practice, it is common to fit the elastic modulus-time responses to empirical functions based on simple mathematical constructs such as an exponential decay or a power-law decay time [Oyen, 2011].

1.6 Nanoindentation of Bone

Bone's mechanical properties vary widely at different length scales. Large hydrated cortical tensile specimens produce modulus values ranging from $14 - 20\,\mathrm{GPa}$ [Reilly et al., 1974, Bayraktar et al., 2004], micrometer-sized specimens yield values of $5.4\,\mathrm{GPa}$ [Choi et al., 1990], and tensile specimens from dissected osteons measure at $12\,\mathrm{GPa}$ [Ascenzi and Bonucci, 1967]. In order to understand bone's mechanical properties at multiple scales, the basic structural building blocks must also be investigated. Nanoindentation is the ideal tool as it allows testing of small volumes of bone and excludes the effects of large-scale porosity on mechanical property measurement. Additionally, nanoindentation can be used to determine the nanomechanical properties of bone's various microstructures (*e.g.*, individual lamellae), which are on the order of micrometers and are thus ideally suited for indentation testing. At any scale, the mechanical response of bone depends heavily on extrinsic factors that include preparation techniques, sample geometry (*e.g.*, testing a whole bone versus a machined section), hydration state, and mechanical test type and parameters (*e.g.*, strain rate) [Oyen, 2011]. The method of surface preparation can also affect mechanical properties because surface roughness can have a significant impact on the measurement of modulus using nanoindentation. To minimized errors arising from surface roughness, mineralized tissues are often microtomed or polished prior to indentation [Ebenstein and

Pruitt, 2006]. Additionally, a wide variety of testing parameters such as loading rate and indenter tip shape must be considered in order to extract a specific set of mechanical properties.

The Oliver-Pharr formulation used to commonly extract elastic modulus from an indentation unloading curve assumes that the test material is homogeneous, isotropic, and elastic-plastic. Instead, bone is heterogeneous, anisotropic, and viscoelastic. Caution must therefore be taken when testing and interpreting nanoindentation results to understand bone's unique structural and mechanical response [Oyen, 2011].

1.6.1 Viscoelastic Indentation

In the case of an elastic indentation problem, there is a closed-form analytical solution for the load-displacement behavior, in particular the relationship between load (P) and displacement (h) is not linear, with $P \sim h^2$ for conical-pyramidal indentation and $P \sim h^{3/2}$ for spherical indentation (see [Oyen, 2006] for details). Lee and Radok [Lee and Radok, 1960] proposed that a pseudo-linear viscoelastic analysis could be performed for the indentation problem by replacing the elastic constants within the nonlinear load-displacement relationship with viscoelastic operators.

1.6.2 Sample Hydration

Despite the fact that most biological materials are naturally hydrated, much of the early work in bone indentation was performed on dehydrated samples. The water content of bone, which typically ranges from 10% to 20%, plays an important role in determining its mechanical properties. Studies of bone specimens report increases in indentation moduli of 11% to 28% after dehydration [Rho et al., 1997, Rho et al., 1999, Zysset et al., 1999]. In bovine femur cortical bone, dehydration increased E in osteonal tissue and interstitial lamellae by 15.4% and 9.7%, respectively, a result that was attributed to the fact that drying contracts the individual fibrils in the tissue [Rho and Pharr, 1999]. Other studies illustrate the importance of selecting an appropriate hydrating fluid. Fox example Habelitz et al. [Habelitz et al., 2002] demonstrate that storage of dentin and enamel specimens in a salt solution maintains mechanical properties, while storage in deionized water results in a decrease in modulus and hardness that can be attributed to demineralization of the surface [Habelitz et al., 2002].

1.6.3 Tip Geometry

The selection of the optimal tip geometry is critical for obtaining high quality indentation data. The biggest limitation in tip selection lies in our limited understanding of what occurs within the collagen, mineral and pore spaces within the bone material, at nanometer length scales, during an indentation event. For example, plastic deformation under an indenter tip likely results in compaction of the mineral platelets, possible generation of microcraks within the material of bone, pore collapse, and permanent displacement of water (for bone in a hydrated state) [Tai et al., 2005]. The mechanics of how each tip contacts and indents into the bone material is therefore of critical importance and should be considered when determining the experimental approach to testing elastic, "plastic", or viscous behaviors.

The majority of bone indentation experiments have been carried out with a Berkovich tip, which is supplied with most commercially available testing system. The tip radius of a typical new Berkovich indenter is on the order of $50 - 100\,\text{nm}$, but usually increases to about $200\,\text{nm}$ with use [Fischer-Cripps, 2011]. The Berkovich tip, possessing a contact radii that is similar in size to a lamella, has been effectively used to determine mechanical properties of such individual structural features in bone [Zysset et al., 1999, Rho et al., 2002]. However, Berkovich tips are "sharp" and cause significant plastic deformation at the onset of indentation.

Spherical tips serve as a powerful tool to study both elastic and viscoelastic properties in bone tissue. For spherical indenters, the contact stresses are initially small and produce only elastic deformation avoiding damaging the sample [Ebenstein and Pruitt, 2006]. As the spherical indenter is driven into the surface, a detectable transition from elastic to plastic deformation occurs. In contrast, Berkovich tips have an immediate onset of plasticity at very small displacements due to the stress concentration near the material's surface [Oyen, 2011]. Anyway at the microscale, the use of spherical indenters has been impeded by difficulties in obtaining high-quality spheres made from hard, rigid materials. This is one reason the Berkovich indenter has been the indenter of choice for most small-scale testing, even though it cannot be used to investigate the elastic-plastic transition.

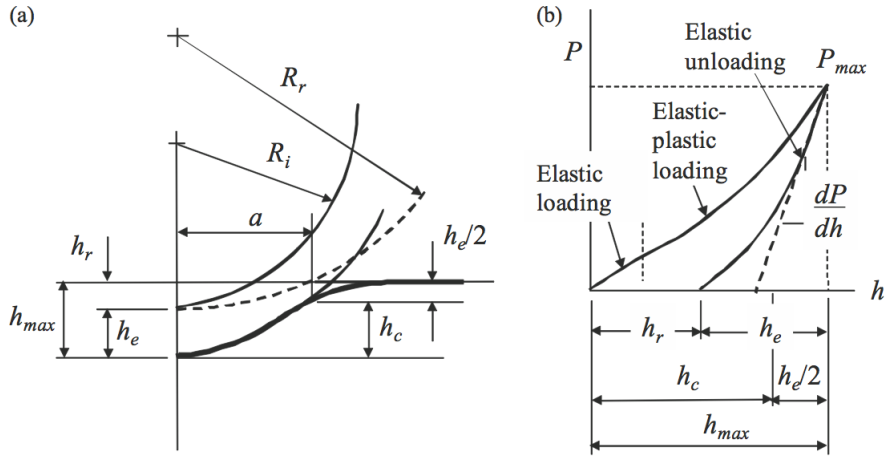

Figure 1.16: (a) Geometry of loading a preformed impression of radius R_r with a rigid indenter radius R_i. (b) Compliance curve (load vs displacement) for an elastic-plastic specimen loaded with a spherical indenter showing both loading and unloading response. Upon loading, there is an initial elastic response followed by elastic-plastic deformation. Upon complete unload, there is a residual impression of depth h_r [Fischer-Cripps, 2011].

CHAPTER 2

Materials and Methods

In the present work the material is considered as a linear viscoelastic solid and described by a three-element model, *i.e.*, a standard linear solid (SLS) model in viscoelasticity. This is a useful approximation to many polymeric materials [Meares, 1965, Ferry, 1980, Sperling, 1986]. The reason is that it exhibits a solid-like character with retarded elasticity, *i.e.*, both instantaneous and delayed elastic deformation [Cheng et al., 2005].

Mechanical characterization of the bone tissue samples was carried out using nanoindentation. The hardness and the indentation modulus are calculated from the unloading portion of load-displacement data using the Oliver-Pharr method [Oliver and Pharr, 1992]. The bone indentations with a Berkovich and spherical tips are then examined using analytical solution derived from Vandamme and Ulm [Vandamme and Ulm, 2006], and Cheng *et al.* [Cheng et al., 2005] respectively.

The dependent quantity of interest, the indentation depth h, depends on the time t, the load history parameters (P_{max}, τ_L, τ_H, τ_U), the elastic properties (E_0, ν_0), the viscous properties (E_1, ν_1, η_1) and the indenter geometry. The input parameters are the instantaneous elastic properties, *i.e* the instantaneous elastic modulus E_0, which was determined employing the Oliver and Pharr method [Oliver and Pharr, 1992], and the Poisson's ratio ν_0 [Vandamme and Ulm, 2006]. A suitable Poisson's ratio ν_0 of 0,3 was chosen based on previous literature [Rho et al., 1997, Rho et al., 2002, Zysset et al., 1999, Fan and Rho, 2003]. We moreover assumed that the Kelvin element of the model is incompressible ($\nu_1 = 0{,}5$).

The data files exported from the nanoindenter software were analyzed

using a Python program. Python is a free, cross-platform, open source programming language that is well recognized as effective and powerful.

2.1 Testing Methods

A variety of testing procedures have been used for nanoindentation of bone. Two of the most commonly used methods include ramp-and-hold and dynamic measurements analysis (DMA). Because bone exhibits time-dependent behavior, properties are sensitive to strain rate and dynamic testing frequency [Oyen, 2011].

2.1.1 Ramp and Hold

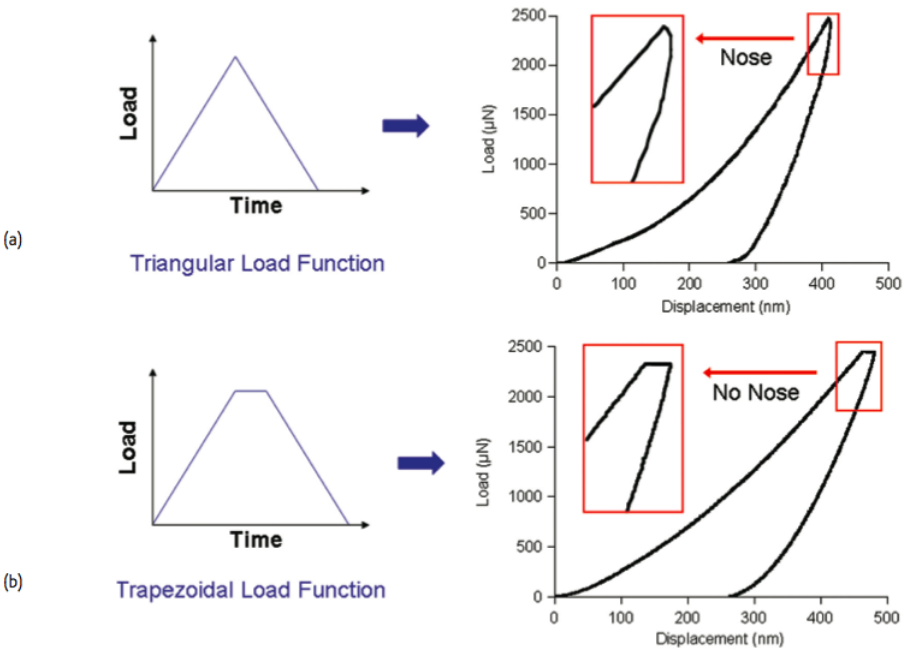

Figure 2.1: (a) Illustration of the nose effect resulting from indenting a viscoelastic material with a triangular load profile. (b) Illustration of the elimination of the nose effect by indenting a viscoelastic material with a trapezoidal load profile [Ebenstein and Pruitt, 2006].

In cases where creep behavior dominates the elastic response of the material, a 'nose' is observed on the indentation unloading curve, as illustrated in Figure 2.1 [Ebenstein and Pruitt, 2006]. A thorough discussion of this nose

phenomenon was presented by Briscoe et al. [Briscoe et al., 1998]. In short, it was found that when loading is followed by unloading without a hold at peak load, displacement increases slightly in the initial portion of the unloading phase, because the creep rate of the material is initially higher than the imposed unloading rate. This phenomenon results in a negative and changing slope in the initial unloading region (Figure 2.1). For this case, formula (1.37) would predict a negative indentation modulus M, which is obviously not admissible. To eliminate this nose, Biscoe and colleagues incorporated 10 s hold period at peak load into their applied load functions in order to allow the material to approach equilibrium prior to unloading. The effect of this hold period on load-displacement data is illustrated in Figure 2.1-b. Anyway, an appropriate hold time should be selected based on the creep and unloading rates used in the experiment. In fact, experimental indentation results show that the unloading stiffness S can be overestimated if the holding phase is too short [Chudoba and Richter, 2001] or if the unloading phase is too long [Feng and Ngan, 2002].

More rigorous nanoindentation methods that model the time-dependent behavior rather then allowing it to dissipate have been developed for viscoelastic materials. These include analysis of load-displacement data using creep compliance functions, three element standard solid models, and viscous-elastic-plastic models. In addition, many commercial nanoindenters have a dynamic testing option, where sinusoidal loads can be applied to measure storage and loss moduli as a function of loading frequency. These methods provide alternatives to quasi-static indentation with a trapezoidal load function, allowing direct measurement of time-dependent and frequency-dependent properties rather than measuring an equilibrium modulus [Ebenstein and Pruitt, 2006].

2.1.2 Dynamic Mechanical Analysis (DMA)

Recent advances in nanoindentation techniques have further improved the measurement of mechanical characteristics. Viscoelasticity can be studied using DMA during nanoindentation. The DMA is accomplished by imposing a small sinusoidal oscillation over the main loading function. This particular technique of repeated loading/unloading allows the measurement of contact stiffness at any point along the loading curve and not just at the point of unloading as in the conventional measurement, hence a single load-unload cycle is needed. This way mechanical properties such as hardness and Young's modulus as a function of depth can be obtained. Moreover, DMA can reveal information about storage and loss moduli for viscoelastic materials due to measurement of phase shift between loading force and displacement [Li and

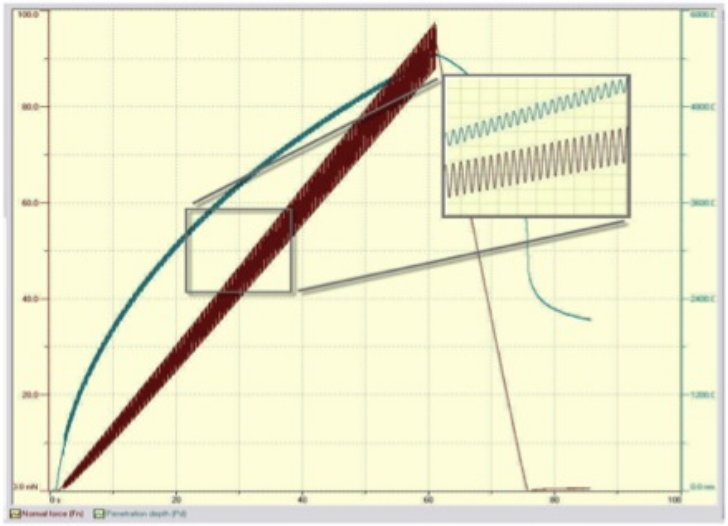

Figure 2.2: Schematic drawing of load and penetration depth versus time in the sinus mode [Instruments, 2010].

Bhushan, 2002, Instruments, 2010].

2.1.3 The Oliver and Pharr method

A typical load versus displacement curve resulting from a standard nanoindentation protocol can be seen in Figure 2.3. The three most important quantities that can be measured using the indentation force *vs.* indentation depth, $P - h$ curve are: the maximum load, P_{max}, the maximum displacement, h_{max}, and the contact stiffness at the beginning of the unloading $S = \frac{dP}{dh}\big|_{h=h_{max}}$, which is the slope of the initial portion of the unloading curve.

As the indenter is driven into the material, both elastic and plastic deformations occur: the result is the formation of a hardness impression, which is conformed to the indenter shape at the contact depth h_c. During the withdrawn of the indenter, only the elastic part of the deformation is recovered. A key assumption in the Oliver-Pharr method is that the test specimen behaves purely elastically during its unloading. The first step in the data analysis procedure is the unloading curve fitting to the power-law relation:

$$P = \alpha(h - h_f)^m \tag{2.1}$$

Where α and m are power law fitting parameters, and h_f is the final displacement after complete unloading, which is also determined by fitting

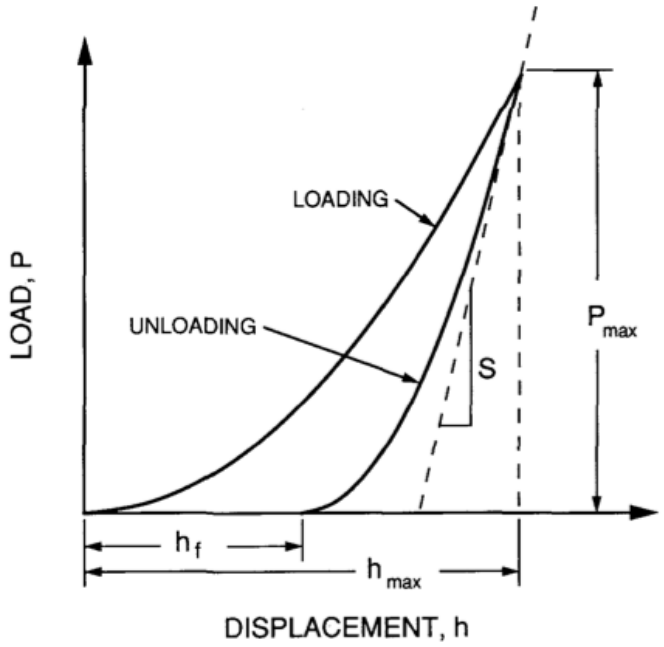

Figure 2.3: A schematic representation of load versus indenter displacement data for an indentation load; h_{max} represents the indenter displacement at peak load; h_f represents the final depth of the contact impression after unloading; and S is the initial unloading stiffness [Oliver and Pharr, 1992].

procedure. By evaluating the differentiated expression form of this expression at the maximum displacement, h_{max}, the unloading stiffness can be determined:

$$S = \left.\frac{dP}{dh}\right|_{h=hmax} = m\alpha(h_{max} - h_f)^{m-1} \tag{2.2}$$

From the load-displacement curve also the contact depth is estimated using:

$$h_c = h_{max} - \epsilon\frac{P_{max}}{S} \tag{2.3}$$

where ϵ is an indenter geometry-dependent constant, which assumes the value 0,75 for a spherical indenter, as stated by means of empirical studies [Oliver and Pharr, 1992, Fischer-Cripps, 2011]. The value for the pyramidal indenters should theoretically be 0,72 but it has been shown that a value of 0,75 better represents experimental data [Fischer-Cripps, 2011]. Determining the contact area involves evaluating an empirically derived indenter area

function for the indenter tip used throughout the experimental procedure. This contact area is function of the contact depth h_c, and can be expressed as $A = f(h_c)$. This shape function relates the cross.sectional area of indenter to the distance h_c from its tip. For a spherical indenter, the area of contact is given by:

$$A = \pi(2R_i h_c - h_c^2) \approx 2\pi R_i h_c \tag{2.4}$$

where the approximation is appropriate when the indentation depth is small compared to the radius of the indenter R_i. For a geometrically perfect Berkovich indenter with semi-angle θ, the area of contact is given by:

$$A = 3\sqrt{3}h_c^2 \tan^2\theta \tag{2.5}$$

In indentation testing, pyramidal indenters are generally treated as conical indenters with a cone angle that provides the same area to depth relationship as the actual indenter in question. Particularly, a cone semi-angle of $\alpha = 70.3°$ gives the same area to depth ratio as a triangular Berkovich indenter with semi-angle of $\theta = 65.27°$ [Fischer-Cripps, 2011].

Finally, the indentation hardness H_{IT} and the reduced modulus E_r, follow from:

$$H_{IT} = \frac{P_{max}}{A} \tag{2.6}$$

and

$$E_r = \frac{\sqrt{\pi}}{2\beta}\frac{S}{\sqrt{A}} \tag{2.7}$$

Where β is an indenter geometry-dependent costant. β has been empirically determined and is equivalent to 1,034 and 1 for Berkovich and spherical tip respectively [Fischer-Cripps, 2011].

The reduced modulus is used to account for elastic displacements occurring in both the indenter and the sample during indentation. A second expression for the reduced modulus allows the determination of the actual modulus of each of the respective materials to be calculated once the reduced modulus has been determined. This expression is given by:

$$\frac{1}{E_r} = \frac{1}{E_{IT}} + \frac{1-\nu_i^2}{E_i} \tag{2.8}$$

where ν_i and E_i are the Young's modulus and the Poisson's ratio of the indenter, which is commonly made with diamond ($E_i = 1141\,\text{GPa}$ and

$\nu_i = 0{,}07$). E_{IT} is the indentation modulus, which, for isotropic and rate-independent (nonviscous) materials, is related to the elastic modulus E and Poisson's ratio ν of the specimen by:

$$\frac{1}{E_{IT}} = \frac{1-\nu^2}{E} \tag{2.9}$$

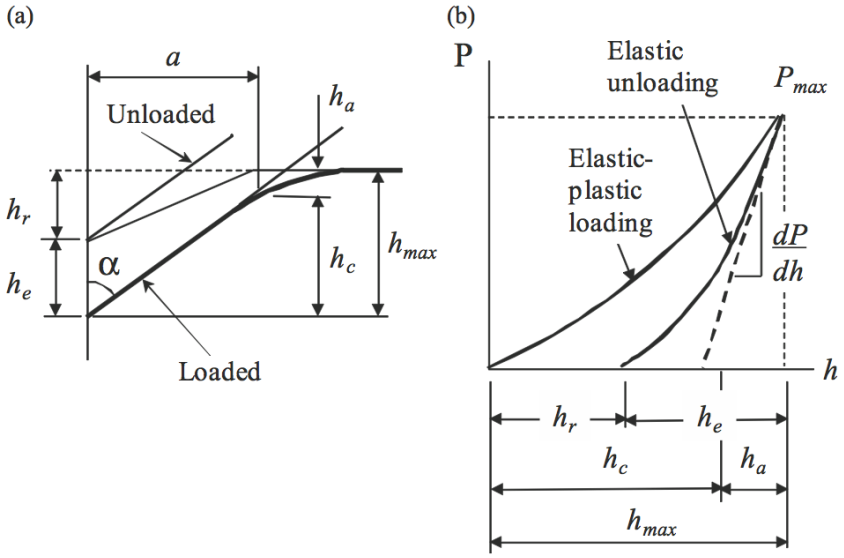

Figure 2.4: (a) Schematic of indenter and specimen surface at full load and unload for a conical indenter. (b) Load versus displacement for elastic-plastic loading followed by elastic unloading. h_r is the depth of the residual impression, h_{max} is the depth from the original specimen surface at load P_{max}, he is the elastic displacement during unloading, and ha is the distance from the edge of the contact to the specimen surface at full load. Upon elastic reloading, the tip of the indenter moves through a distance h_e, and the eventual point of contact with the specimen surface moves through a distance h_a [Fischer-Cripps, 2011].

2.2 Viscoelastic solution

In the current work, two different analysis have been used to examine indentation with a Standard Linear Solid model for a conical [Vandamme and Ulm, 2006] and spherical indenter tip [Cheng et al., 2005] (see Subsec. 2.2.1 and 2.2.2). In this section, these empirical models for viscoelastic materials

are briefly reviewed. Afterwards, the model used in the CSM nanoindenter software during sinus mode measurements is described.

2.2.1 Vandamme-Ulm model

Vandamme and Ulm [Vandamme and Ulm, 2006] presented a framework of viscoelastic indentation analysis based on the method of functional equations, developed by Lee and Radok [Lee and Radok, 1960]. The analytical contact solution was also derived for trapezoidal load history in conical indentation (half-angle θ) on a halfspace composed of a linear viscoelastic material that can be described by the SLS creep model. The trapezoidal load history is defined by:

$$P(t) = P_{max}F(t); F(t) = \begin{cases} t/\tau_L & \text{for } 0 \le t \le \tau_L \\ 1 & \text{for } \tau_L \le t \le \tau_L + \tau_H \\ (\tau_L + \tau_H + \tau_U - t)/\tau_U & \text{for } \tau_L + \tau_H \le t \le \tau_L + \tau_H + \tau_U \end{cases} \tag{2.10}$$

Where P_{max} is the maximum indentation force, $F(t)$ is the normalized load history, and τ_L, τ_H and τ_U define the duration of the loading, holding and unloading phases, respectively. The dependent quantity of interest, the indentation depth h, depends on time t, the load history parameters (P_{max}, τ_L, τ_H, τ_U) defined by (2.10), the elastic properties (K_0, G_0 or E_0, ν_0), the viscous properties (G_V, η_V, η_M,...) and the indenter geometry which in the case of conical indentation reduces to the half-apex angle θ. The relevant solution invariants are defined as follows:

$$\frac{E_0 h^2(t)}{P_{max}} = \Pi\left(\frac{t}{\tau_L}, \frac{\tau_H}{\tau_L}, \frac{\tau_U}{\tau_L}, \nu_0, \frac{G_V}{E_0}, \frac{\eta_V}{E_0 t}, \frac{\eta_M}{E_0 t}, \ldots, \theta\right) \tag{2.11}$$

For an elastic material, relation (2.11) reduces to the classical Galin-Sneddon solution:

$$\frac{E_0 h^2(t)}{P_{max}} = \frac{\pi}{2}\frac{1-\nu^2}{\tan\theta}F(t) \Leftrightarrow h^2(t) = \frac{\pi}{2\tan\theta}\frac{P(t)}{M_0} \tag{2.12}$$

where $F(t)$ is the load-time history defined by (2.10). From the elastic solution, Vandamme and Ulm looked for a dimensionless solution of the viscoelastic problem in the form:

$$y(t) = \frac{2}{\pi}\frac{M_0 h^2(t)}{P_{max}} 4\tan\theta \tag{2.13}$$

where M_0 is the instantaneous indentation modulus defined by:

$$M_0 = 4G_0 \frac{3K_0 + G_0}{3K_0 + 4G_0} \tag{2.14}$$

Starting from the viscoelastic response to a Heaviside step load, the general dimensionless solution for any monotonically increasing load case is derived:

$$y(t) = \frac{2}{\pi} \frac{M_0 h^2(t)}{P_{max}} 4 \tan\theta y(t) = \frac{1}{P_{max}} \int_0^t Y(t-\tau) \frac{d}{d\tau} P(\tau)\, d\tau \tag{2.15}$$

where the fundamental step load solution $Y(t)$ is identified as the indentation creep function. Hence, once $Y(t)$ is known, the dimensionless indentation response $y(t)$ can be determined for any monotonically increasing load history. The step load response of the SLS model in given by:

$$Y(t) = 4 + \frac{M_0}{G_V} \left(1 - e^{-\frac{G_V t}{\eta_V}} \right) + \frac{M_0 (1-2\nu_0)^2}{E_0 + 3G_V} \left(1 - e^{-\frac{(E_0 + 3G_V)t}{3\eta_V}} \right) \tag{2.16}$$

Eq. (2.16) is characterized by two exponential terms defined by two distinct time scales, which can be identified as the characteristic creep time η_V / G_V and a time $\eta_V / (E_0/3 + G_V)$ resulting from a coupling between the instantaneous elastic properties and both the material relaxation and creep times. This show that indentation creep activates, at a material level. both creep and relaxation phenomena. Both exponential terms vanish as time t increases, so that the step load response tends to an asymptotic value:

$$\lim_{t \to \infty} Y(t) = 4 + \frac{M_0}{G_V} + \frac{M_0 (1-2\nu_0)^2}{E_0 + 3G_V} \tag{2.17}$$

Use the trapezoidal load history given by (2.10) in (2.15) yields during the loading:

$$y_L(t) = \frac{1}{P_{max}} \int_0^t Y(t-\tau) \frac{d}{d\tau} P_L(\tau)\, d\tau y_L(t) = \frac{1}{\tau_L} \int_0^t Y(t-\tau)\, d\tau \text{ for } t \leq \tau_L \tag{2.18}$$

In order to access the indentation response for the holding phase, the integral (2.15) needs to be evaluated for both the loading phase and the holding phase. Hence:

$$y_L(t) = \frac{1}{P_{max}} \int_0^{\tau_L} Y(t-\tau) \frac{d}{d\tau} P_L(\tau)\, d\tau + \frac{1}{P_{max}} \int_{\tau_L}^t Y(t-\tau) \frac{d}{d\tau} P_H(\tau)\, d\tau \tag{2.19}$$

That is:

$$y_L(t) = \frac{1}{\tau_L}\int_0^{\tau_L} Y(t-\tau)\,d\tau \quad \text{for } \tau_L \le t \le \tau_L + \tau_H \tag{2.20}$$

Substitution of (2.16) in (2.18) and (2.20) yields the loading response:

$$\begin{aligned} y_L(t) =& \frac{1}{\tau_L}\left(\left(4 + \frac{M_0}{G_V} + \frac{M_0(1-2\nu_0)^2}{E_0+3G_V}\right)t - \frac{\eta_V M_0}{G_V^2}\left(1 - e^{-\frac{G_V t}{\eta_V}}\right) - \frac{3\eta_V M_0(1-2\nu_0)^2}{(E_0+3G_V)^2}\right. \\ & \left.\times\left(1 - e^{-\frac{(E_0+3G_V)t}{3\eta_V}}\right)\right) \end{aligned} \tag{2.21}$$

and the holding response:

$$\begin{aligned} y_H(t) =& \left(4 + \frac{M_0}{G_V} + \frac{M_0(1-2\nu_0)^2}{E_0+3G_V} + \frac{\eta_V M_0}{G_V^2\tau_L}\left(1 - e^{-\frac{G_V\tau_L}{\eta_V}}\right)e^{-\frac{G_V t}{\eta_V}} + \frac{3\eta_V M_0(1-2\nu_0)^2}{(E_0+3G_V)^2\tau_L}\right. \\ & \left.\times\left(1 - e^{\frac{(E_0+3G_V)\tau_L}{3\eta_V}}\right)e^{-\frac{(E_0+3G_V)t}{3\eta_V}}\right) \end{aligned} \tag{2.22}$$

The holding response of the SLS model displays the two exponential terms of the indentation creep function (2.16). Both exponential terms vanish as time t increases, so that the holding response tends to the asymptotic value (2.17):

$$lim_{t\to\infty} y_H(t) = \lim_{t\to\infty} Y(t) \tag{2.23}$$

Analogously, the response for the unloading phase using the method of the functional equations is:

$$y_L(t) = \frac{1}{\tau_L}\int_0^{\tau_L} Y(t-\tau)\,d\tau - \frac{1}{\tau_L}\int_{\tau_L}^{t} Y(t-\tau)\,d\tau \quad \text{for } t \ge \tau_L + \tau_H \tag{2.24}$$

This gives:

$$
\begin{aligned}
y_U(t) = &\left(4 + \frac{M_0}{G_V} + \frac{M_0(1-2\nu_0)^2}{E_0+3G_V} + \frac{\eta_V M_0}{G_V^2 \tau_L}\left(1 - e^{-\frac{G_V \tau_L}{\eta_V}}\right) e^{-\frac{G_V t}{\eta_V}} - \frac{(1-2\nu_o)^2}{1-\nu_0^2}\frac{3M_0\eta_V}{(E_0+3G_V)^2\tau_L}\right. \\
&\times e^{-frac(E_0+3G_V)t3\eta_v}\left(e^{\frac{\tau_L(E_0+3G_V)}{3\eta_V}} - 1\right) - 4\frac{t-(\tau_L+\tau_H)}{\tau_L} - \frac{M_0}{G_V}\frac{t-(\tau_L+\tau_H)}{\tau_L} \\
&+ \frac{\eta_V M_0}{G_V^2\tau_L}\left(1 - e^{-\frac{G_V(t-(\tau_L+\tau_H))}{\eta_V}}\right) - (1-2\nu_0)^2\frac{M_0}{E_0+3G_V}\frac{t-(\tau_L+\tau_H)}{\tau_L} \\
&\left.+ \frac{3\eta_V M_0(1-2\nu_0)^2}{(E_0+3G_V)^2\tau_L}\left(1 - e^{-\frac{(E_0+3G_V)(t-(\tau_L+\tau_H))}{3\eta_V}}\right)\right)
\end{aligned}
\tag{2.25}
$$

The analytical solution performs very well at the beginning of the unloading part, while the displacements deviate from the P-h curves at the end of the unloading part. In fact, the analytical solutions are only valid as long as the contact area monotonically increase, i.e. during the loading and the holding phases. Nevertheless, the method of functional equations remains valid to calculate the initial unloading slope of the P-h curve.

The contact stiffness S, obtained after a loading and holding period from the P-h curve, is given by:

$$
S = \left.\frac{dP}{dh}\right|_{t=(\tau_L+\tau_H)^+} = \frac{\dot{P}(t=(\tau_L+\tau_H)^+)}{\dot{h}(t=(\tau_L+\tau_H)^+)} \tag{2.26}
$$

Recalling (2.12), the indentation rate $\dot{h}$ can be expressed in function of $y(t)$ and $\dot{y}(t)$:

$$
\dot{h}(t) = \frac{\dot{h}(t)}{4\sqrt{y(t)}}\sqrt{\frac{\pi}{2}\frac{P_{max}}{M_0\tan\theta}} \tag{2.27}
$$

In the case of a trapezoidal loading, the unloading rate is $\dot{P} = -P_{max}/\tau_U$, so that the contact stiffness (2.26) becomes:

$$
S = \left.\frac{dP}{dh}\right|_{t=(\tau_L+\tau_H)^+} = \frac{4\sqrt{y(t=(\tau_L+\tau_H)^+)}}{\dot{y}(t=(\tau_L+\tau_H)^+)\tau_U}\sqrt{\frac{2P_{max}M_0\tan\theta}{\pi}} \tag{2.28}
$$

or equivalently, recalling $A_c(t)/h^2(t) = 4/\pi\tan^2\theta$ in any conical indentation test into a linear viscoelastic material, during the contact are monotonically increases:

$$
S = \left.\frac{dP}{dh}\right|_{t=(\tau_L+\tau_H)^+} = S_0\left(\frac{-4}{\dot{y}(t=(\tau_L+\tau_H)^+)\tau_U}\right) \tag{2.29}
$$

where S_0 is the independent expression of (1.37):

$$S_0 = \frac{2}{\sqrt{\pi}} M_0 \sqrt{A_c(t = (\tau_L + \tau_H)^+)} \tag{2.30}$$

with A_c the projected contact area. Hence, viscous effects affect the actual contact stiffness through the dimensionless factor $-4/(\dot{y}\tau_U)$. To evaluate this factor, $y_U(t)$ needs to be determined for the unloading phase.:

$$\dot{y}_U(t = (\tau_L+\tau_H)^+) = \frac{d}{dt}\left(\frac{1}{\tau_L}\int_0^{\tau_L} Y(t-\tau)\,d\tau - \frac{1}{\tau_U}\int_{\tau_L+\tau_H}^{t} Y(t-\tau)\,d\tau\right)_{t=(\tau_L+\tau_H)^+} \tag{2.31}$$

Use of (2.31) in (2.29) allows to evaluate the deviation of the measurable contact stiffness S from the instantaneous contact stiffness S_0. In SLS model, $Y(t)$ is given by (2.16), and application of (2.31) in (2.29) yields:

$$\frac{S_0}{S} = 1 - \frac{\tau_U M_0}{4\tau_L G_V} e^{-\frac{G_V \tau_H}{\eta_V}} \left(1 - e^{-\frac{G_V \tau_L}{\eta_V}}\right) - \frac{\tau_U M_0 (1-2\nu_0)^2}{4\tau_L (E_0 + 3G_V)} e^{-\frac{(E_0+3G_V)\tau_H}{3\eta_V}} \left(1 - e^{-\frac{(E_0+3G_V)\tau_L}{3\eta_V}}\right) \tag{2.32}$$

For $\tau_U > 0$, a viscous stiffening of the measurable contact stiffness is observed, $S \geq S_0$. To reduce this error, the second term in Eq. (2.32) must be much smaller than unity. This allows to derive the following criterion for the unloading time:

$$\tau_U \ll 4\tau_L \left[\frac{M_0}{G_V} e^{-\frac{G_V \tau_H}{\eta_V}} \left(1 - e^{-\frac{G_V \tau_L}{\eta_V}}\right) + \frac{M_0 (1-2\nu_0)^2}{E_0 + 3G_V} e^{-\frac{(E_0+3G_V)\tau_H}{3\eta_V}} \left(1 - e^{-\frac{(E_0+3G_V)\tau_L}{3\eta_V}}\right)\right]^{-1} \tag{2.33}$$

The unloading time criterion of the SLS model depends on both the loading and the holding times, τ_L, and τ_H, in addition to the viscoelastic properties of the indented material (E_0, ν_0, G_V, η_V) and to the related characteristic times of the SLS model, η_V/G_V and $\eta_V/(E_0/3 + G_V)$. The greater τ_L, and τ_H, the longer the unloading phase can be. Hence, the closer the indentation response during loading and holding is to its asymptotic value (2.23), the less do viscous effects affect the initial unloading response.

2.2.2 Cheng model

Cheng et al. [Cheng et al., 2005] presented a framework of viscoelastic indentation analysis based on the method of functional equations, developed by

Lee and Radok [Lee and Radok, 1960]. The analytical solution was derived for approximating relaxation testing and creep testing in spherical indentation (radius R) on a half-space composed of a linear viscoelastic material that can be described by the SLS creep model. For convenience in presenting the formulas, three dimensionless parameters a, b and c are introduced:

$$a = \frac{3K_0 + 4G^*}{3K_0 + 4G_0}\,, \quad b = \frac{6K_0 + 2G^*}{6K_0 + 2G_0}\,, \quad c = \frac{6K_0 + 2G_0}{3K_0 + 4G_0}\,, \tag{2.34}$$

where

$$G^* = \frac{G_0 G_1}{G_0 + G_1}\,. \tag{2.35}$$

The other three parameters employed by Cheng et al. are defined as:

$$t_r = \frac{\eta}{G_0 + G_1}\,, \quad t_c = \frac{\eta}{G_1}\,, \quad m = (2G_0)c\,. \tag{2.36}$$

The constants a, b, c, t_r, t_c and m all depend solely on material properties. In a creep test, the indenter is loaded to a certain value P_{max}, which is maintained there-after. The solution during the creep is derived assuming that the load changes instantaneously by a step:

$$h(t) = \sqrt[3]{\frac{9P_{max}^2}{16Rm^2}}\big(A_c\, e^{-\alpha_c t} + B_c\, e^{-\beta_c t} + C_c\big)^{2/3} \tag{2.37}$$

where

$$A_c = \frac{\big(1 - \frac{t_c}{t_r}\big)\big(a - \frac{t_r}{t_c}\big)}{\big(b - \frac{t_r}{t_c}\big)}\,, \;\; B_c = \frac{\big(b - a\big)\big(b - 1\big)}{b\big(b - \frac{t_r}{t_c}\big)}\,, \;\; C_c = \left(\frac{a}{b}\right)\left(\frac{t_c}{t_r}\right) \tag{2.38}$$

and

$$\alpha_c = 1/t_c\,, \quad \beta_c = b/t_r\,. \tag{2.39}$$

As can be verified,

$$A_c + B_c + C_c = 1\,. \tag{2.40}$$

This equation implies that at the initial moment the viscoelastic material has an instantaneous elastic response to a sudden change of load. It is assumed that the contact radius $r(t)$ is nondecreasing and $r(t) = \sqrt{u(t)R}$ holds at

every time instance. The nondecreasing $r(t)$ guarantees zero surface tractions outside the region of contact (see Lee and Radok, 1960), which represents the contact situation of interest.

When a sample is subjected to an arbitrary load history, that is:

$$P = P(t) \tag{2.41}$$

the indentation creep response can be obtained by applying the superpositional principle to the result of constant step load creep test, Eq. (2.37). This gives:

$$u(t) = \left(\int_0^t \frac{3}{4\sqrt{R}} J_c(t-\tau)\, dP(\tau) \right)^{2/3}, \tag{2.42}$$

where

$$J_c(t) = \frac{1}{m}\left(A_c\, e^{-\alpha_c t} + B_c\, e^{-\beta_c t} + C_c\right). \tag{2.43}$$

Use the trapezoidal load history given by (2.10) in (2.42) yields the loading response:

$$h(t) = \left[\frac{3}{4m\sqrt{R}} \frac{P_{max}}{\tau_L} \left(\frac{A_c}{\alpha_c} e^{-\alpha_c t}\left(e^{\alpha_c t} - 1\right) + \frac{B_c}{\beta_c} e^{-\beta_c t}\left(e^{\beta_c t} - 1\right) + C_c\, t \right) \right]^{2/3} \tag{2.44}$$

the holding response:

$$h(t) = \left[\frac{3}{4m\sqrt{R}} \frac{P_{max}}{\tau_L} \left(\frac{A_c}{\alpha_c} e^{-\alpha_c t}\left(e^{\alpha_c \tau_L} - 1\right) + \frac{B_c}{\beta_c} e^{-\beta_c t}\left(e^{\beta_c \tau_L} - 1\right) + C_c\, \tau_L \right) \right]^{2/3} \tag{2.45}$$

and the unloading response:

$$\begin{aligned} h(t) = & \left[\frac{3}{4m\sqrt{R}} \frac{P_{max}}{\tau_L} \left(\frac{A_c}{\alpha_c} e^{-\alpha_c t}\left(e^{\alpha_c \tau_L} - 1\right) + \frac{B_c}{\beta_c} e^{-\beta_c t}\left(e^{\beta_c \tau_L} - 1\right) + C_c\, \tau_L \right) \right. \\ & - \frac{3}{4m\sqrt{R}} \frac{P_{max}}{\tau_U} \left(\frac{A_c}{\alpha_c} e^{-\alpha_c t}\left(e^{\alpha_c t} - e^{\alpha_c(\tau_L+\tau_H)}\right) + \frac{B_c}{\beta_c} e^{-\beta_c t}\left(e^{\beta_c t} - e^{\beta_c(\tau_L+\tau_H)}\right) \right. \\ & \left. \left. + C_c(t - \tau_L - \tau_H) \right) \right]^{2/3} \end{aligned} \tag{2.46}$$

The contact stiffness S, obtained after a loading and holding period from the P-h curve, is given by Eq. (2.26). In the case of a trapezoidal loading,

the unloading rate is $\dot{P} = -P_{max}/\tau_U$, and $\dot{h}$ at $t = (\tau_L + \tau_H)^+$ is determined:

$$\begin{aligned}\left.\frac{dh}{dt}\right|_{t=(\tau_L+\tau_H)^+} = \frac{2}{3}\left(\frac{3P_{max}}{4m\sqrt{R}}\right)^{2/3}\Bigg[\frac{A_c}{\alpha_c\tau_L}\left(e^{-\alpha_c\tau_H} - e^{-\alpha_c(\tau_L+\tau_H)}\right) + \frac{B_c}{\beta_c\tau_L}\left(e^{-\beta_c\tau_H}\right. \\ \left. - e^{-\beta_c(\tau_L+\tau_H)}\right) + C_c\Bigg]^{-1/3}\Bigg[-\frac{A_c}{\tau_L}\left(e^{-\alpha_c\tau_H} - e^{-\alpha_c(\tau_L+\tau_H)}\right) - \frac{B_c}{\tau_L}\left(e^{-\beta_c\tau_H}\right. \\ \left. - e^{-\beta_c(\tau_L+\tau_H)}\right) - \frac{1}{\tau_U}\Bigg]\end{aligned} \tag{2.47}$$

Hence:

$$\frac{S_0}{S} = \frac{\tau_U}{\tau_L}\frac{M_0}{m}\left[A_c\left(e^{-\alpha_c\tau_H} - e^{-\alpha_c(\tau_L+\tau_H)}\right) + B_c\left(e^{-\beta_c\tau_H} - e^{-\beta_c(\tau_L+\tau_H)}\right) + 1\right] \tag{2.48}$$

where S_0 is given in Eq. (2.30). Thus, the unloading time criterion which limits viscous phenomena to affect the elastic unloading response, is:

$$\tau_U \ll \tau_L\frac{m}{M_0}\left[A_c\left(e^{-\alpha_c\tau_H} - e^{-\alpha_c(\tau_L+\tau_H)}\right) + B_c\left(e^{-\beta_c\tau_H} - e^{-\beta_c(\tau_L+\tau_H)}\right) + 1\right]^{-1} \tag{2.49}$$

As in the Vandamme and Ulm model (see Section 2.2.1), the greater τ_L and τ_H, the longer the unloading phase can be.

2.2.3 Sinus Mode Procedure

The Sinus mode indentation is done at constant frequency f ($\omega = 2\pi f$) and the load applied is:

$$P(t) = f_1 t + P_0\cos(\omega t). \tag{2.50}$$

The differential equation for harmonic oscillations is given by:

$$m\ddot{x} + b\dot{x} + kx = P_0\cos(\omega t) \tag{2.51}$$

where m is the mass of the indenter, k the stiffness of the UNHT head spring and b the damping. These parameters have been determined and memorized during the dynamic calibration. The solution is a combination of general x_t and particular x_P term:

$$x(t) = x_t(t) + x_P(t) \tag{2.52}$$

The general term solution is necessary to match the starting conditions, but it always dies out with the time, while the particular solution will dominate. The solution is:

$$k - m\omega^2 + ib\omega = \frac{P_0}{x_0}e^{i\delta} = \frac{P_0}{x_0}(\cos(\delta) + i\sin(\delta)) \tag{2.53}$$

where

$$\text{real part of the solution: } k = m\omega^2 + \frac{P_0}{x_0}\cos(\delta) \tag{2.54}$$

$$\text{imaginary part of the solution: } b\omega = \frac{P_0}{x_0}\sin(\delta) \tag{2.55}$$

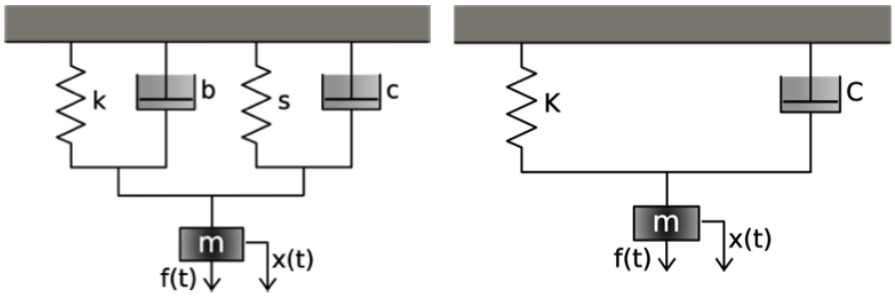

Figure 2.5: On the left: schematics of the UNHT head + indenter (left oscillator) in contact with the sample (right oscillator). On the right: schematics of the "big oscillator" (UNHT head + indenter in contact with the sample) [Instruments, 2010].

Introducing the UNHT head in contact with the sample will add to existing UNHT spring and damping oscillator another oscillator (the sample) in parallel with s (sample stiffness) and c (sample damping). For simplicity both oscillators can be regarded as one "big oscillator" with stiffness K and damping C (see Figure 2.5). The new equation for the "big oscillator" will be:

$$m\ddot{x} + C\dot{x} + Kx = P_0\cos(\omega t) \tag{2.56}$$

The K, S, k, m and s, c parameters are related to each other:

$$K = k + s \tag{2.57}$$

and

$$C\omega = c\omega + b\omega \tag{2.58}$$

Using Eq. (2.54) and (2.55) for oscillator parameters yields for "big oscillator":

$$\text{real part of the solution: } K = m\omega^2 + \frac{P_0}{X_0}\cos(\Phi) \tag{2.59}$$

$$\text{imaginary part of the solution: } C\omega = \frac{P_0}{X_0}\sin(\Phi) \tag{2.60}$$

During the measurements the response of the whole system (UNHT head and sample) is measured and parameters (K, S) of the whole oscillator are determined. In particular, the local stiffness S is given by the slope $\dot{,}P/\,dD_z$ during the unloading part of each cycle. At the same time phase shift δ between P and D_z is calculated. Knowing k, m and b for the UNHT head+indenter system and x_0 and P_0 from starting conditions, stiffness s and damping c can be calculated using Eq. (2.57), (2.58), (2.59) and (2.60), yielding to:

$$s = \frac{P_0}{x_0}\cos(\Phi) - (k - m\omega^2) \tag{2.61}$$

$$c\omega = \frac{P_0}{x_0}\sin(\Phi) - b\omega \tag{2.62}$$

The hardness and the Young's modulus are calculated using Eq. (2.6) and (2.7) respectively. The storage modulus is then calculated from Eq. (2.61) for stiffness, while the loss modulus from Eq. (2.62) for damping [Instruments, 2010]:

$$E' = \frac{\sqrt{\pi}}{2}\frac{s}{\sqrt{A_p(h_c)}} \tag{2.63}$$

$$E'' = \frac{\sqrt{\pi}}{2}\frac{c\omega}{\sqrt{A_p(h_c)}} \tag{2.64}$$

2.3 Experimental Procedures

Cutting and machining of bone samples can be a very time consuming step in preparation of bone specimens for nanoindentation. Certain factors, such as overheating and dehydration, need to be considered during this process. Moreover, factors such as sample surface roughness and inhomogeneities have a significant effect on the measured mechanical properties during indentation. In order to keep the samples in as close to physiological conditions as possible, samples were always kept hydrated throughout the preparation.

2.3.1 Sample preparation

Fresh adult compact bones from the femur mid-diaphysis were obtained from a 24 months old cow. The mid-part of femora was extracted using a handsaw. After removing the marrow, the femoral shaft was sectioned down to approximately 4 mm high prismatic pieces using a high precision diamond-coated band saw (EXAKT 300, EXACT, Norderstedt, Germany) under continuous water irrigation. Specimens were cut parallel and transverse to the bone axis (Figure 2.6). Osteons were cut approximately parallel and perpendicular to the Haversian canal axis in the transverse and axial specimens respectively (Figure 2.7). However, the longitudinal axis of the osteons can not be exactly determined.

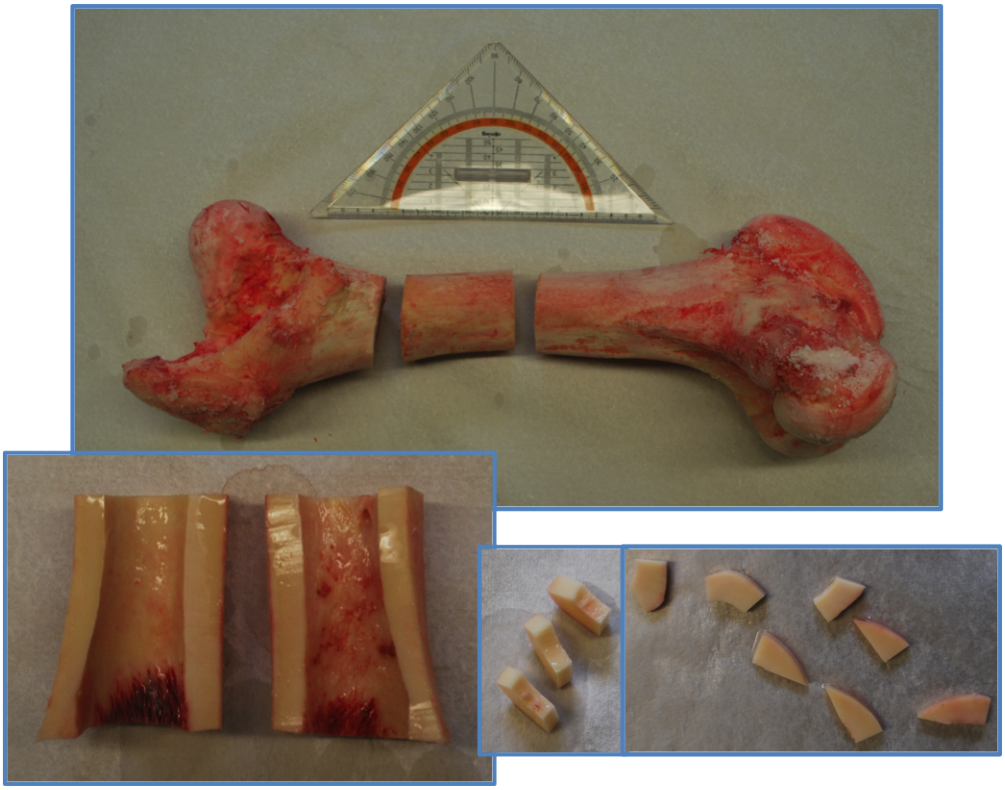

Figure 2.6: Bovine bone specimens preparation.

After all cutting procedures were completed, all samples were immediately placed in sealed plastic bags and stored at -20 ℃ until the embedding procedure. Polymethylmethacrylate (PMMA) was chosen as the embedding material and it is a low viscosity, infiltrating medium often used for mineralized tissue analysis. Embedding facilitates complete infiltration of the

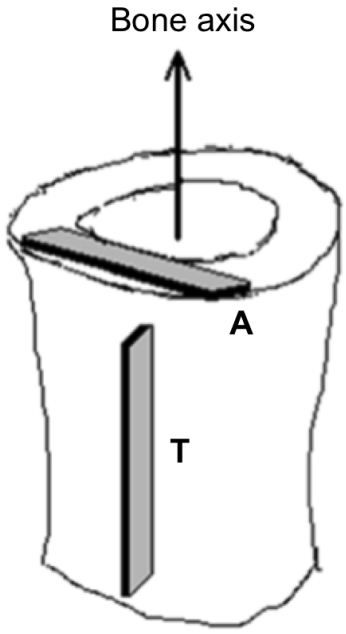

Figure 2.7: Bone specimens cut parallel (A) and perpendicular (T) to the bone axis (modified from [Sasaki, 2012]).

embedding medium into pore spaces, maintains tissue morphology and permits excellent surface preparation. PMMA was formed by mixing Pleximon 804 with Plexigum M 354 in the ratio 2 : 3. The PMMA was used to provide support during tests and has no effect on test results as long as no indents are made close to the bone-PMMA boundary. Tissue embedding is also useful for stabilizing the porous architecture of bone and, with a low Young's modulus of $\sim$ 5 GPa, is thought to minimally contribute to the measured mechanical properties of PMMA-embedded bone [Oyen, 2011].

Finally, the solution containing the MMA plastic was introduced into a home-designed mold (Figure 2.8) where a sample, covered by a thin layer of vaseline, was previously placed in with the surface to be indented laying on the bottom. Vaseline prevented water from escaping the bone and forming bubbles inside PMMA. The molds were then left for 30 minutes in an autoclave (Acryclave S, Dent-e-con, Germany) pressurized at 2 bar in order to minimize the formation of bubble during the polymerization of the embedding medium. Polymerization of methacrylate is an exothermic radical chain reaction, which is usually carried out at temperatures between 30 and 45℃ [Erben, 1997]. The samples were then embedded without thawing to avoid possible dehydration due to the high temperature, and without alcohol

fixation to avoid possible deterioration of the collagen. The molds consist of two symmetrical parts firmly screwed together, so that embedded specimen can be easily removed after unscrewing the screws. Yet the molds have an opening large enough to permit easy placement and manipulation of the specimen. PMMA tends to stick to metal molds unless they are highly polished. Add dimensions of the molds!

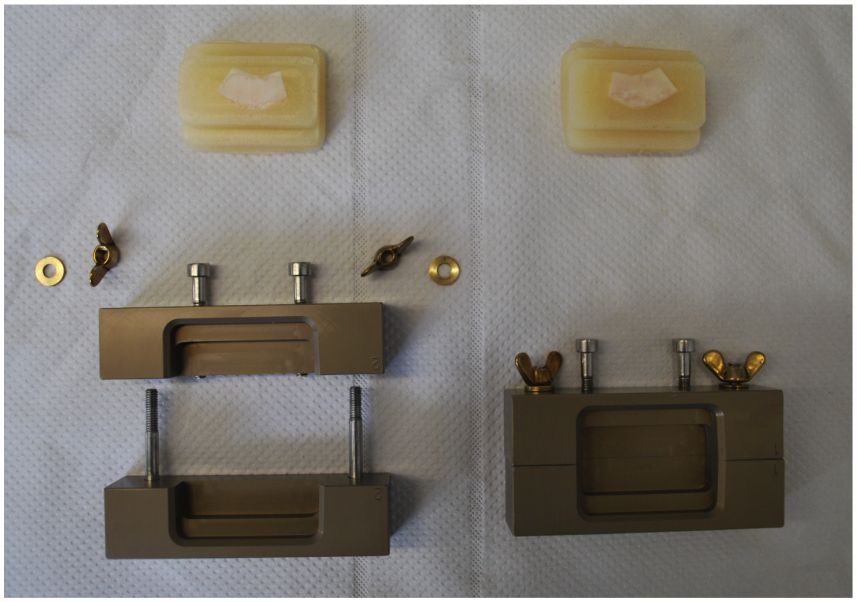

Figure 2.8: Home-designed molds used for specimens embedding.

The further surface preparation for nanoindentation was achieved in several steps following different protocols. The objective of using multiple protocols was to compare methods for bovine bone preparation requiring minimal sample manipulation, which would produce a flat plane with a small surface roughness.

After polymerization, specimens were mounted on a Leica sledge microtome (Leica SP2600, Leica Microsystems, Nussloch) with an ultramiller (Leica/Reichert-Jung Polycut E, Leica Microsystems, Nussloch, Germany) attachment. The ultramiller was employed in order to obtain two flat and parallel surfaces and to remove the possible thin layer of PMMA on bone's surface. The surface of the specimen with the bone was milled down with an increasing cutting depth. The rotational speed of the spindle was set at 500 rpm, which was found to be the ideal speed for milling bone, but not PMMA. To ensure high-quality final results the travelling speed of the sledge was also be adjusted according to the properties of the specimens. Some protocols required then the samples surfaces to be polished (LaboPol-5

Struers) with a diamond suspension paste embedded in a soft polishing cloth. During the polishing, lubricant blue (Struers) was used as lubricant. Moreover, after each polishing step the specimens were immersed in an ultrasonic bath (Ultrawave) for 3 minutes in order to remove debris. Also the machine was carefully cleaned between each polishing step using ethylene to avoid contamination of the follower smoother paper with rougher particles.

The bone was kept hydrated with 0.9% sodium chloride throughout cutting, milling and polishing. The samples were then kept frozen until testing. Unfortunately, there wasn't a protocol that was best for bovine bone embedded specimens, so some testing and optimization were necessary.

- Protocol n°1: the surface of the specimen was milled down with an increasing cutting depth finishing with four times 10 µm and two times 1 µm. The travelling speed of the sledge was set at 0.2 mm/s.

- Protocol n°2: the surface was milled as in protocol n°1. The sample was then subjected to ten minutes polishing using the 3 µm grit size polish, followed by another ten minutes polishing using 1 µm grit size polish.

- Protocol n°3: the surface was machined as in protocol n°2 and was then subjected to ten minutes final polishing using 0.25 µm grit size.

- Protocol n°4: the surface was milled as in protocol n°1 and afterwards polished for 3 minutes using 1 µm grit size polish.

- Protocol n°5: the surface was milled as in protocol n°1 and afterwards polished for 1 minute using 1 µm grit size polish.

- Protocol n°6: the surface was milled as in protocol n°1 and afterwards polished for 30 seconds using 1 µm grit size polish.

The specimens surfaces were therefore thoroughly examined and found to be slightly inclined. However a perfectly flat surface is required by the nanoindenter's tip-reference system. The ultramiller was adjusted by changing the spindle's inclination and replacing the sledge with a higher quality one. Afterwards new protocols were tested.

- Protocol n°1: the surface of the specimen was milled down with an increasing cutting depth finishing with two times 10 µm and two times 1 µm. The travelling speed of the sledge was set at 0.2 mm/s.

- Protocol n°2: the surface of the specimen was milled down with an increasing cutting depth finishing with two times 10 µm and two times 1 µm. The travelling speed of the sledge was set at 1 mm/s.

- Protocol n°3: the surface of the specimen was milled down with an increasing cutting depth finishing with two times 10 µm and two times 1 µm. The travelling speed of the sledge was set at 1.5 mm/s.

- Protocol n°4 the surface of the specimen was milled down with an increasing cutting depth finishing with two times 10 µm and two times 1 µm. The travelling speed of the sledge was set at 2 mm/s.

It was observed that milling larger bone samples size caused knife oscillations. New smaller samples were therefore obtained from the bigger ones and, before milling, the specimens edges were chamfered.

Finally, two different protocols were adopted for axial and transverse specimens preparation.

- Axial specimens were milled down with a 100 µm cutting depth, followed by two times 10 µm. The travelling speed of the sledge was set at 0.8 mm/s.

- Transverse specimens were milled down with a 100 µm cutting depth, followed by two times 10 µm. The travelling speed of the sledge was set at 0.8 mm/s.

The specimens tested in dry state were then air-dried in room conditions for 48 hours.

2.3.2 Sample imaging

After milling, the relevant structural features for the bovine femur cortical bone used in this research were characterized experimentally via Optical Microscopy (OM) and Atomic Force Microscopy (AFM). OM images were taken with M Plan Achromat-MPLN objective lens (Olympus Corporation, Shinjuku-ku, Tokyo, Japan) at 5x and 100x magnification. The Olympus microscopes are combined with the UNHT and provide excellent contrast and optimum flatness throughout the field of view. AFM imaging was performed using a Nanosurf (Nanosurf AG, Liestal, Switzerland).

2.3.3 Nanoindentation tests

All nanoindentation experiments were carried out in ambient condition (room temperature). An Ultra Nano Hardness Tester (UNHT) (CSM Instruments SA, Switzerland) with ultra low thermal drift, equipped with acoustic damping enclosure, was used throughout the duration of this present work. The UNHT uses the top surface reference technique and offers load and displacement resolution of 0.01 µN and 0.001 nm respectively. The UNHT is based on the principle of using an axis of measurement and an axis of reference, each one having its own actuator and its own sensors of depth and force. It is therefore possible to carry out active referencing of the surface of the sample. The use of the sapphire reference ring obviates the errors introduced by effects of temperature variation/thermal drift and frame deflection. In addition, a rapid approach speed can be used resulting in test times, which are in this system 10 to 50 times faster than other conventional nano indentation systems [Zioupos, 2005]. The instrument is housed in an acoustic damping enclosure so as to minimize instabilities due to the ambient background noise.

The indenter tips chosen were a Berkovich and a spherical diamond indentation tips (CSM, Switzerland), with defined elastic modulus of 1140 GPa and Poisson's ratio equal to 0,07.

A suitable Poisson's ratio for the test samples of 0,3 was chosen based on previous literature [Rho et al., 1997, Rho et al., 2002, Zysset et al., 1999, Fan and Rho, 2003].

All indentation locations were selected within plexiformal regions and with a 50 000 µm spacing using instrument's internal microscope. The interindent spacing was sufficiently large for minimal interference with a neighboring residual inelastically deformed zone as well as residual stresses.

Two kinds of configurations were tested: "dry indentations", in which the samples were stored and indented under atmospheric conditions, and "wet indentations", in which a fluid cell was employed in order to keep the sample (and part of the indenter) immersed in saline solution during testing. For both cases the same longer indenters were used.

Four sets of experiments have been carried out for each configuration:

- Set n°1: trapezoidal load. Three different penetration depths have been explored: 1000, 1500 and 2000 nm with Berkovich tip, and 500, 750 and 1000 nm with spherical tip. 30 indentations were performed at each penetration depth. Loading and unloading were performed at constant loading/unloading rates (50 000 µm/s and 400 000 µm/s respectively) and holding time was 30 s at each peak load level. A total of around 360 indentations were carried out for this set of experiments. Wu et al. [Wu et al., 2011] showed that the creep rate decreased with

holding time during the first 10 s, and fell below 5 nm/s after a 30 s holding period. As such, a 30 s holding period was chosen for each experiment set. Moreover, conventional nanoindentation techniques use a fast unloading rate in order to minimize the influence of time dependent deformation on calculated indentation modulus. Examples of the resulted load-displacement curves for both Berkovich indenter and spherical indenter are shown in Figure 2.9.

- Set n°2: five step procedure. From the first set of experiments the mean peak load was calculated at each penetration depth. 30 indentations were then performed loading the indenter tip at each peak load (I), holding for 30 s (II), unloading to 10% of the peak load (III), holding for 30 s (IV) and finally unloading to zero (V). Loading and unloading were performed at 50 000 µm/s and 400 000 µm/s respectively. The response during dwell II serves for the determination of viscoelastic parameters, while the back-creep during the low load dwell IV serves for revealing the irreversible components of deformation and check the duration of reversible processes. As suggested by Mencik et al. [Mencík et al., 2011], the period IV should last about the same time as period II. A total of around 360 indentations were carried out for this set of experiments.

- Set n°3: DMA mode. Three different frequencies have been explored: 5, 25 and 50 Hz. The peak load was fixed to 50 000 µN for the Berkovich tip and to 80 000 µN for the spherical tip, and the sinus amplitude was set to the 10% of the peak load. Loading and unloading were performed at 50 000 µm/s and 400 000 µm/s respectively, and holding time was 30 s at each peak load level. A total of around 360 indentations were carried out for this set of experiments.

- Set n°4: progressive multi-cycle. The indenter tip is incrementally loaded and unloaded into the bone over a preselected number of intervals (Figure 2.10). For the Berkovich tip the first load was fixed to 20 000 µN, the unload to 2500 µN, the maximum load to 50 000 µN and the number of cycles to 7. For the spherical tip the first load was fixed to 32 000 µN, the unload to 4000 µN, the maximum load to 80 000 µN and the number of cycles to 8. Loading and unloading were performed at constant loading/unloading rates (50 000 µm/s and 400 000 µm/s respectively) and holding time was 30 s at each peak load and unload level. A total of around 120 indentations were carried out for this set of experiments.

2.3.4 Data analysis and statistical evaluation

For experimental set n°1, the indentation modulus E_{IT} and the hardness H_{IT} were computed from the unloading portion of each force-depth curve. Following the method of Oliver and Pharr (see Subsec. 2.1.3), the 60% of the unloading curve is fitted to the power function (2.1), where h_f and m are fitting parameters determined by a least squares fitting procedure, and α is related to them by:

$$\alpha = \frac{P_{max}}{(h_{max} - h_f)^m} \tag{2.65}$$

A Poisson's ratio $\nu_{diamond} = 0{,}07$ and an elastic modulus $E_{diamond} = 1141\,\text{GPa}$ were adopted as the diamond tip elastic parameters to calculate the indentation modulus E_{IT} from equation (2.8). The Vandamme-Ulm model and the Cheng model were used in order to extract the elastic and the viscous properties. The three model input values are the instantaneous elastic modulus E_0, which is assumed to be equal to the elastic modulus E, and the Poisson's ratios ν_0 and ν_1. ν_0 and ν_1 applied in the calculation were 0,3 and 0,5 respectively, considering the Kelvin-Voigt unit to be incompressible. E_1 and η were then calculated fitting the loading and the holding part of each force-depth curve, to the function (2.18) and (2.20) for the Berkovich indenter, and (2.44) and (2.45) for the spherical indenter. Moreover, it was verified that the unloading time criterions (2.33) and (2.49) had been met. The work W is a model-independent measurement, which can be easily calculated from the P-h curve (Figure 2.9). If the load is integrated with respect to the penetration depth, one finds:

$$W = \int P\,dh \tag{2.66}$$

The area under the loading and holding sections of the P-h curve gives the total work W_{tot} done by the device during indentation. The reversible elastic contribution to the total work, W_E, can be deduced from the area under the unloading curve, therefore, the energy absorbed by plastic deformation alone is then the difference between these, $W_P = W_{tot} - W_E$. The ratio, η_{IT}, of elastic work recovered during unloading to the total work, is expressed as a percentage and is given by [Fischer-Cripps, 2004]:

$$\eta_{IT} = \frac{W_E}{W_{tot}} 100 \tag{2.67}$$

For experimental set n°2, from the first three steps indentation modulus E_{IT}, hardness H_{IT}, Young's moduli E_0 and E_1, and viscosity η were calculated as explained for experimental set n°1. Additionally, creep and recovery

were measured as the change in depth of the indenter during the first and second holding time respectively. The area under the first two steps of the curve gives the total work W_{tot}, while the elastic work can be calculated from the remaining part of the curve.

In case of DMA measurements, as in experimental set n°3, the dynamic mechanical analysis allows for a continuous acquisition of hardness H_{IT}, reduced modulus E_{IT}, storage and loss modulus (E' and E'') data as a function of indentation depth.

For experimental set n°4, indentation modulus E_{IT}, hardness H_{IT}, creep, recovery, total work W_{tot} and elastic work W_E were calculated from each loading cycle as previously described.

Within experimental sets n°1 and n°2, the parameters calculated from different penetration depths were compared using two-ways ANOVA. Statistical analysis was performed with R [Team, 2008]

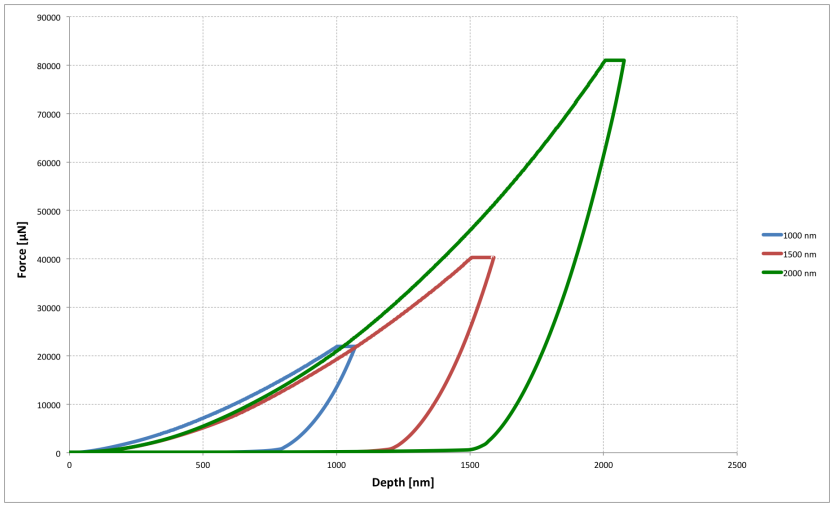

(a) Berkovich tip

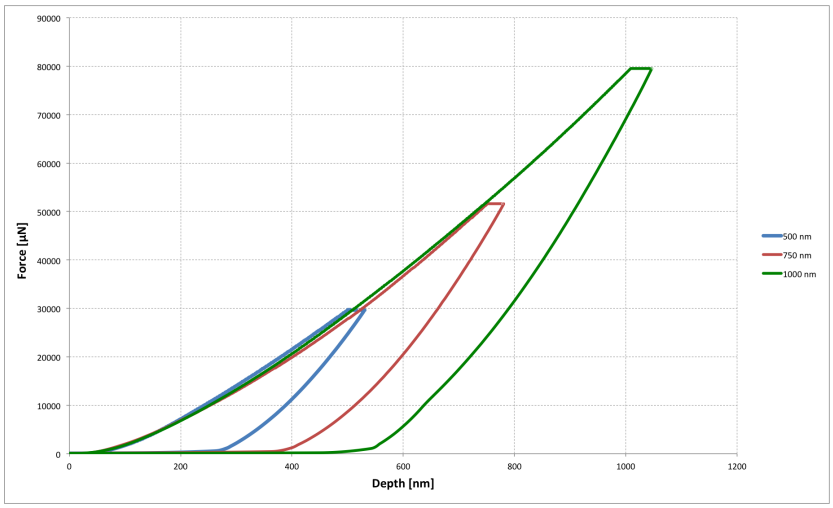

(b) Spherical tip

Figure 2.9: Example of *P-h* indentation curves for the Berkovich (a) and spherical (b) tips at the three tested maximum depths in the experimental set n°1.

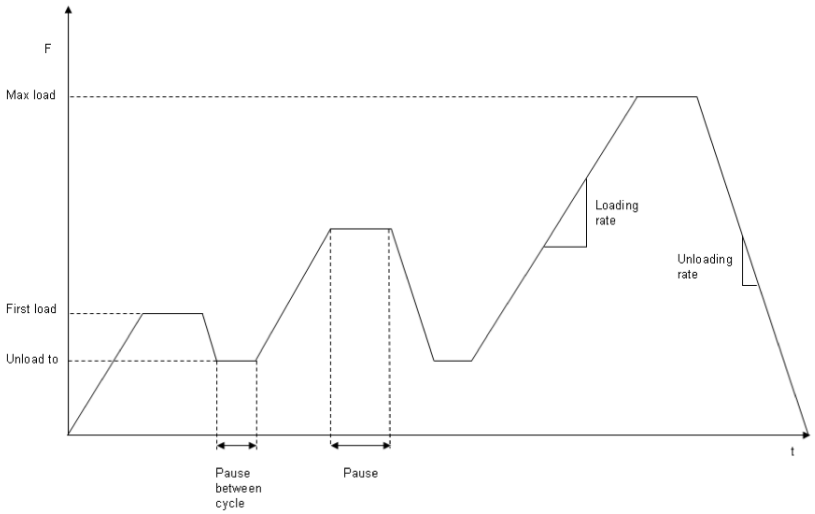

Figure 2.10: Load-time sequence with progressive multi-cycle mode. Example for 3 cycles [Instruments, 2010].

CHAPTER 3

Results

3.1 Results of Sample Preparation

Several protocols were tested in order to find an optimized specimens preparation.

In the first set of protocols, microcracks were observed on bone surface, probably due to the use of the lubricant blue, which is alcohol based and dehydrates the bone tissue [Erben, 1997]. Protocols with reduced polishing time were tested, but even after 30 s microcracks were still noticed.

Thus, in the second set of protocols, the polishing was avoided and, accordingly, the time in which specimens were out of saline solution decreased. After testing many different protocols, the transverse specimen surface looked still dark as shown in Figure 3.1, while the axial specimen surface appeared clear and bright especially in the osteonal regions (Figure 3.2). It was therefore decided not to test transverse specimens, but to focus on axial specimens.

Concerning the wet indentations, the specimen to be tested was removed from the freezer in the morning, left thawing out in saline solution for 2 hours and then milled. Care was taken not to freeze again the specimen after the milling and not to test the specimens after being absorbed in saline solution for more than 15 hours. In fact, it was noticed that freezing the milled specimen induces crack formation on bone surface, and that leaving the specimen in saline solution for a long period of time causes a "shoulder" at the beginning of the nanoindentation P-h curves.

After the specimen preparation described above, the surface of an in-

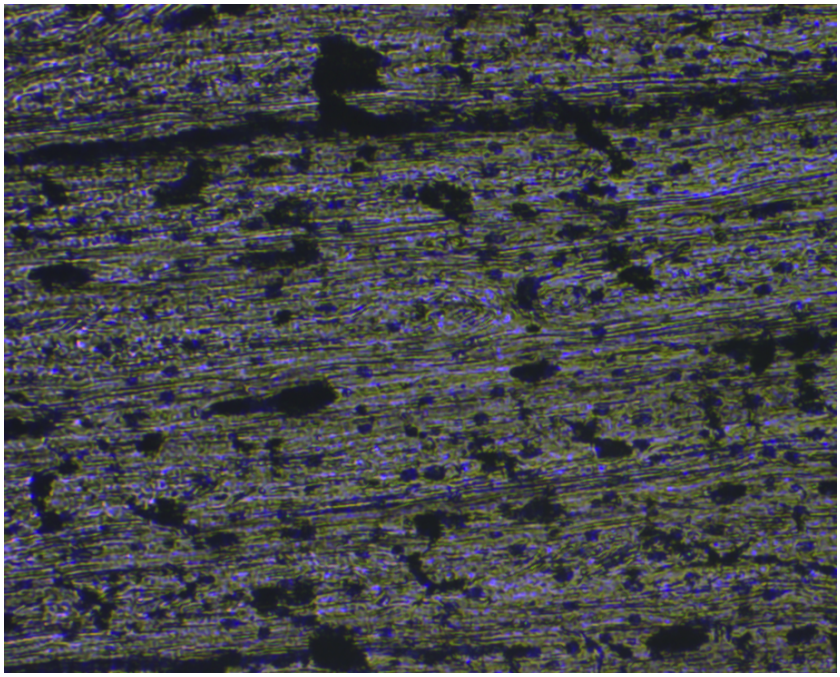

Figure 3.1: Optical microscopy image of transverse specimen after preparation with the final protocol.

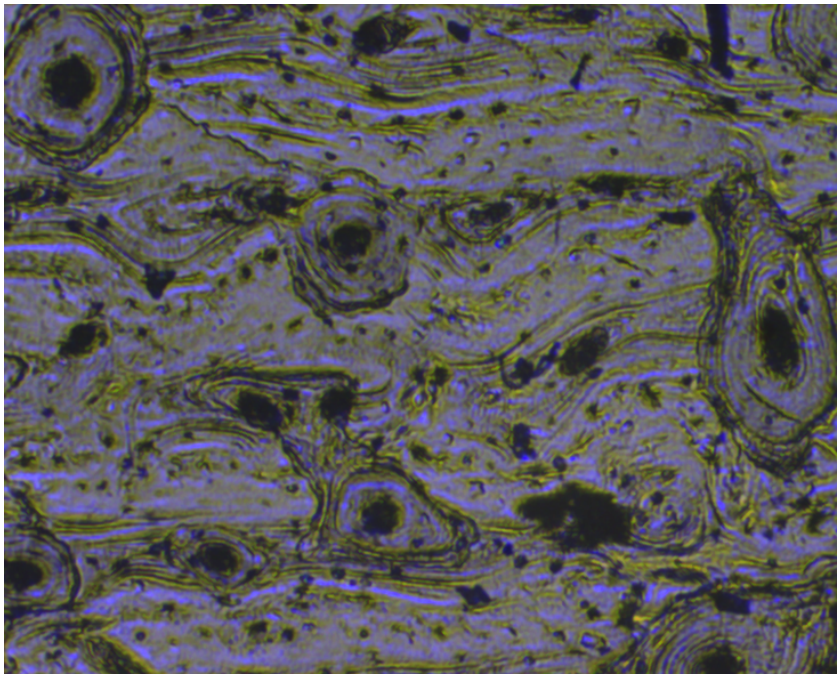

Figure 3.2: Optical microscopy image of axial specimen after preparation with the final protocol.

dented axial sample was characterized using an Atomic Force Microscope (AFM) and images are shown in Figure 3.3. Optical microscopic examination showed that all of the samples were generally plexiform but partly transformed into Haversian bone.

3.2 Results of Nanoindentation Tests

This section contains the results from nanoindentation experiments. Force-time and depth-time data was collected using protocols and procedures previously described in Chapter 2.3. The load-depth curves were studied individually in detail. In some cases, the curves exhibited obviously errors, probably due to indenting on or near an osteocyte lacuna or canalicula. These indents were identified and not used for further processing. The number of usable indentations for each testing procedure ranged from 28 to 32, with a median of 30.

3.2.1 Trapezoidal Load

In this Section, results obtained with experimental set n°1 are presented.

After experiments, the material sample surface was observed with help of OM (Figure 3.4).

60% of the unloading curve from the nanoidentation load-displacement data is used to calculate E_{IT} and H_{IT} of the sample (see Subsec. 2.1.3). Examples of the analytical fits are shown in figure 3.5. Mean and standard deviation of E_{IT} and H_{IT} as a function of the penetration depth are shown in Figure 3.6 and 3.7 for dry and wet samples respectively. Moreover, the ratio between H_{IT} and E_{IT} has been calculated (Figure 3.8 and 3.9). A linear regression model is used to fit the data, and the equation of the straight line is written on each graphic.

E_0 is assumed equal to elastic modulus E, while E_1 and η are calculated using the Vandamme-Ulm (for the Berkovich tip) and the Cheng (for the spherical tip) models (Figure 3.10). Means, standard deviations and linear regression fittings of these parameters are shown in Figure 3.11 and 3.12 for dry and wet samples respectively.

The ratio, W_{el}/W_{tot}, of elastic work recovered during unloading to the total work, is represented in Figure 3.13 and 3.14 as a function of the penetration depth.

Means and standard deviations of all the extracted values mentioned above are presented in Table 3.1. The results from two-way ANOVA test are shown in Tables 3.2 and 3.3.

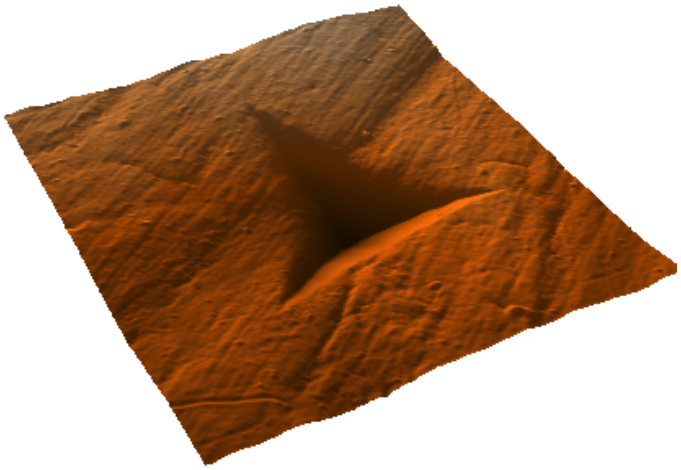

(a) Berkovich tip

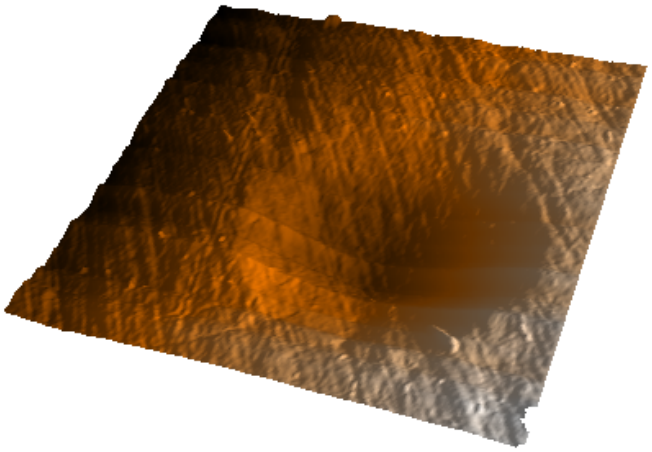

(b) Spherical tip

Figure 3.3: AFM images of bovine bone specimens indented in dry conditions with a Berkovich (a) and a spherical (b) tip. Images used with permission of J. Schwiedrzik.

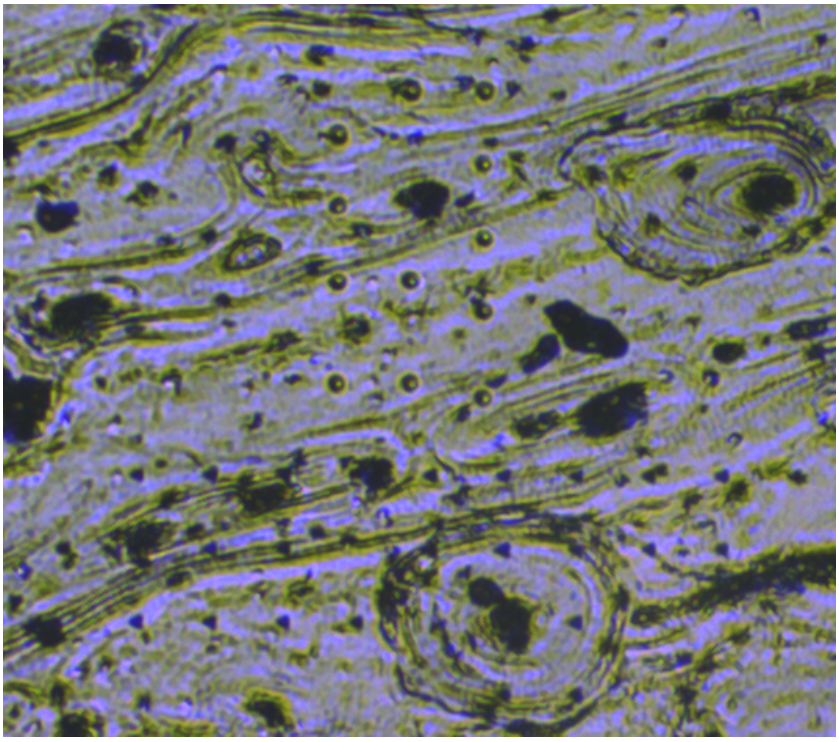

Figure 3.4: Example of optical microscopy image of bovine cortical bone after being indented with spherical (top) and Berkovich (bottom) tips in the experimental set n°1.

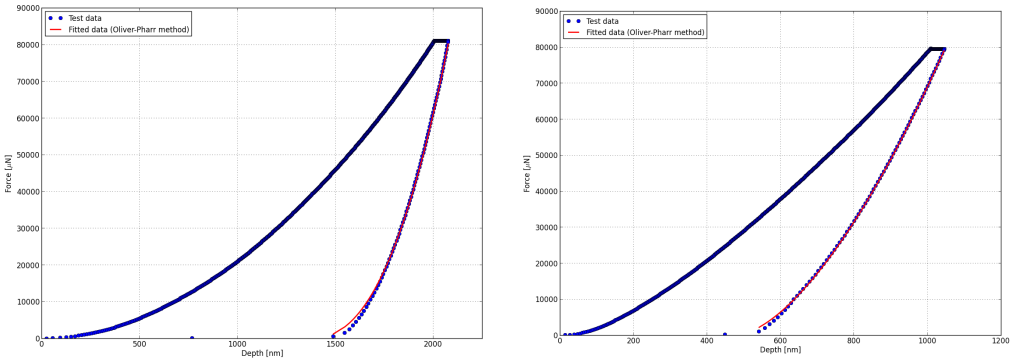

(a) Berkovich tip

(b) Spherical tip

Figure 3.5: Examples of P-h curves fitted for the unloading phases with the Oliver and Pharr method. Curves are taken from dry specimens indented with Berkovich (a) and spherical (b) tip and experimental set n°1

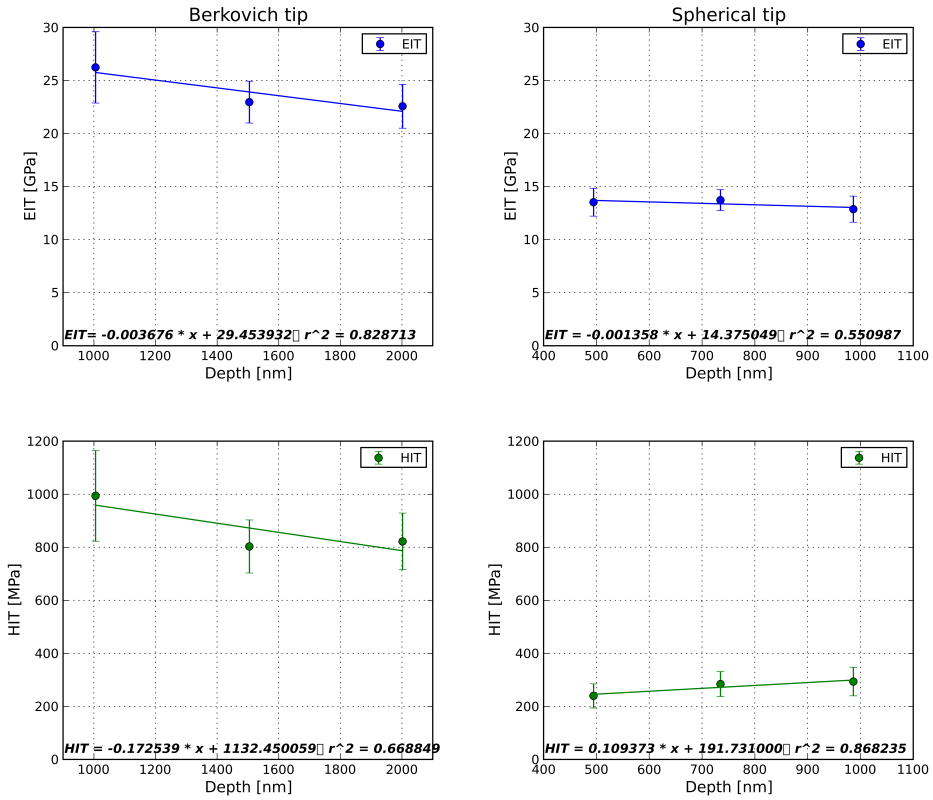

Figure 3.6: E_{IT} and H_{IT} (mean and standard deviation) of dry bovine bone samples calculated using a trapezoidal loading history. The equation written below each graphic represents the linear regression line.

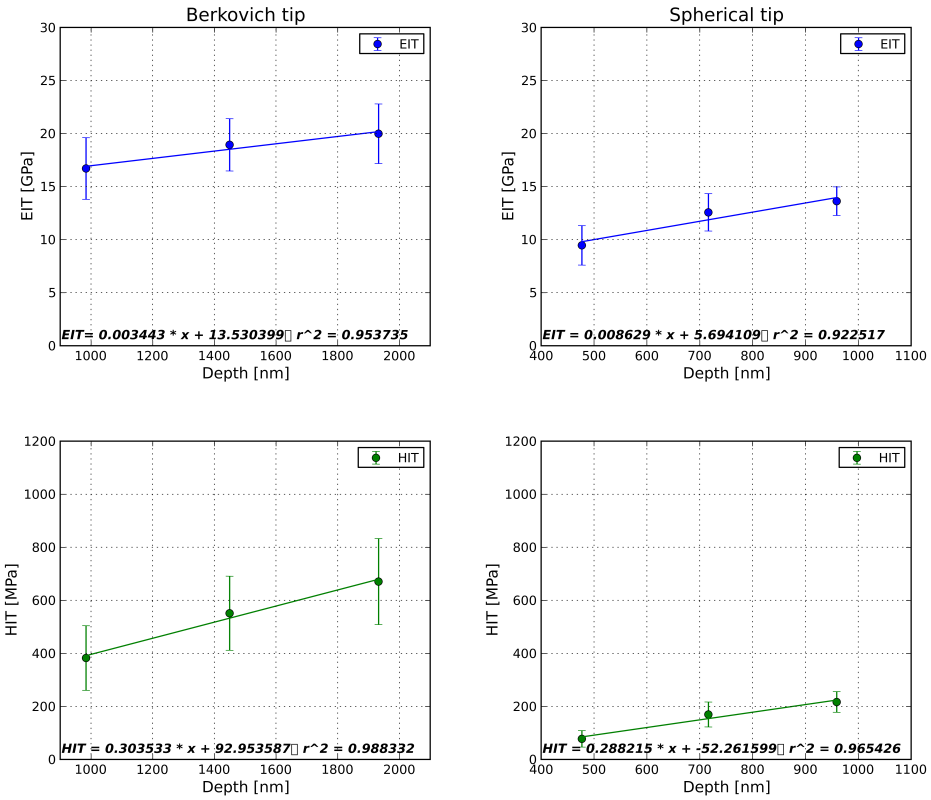

Figure 3.7: E_{IT} and H_{IT} (mean and standard deviation) of wet bovine bone samples calculated using a trapezoidal loading history. The equation written below each graphic represents the linear regression line.

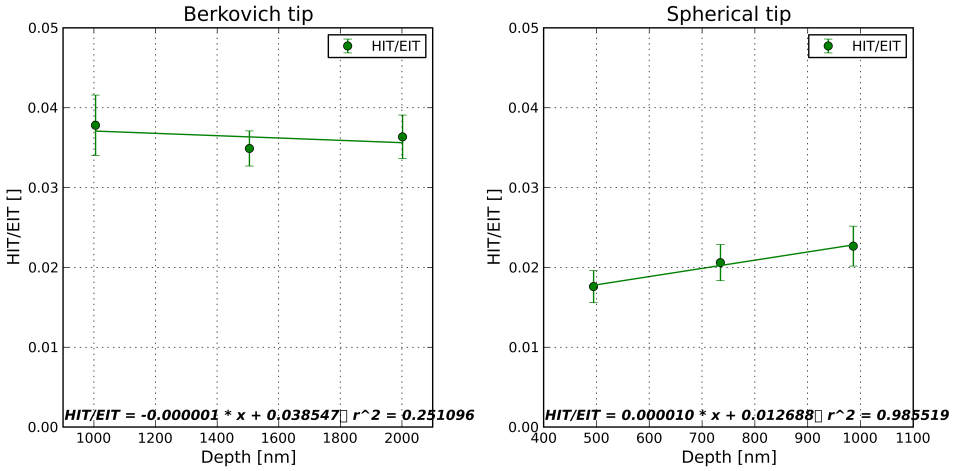

Figure 3.8: Ratio of H_{IT}/E_{IT} (mean and standard deviation) of dry bovine bone samples calculated using a trapezoidal loading history. The equation written below each graphic represents the linear regression line.

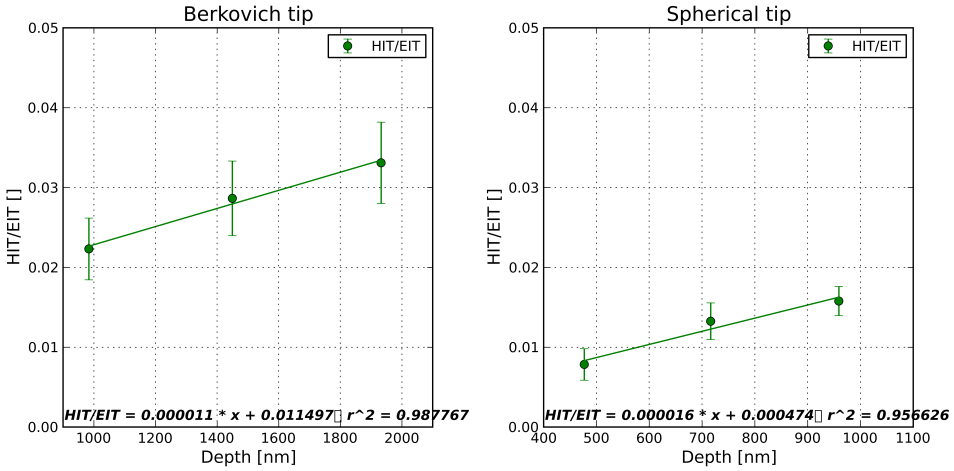

Figure 3.9: Ratio of H_{IT}/E_{IT} (mean and standard deviation) of wet bovine bone samples calculated using a trapezoidal loading history. The equation written below each graphic represents the linear regression line.

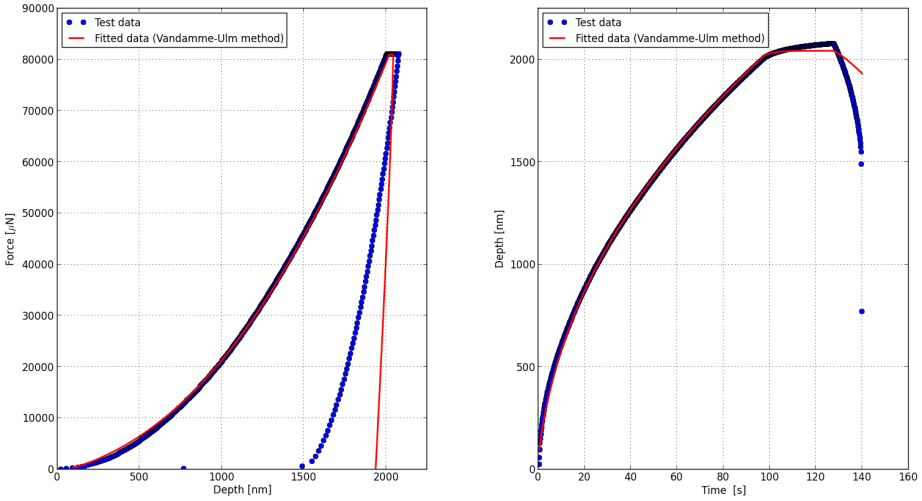

(a) Berkovich tip

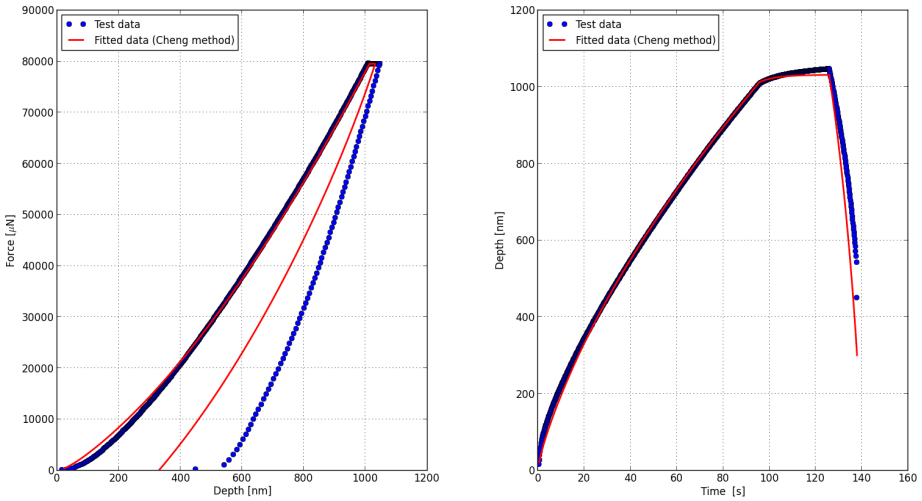

(b) Spherical tip

Figure 3.10: Examples of P-h (on the left) and h-t (on the right) curves fitted with the Vandamme-Ulm method and Cheng method. Curves are taken from dry specimens indented with Berkovich (a) and spherical (b) tip

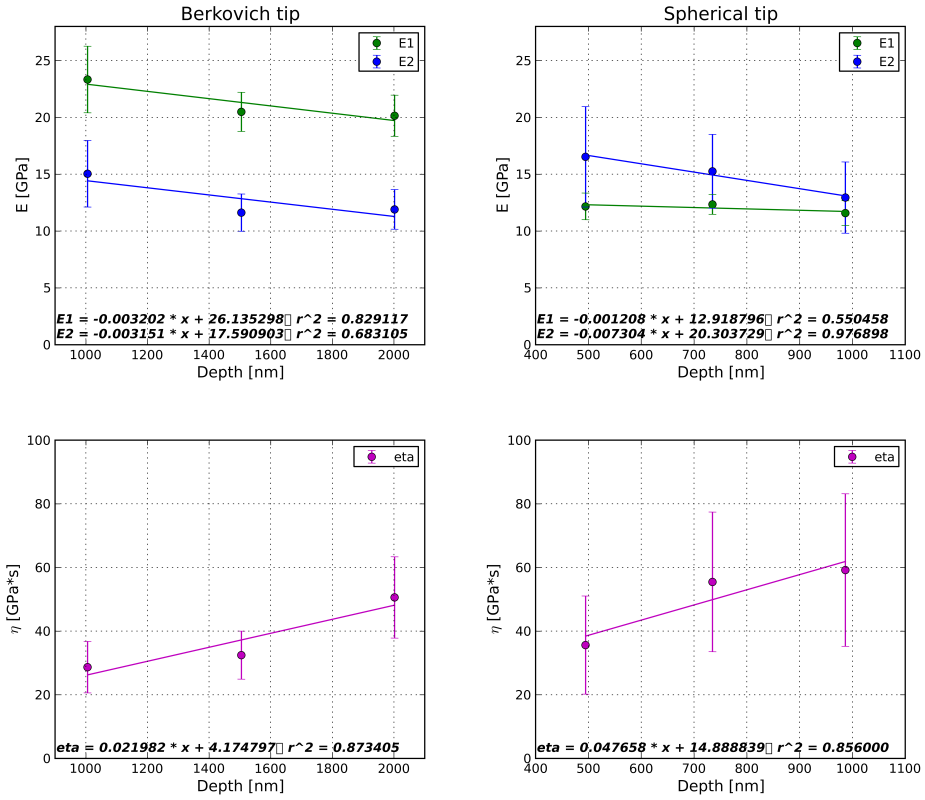

Figure 3.11: E_0, E_1 and η (mean and standard deviation) of dry bovine bone samples calculated using the Vandamme-Ulm method for the Berkovich tip and the Cheng method for the spherical tip. The equation written below each graphic represents the linear regression line.

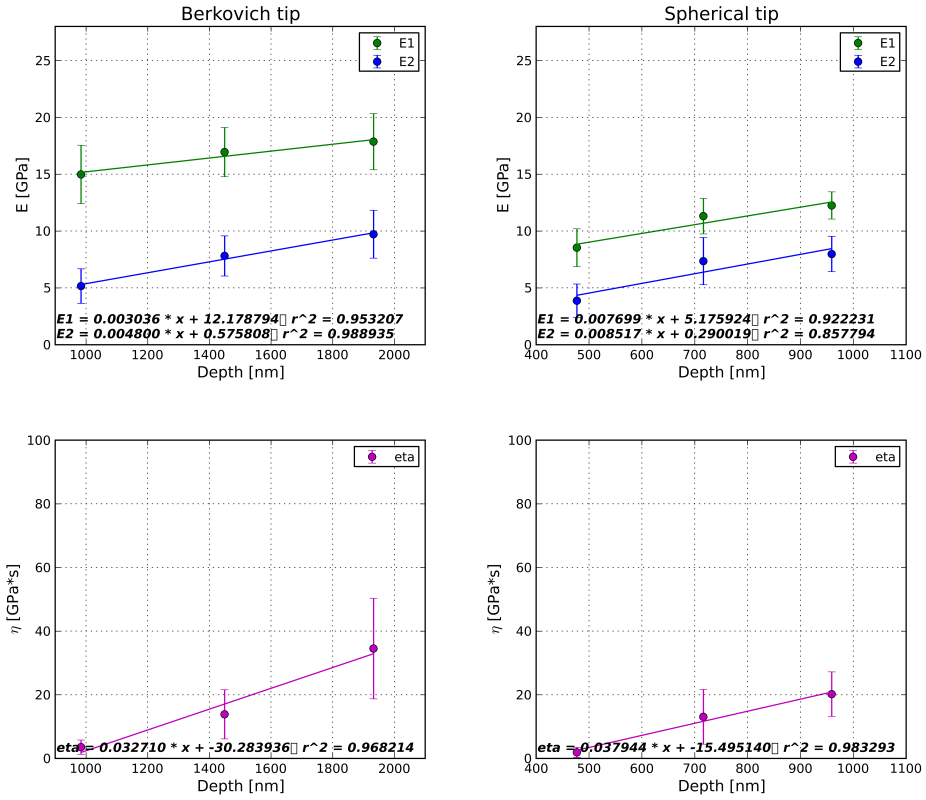

Figure 3.12: E_0, E_1 and η (mean and standard deviation) of wet bovine bone samples calculated using the Vandamme-Ulm method for the Berkovich tip and the Cheng method for the spherical tip. The equation written below each graphic represents the linear regression line.

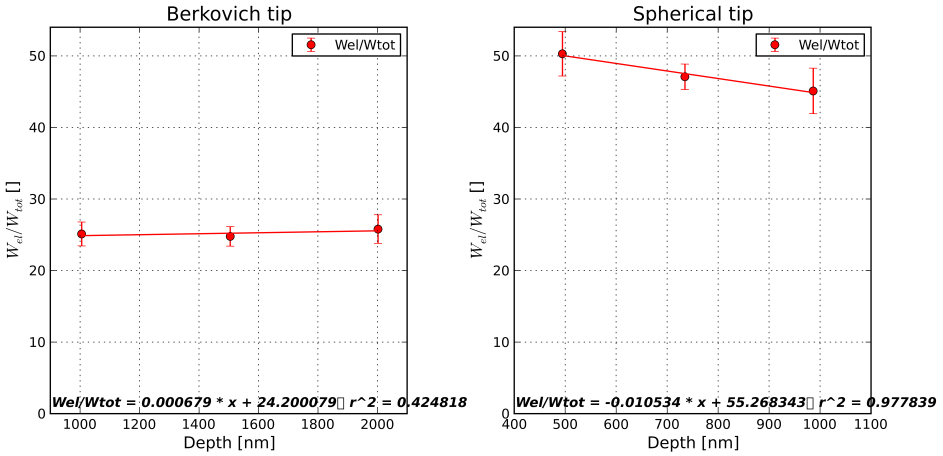

Figure 3.13: W_{el}/W_{tot} (mean and standard deviation) of dry bovine bone samples. The equation written below each graphic represents the linear regression line.

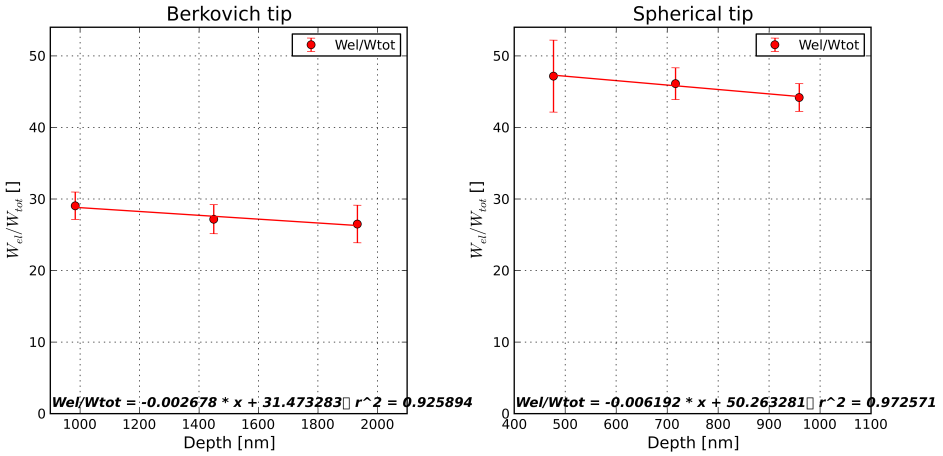

Figure 3.14: W_{el}/W_{tot} (mean and standard deviation) of wet bovine bone samples. The equation written below each graphic represents the linear regression line.

Table 3.1: Means and standard deviations (in brackets) of parameters calculated from experimental set n°1.

Tip	Depth [nm]	Dry/Wet	E_{IT} [GPa]	H_{IT} [MPa]	W_{el}/W_{tot}	E_1 [GPa]	E_2 [GPa]	η [GPa*s]
B	1000	D	26,24 (3,36)	993,83 (170,97)	25,11 (1,67)	23,33 (2,93)	15,04 (2,93)	28,68 (8,08)
		W	16,71 (2,90)	382,33 (121,68)	29,05 (1,91)	14,98 (2,57)	5,16 (1,52)	3,55 (2,25)
	1500	D	22,96 (1,97)	802,95 (100,19)	24,77 (1,37)	20,48 (1,72)	11,62 (1,64)	32,44 (7,55)
		W	18,94 (2,46)	550,97 (139,71)	27,18 (2,04)	16,95 (2,17)	7,81 (1,77)	13,88 (7,72)
	2000	D	22,58 (2,07)	822,04 (106,73)	25,79 (2,00)	20,14 (1,81)	11,90 (1,74)	50,60 (12,78)
		W	19,98 (2,81)	670,68 (162,03)	26,50 (2,62)	17,86 (2,47)	9,71 (2,11)	34,52 (15,64)
S	500	D	13,53 (1,32)	239,63 (45,52)	50,29 (3,11)	12,16 (1,17)	16,53 (4,41)	35,62 (15,42)
		W	9,46 (1,86)	77,57 (31,11)	47,16 (5,03)	8,53 (1,67)	3,87 (1,48)	1,91 (1,58)
	750	D	13,73 (0,99)	284,21 (47,08)	47,08 (1,78)	12,34 (0,88)	15,26 (3,25)	55,46 (21,94)
		W	12,57 (1,76)	169,39 (46,98)	46,12 (2,22)	11,31 (1,57)	7,36 (2,08)	13,06 (8,59)
	1000	D	12,86 (1,23)	293,72 (54,04)	45,10 (3,18)	11,58 (1,09)	12,94 (3,13)	59,19 (23,98)
		W	13,62 (1,35)	216,63 (39,08)	44,18 (1,94)	12,25 (1,20)	7,98 (1,55)	20,21 (6,13)

Table 3.2: Significance level of the indentation modulus investigated for results under both dry and wet conditions from experimental set n°1. Significance code: 0 '$***$', 0,001 '$**$', 0,01 '$*$', 0,05 '.', $>$ 0,1 ' '.

	p value	
Factors for indentation modulus		
Penetration depth	$< 2e-16$	$***$
Tip shape	$< 2e-16$	$***$
Hydration conditions	$< 2e-16$	$***$
Penetration depth vs. tip shape	0,0013	$**$
Penetration depth vs. hydration conditions	0,0149	$*$
Tip shape vs. hydration conditions	$< 2e-16$	$***$
Penetration depth vs. tip shape vs. hydration state	0,01391	

Table 3.3: Significance level of the parameters investigated for results under both dry and wet conditions from experimental set n°1. Significance code: 0 '$***$', 0,001 '$**$', 0,01 '$*$', 0,05 '.', $>$ 0,1 ' '.

	p value (Berkovich)		p value (spherical)	
Factors for H_{IT}				
Penetration depth	0,1988		$9{,}02e-5$	$***$
Hydration conditions	$<2e-16$	$***$	$<2e-16$	$***$
Penetration depth vs. hydration conditions	0,0089	$**$	0,0246	$*$
Factors for W_{el}/W_{tot}				
Penetration depth	0,850		$4{,}86e-8$	$***$
Hydration conditions	$2{,}58e-9$	$***$	0,2175	
Penetration depth vs. hydration conditions	0,909		0,0089	$**$
Factors for E1				
Penetration depth	0,9225		0,182	
Hydration conditions	$<2e-16$	$***$	$1{,}90e-13$	$***$
Penetration depth vs. hydration conditions	0,0020	$**$	$1{,}11e-8$	$***$
Factors for E2				
Penetration depth	0,2473		$5{,}35e-5$	$***$
Hydration conditions	$<2e-16$	$***$	$<2e-16$	$***$
Penetration depth vs. hydration conditions	0,0008	$***$	$9{,}37e-7$	$***$
Factors for η				
Penetration depth	$1{,}05e-5$	$***$	0,0029	$**$
Hydration conditions	$5{,}89e-10$	$***$	$6{,}84e-11$	$***$
Penetration depth vs. hydration conditions	$1{,}24e-7$	$***$	0,14052	

3.2.2 Five Step Procedure

In this Section, results obtained with experimental set n°2 are presented. The maximum load for each penetration depth and tip shape was set equal to the corresponding average maximum load calculated in experimental set n°1 (Table 3.4)

Table 3.4: Average maximum loads calculated from experimental set n°1 for each different tip shape, hydration condition and penetration depth.

Tip shape	Dry/Wet	Depth	Max load
Berkovich	Dry	1000 nm	22093,00
		1500 nm	40097,00
		2000 nm	70609,00
	Wet	1000 nm	8846,00
		1500 nm	31514,00
		2000 nm	66104,00
Spherical	Dry	500 nm	27600,00
		750 nm	50432,00
		1000 nm	72003,00
	Wet	500 nm	N.A.
		750 nm	33506,00
		1000 nm	57217,00

After experiments, the material sample surface was observed with help of OM (Figure 3.15.

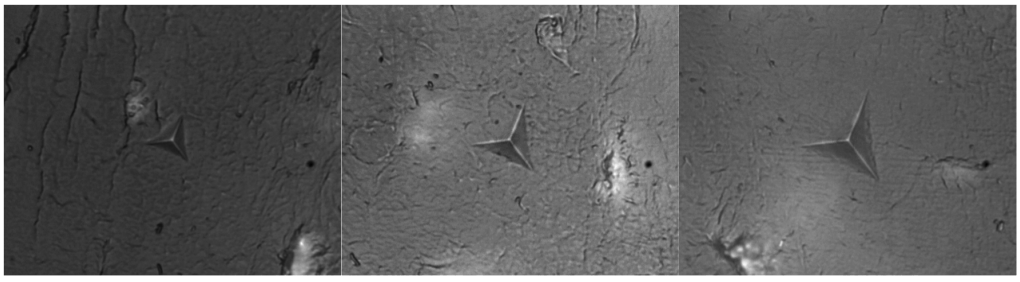

Figure 3.15: Optical microscopy (100x objective) images of residual impressions for indentation tests on bovine bone in dry conditions, performed at penetration depth of 1000 nm (left), 1500 nm (center), and 2000 nm (right).

Indentation modulus and hardness were extracted from the first unloading curve, using the Oliver and Pharr method (see Subsec. 2.1.3). Examples of

the analytical fits are shown in figure 3.16. Mean and standard deviation of E_{IT} and H_{IT} as a function of the penetration depth are shown in Figure 3.17 and 3.18 for dry and wet samples respectively. Moreover, the ratio between H_{IT} and E_{IT} has been calculated (Figure 3.19 and 3.20). A linear regression model is used to fit the data, and the equation of the straight line is written on each graphic.

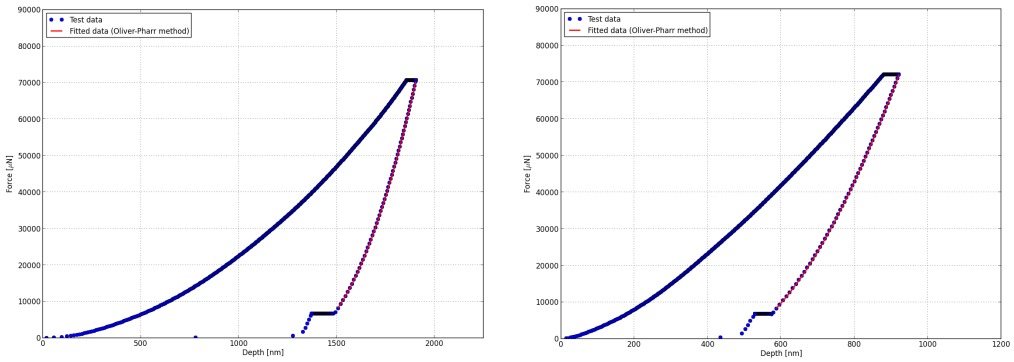

(a) Berkovich tip

(b) Spherical tip

Figure 3.16: Examples of P-h curves fitted for the unloading phases with the Oliver and Pharr method. Curves are taken from dry specimens indented with Berkovich (a) and spherical (b) tip and experimental set n°2.

Creep and backcreep were measured during step II and IV respectively. Means, standard deviations and linear regression fittings of these parameters are shown in Figure 3.21 and 3.22 for dry and wet samples respectively. The results from two way ANOVA tests are summarized in Table 3.5.

The ratio, W_{el}/W_{tot}, of elastic work (recovered during step III, IV and V) to the total work, is represented in Figure 3.23 and 3.24 as a function of the penetration depth.

Means and standard deviations of all the extracted values mentioned above are presented in Table 3.6.

3.2.3 DMA Mode

In this Section, results obtained with experimental set n°3 are presented. After experiments, the material sample surface was observed with help of OM. The dynamic mechanical analysis allows for a continuous acquisition of H_{IT} and E_{IT}, whose means and 95% confidence intervals are shown in Figure

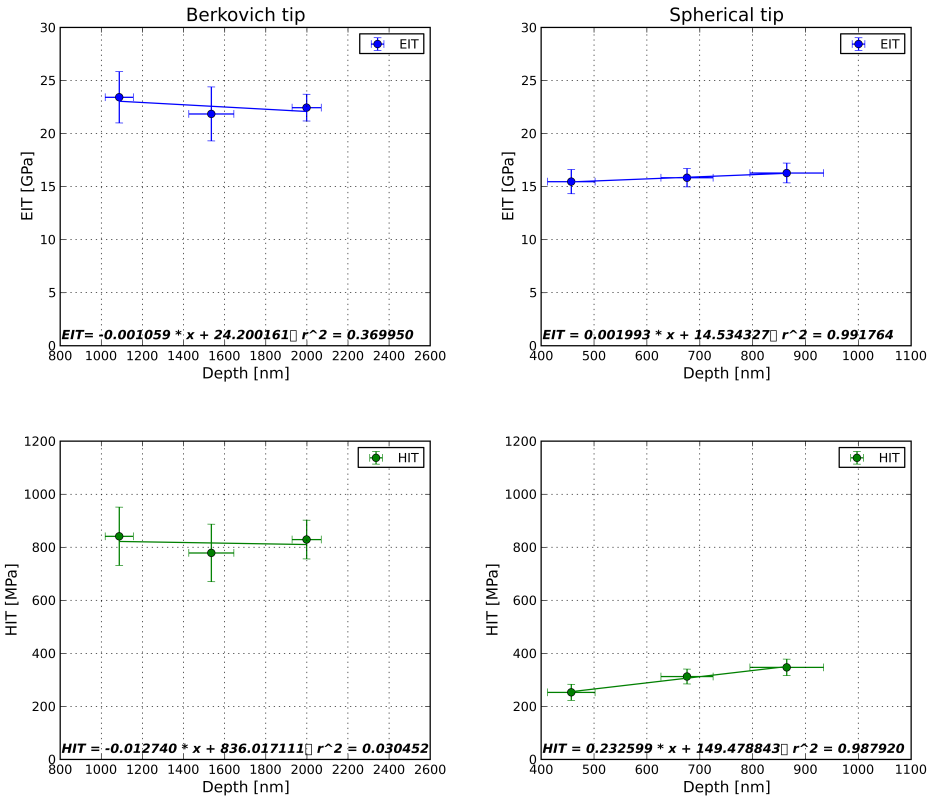

Figure 3.17: E_{IT} and H_{IT} (mean and standard deviation) of dry bovine bone samples calculated using a five-step loading history. The equation written below each graphic represents the linear regression line.

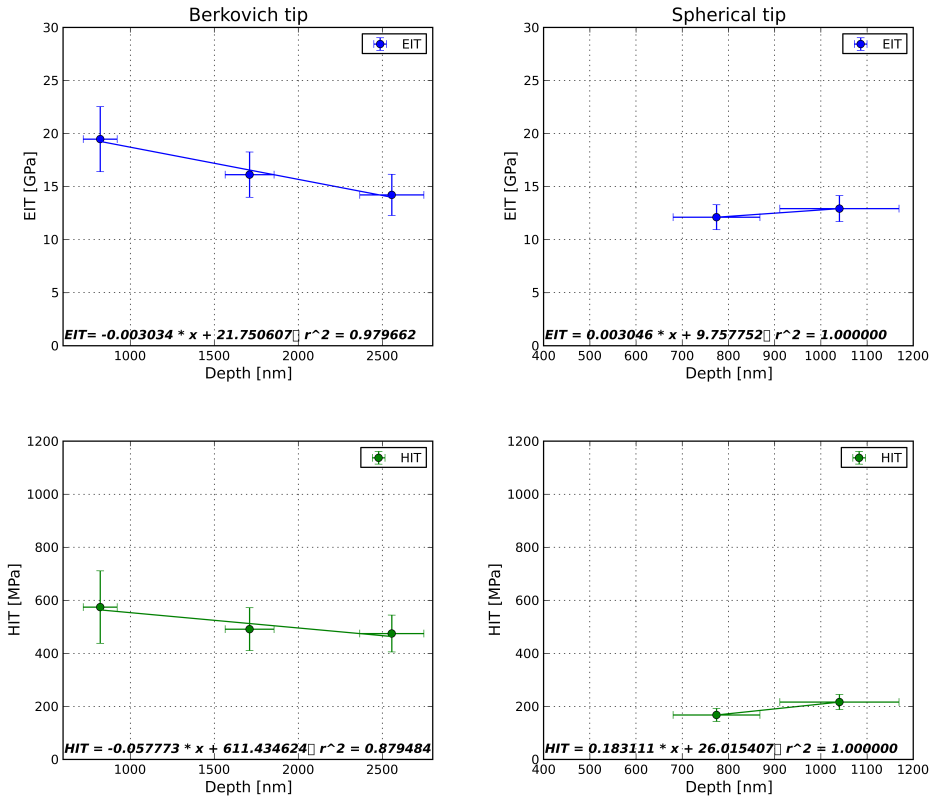

Figure 3.18: E_{IT} and H_{IT} (mean and standard deviation) of wet bovine bone samples calculated using a five-step loading history. The equation written below each graphic represents the linear regression line.

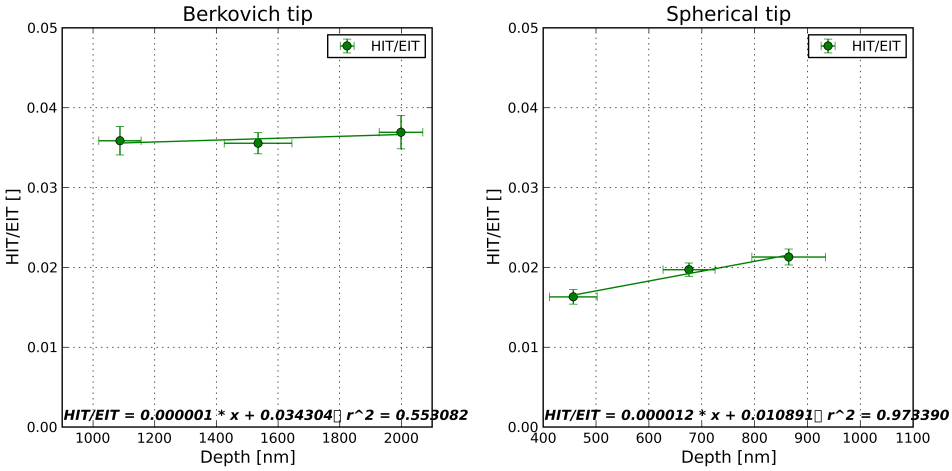

Figure 3.19: Ratio of H_{IT}/E_{IT} (mean and standard deviation) of dry bovine bone samples calculated using a trapezoidal loading history. The equation written below each graphic represents the linear regression line.

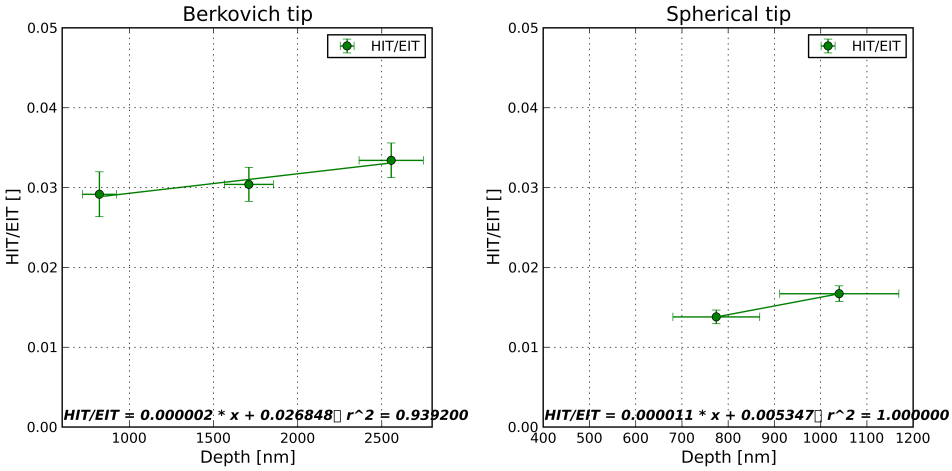

Figure 3.20: Ratio of H_{IT}/E_{IT} (mean and standard deviation) of wet bovine bone samples calculated using a trapezoidal loading history. The equation written below each graphic represents the linear regression line.

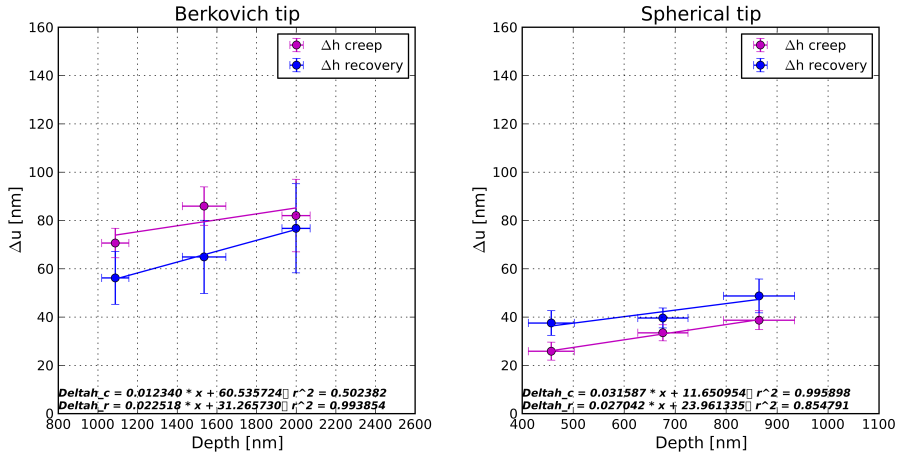

Figure 3.21: Creep and recovery (mean and standard deviation) of dry bovine bone samples. The equation written below each graphic represents the linear regression line.

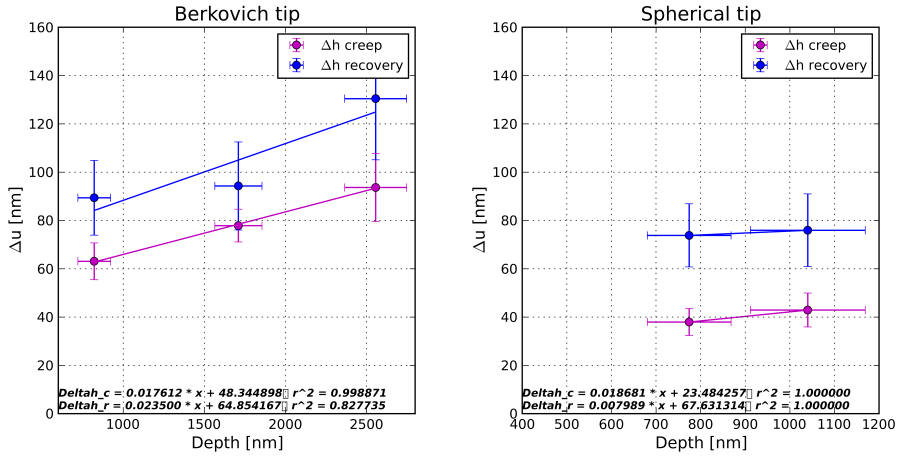

Figure 3.22: Creep and recovery (mean and standard deviation) of wet bovine bone samples. The equation written below each graphic represents the linear regression line.

Table 3.5: Significance level of the parameters investigated for creep and recovery results under both dry and wet conditions from experimental set n°2. Significance code: 0 '$***$', 0,001 '$**$', 0,01 '$*$', 0,05 '.', $>$ 0,1 ' '.

	p value (Berkovich)		p value (spherical)	
Factors for creep				
Penetration depth	$< 2e-16$	$***$	$< 2e-16$	$***$
Hydration conditions	0,42		$3{,}56e-7$	$***$
Penetration depth vs. hydration conditions	$1{,}97e-6$	$***$	0,313	
Factors for recovery				
Penetration depth	$< 2e-16$	$***$	$< 2e-16$	$***$
Hydration conditions	$< 2e-16$	$***$	$< 2e-16$	$***$
Penetration depth vs. hydration conditions	0,00272	$**$	0,23	

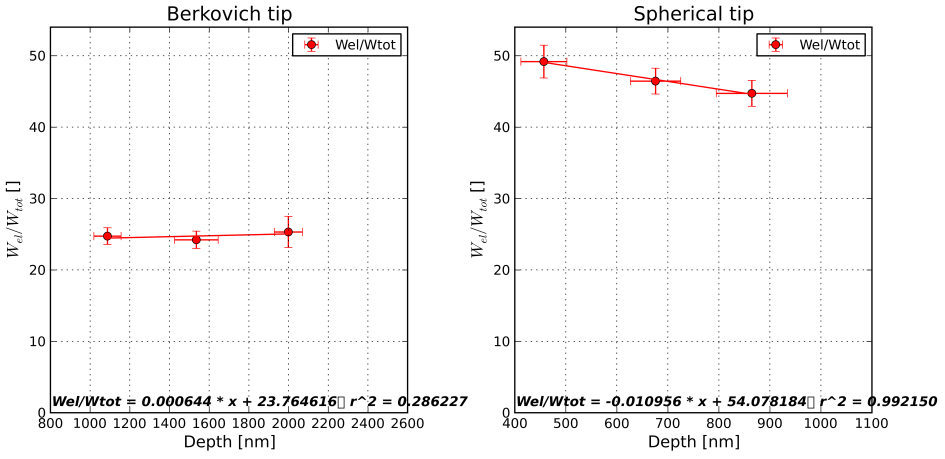

Figure 3.23: W_{el}/W_{tot} (mean and standard deviation) of dry bovine bone samples. The equation written below each graphic represents the linear regression line.

Table 3.6: Means and standard deviations (in brackets) of parameters calculated from experimental set n°2.

Tip	Depth [nm]	Dry/Wet	E_{IT} [GPa]	H_{IT} [MPa]	$W_{el}/W_{tot}\%$	Δh_{creep} [nm]	$\Delta h_{recovery}$ [nm]
B	1087,22	D	23,42	841,41	24,74	70,66	56,22
	(68.45)		(2,42)	(109,94)	(1,16)	(6,11)	(10,95)
	820,98	W	19,47	574,46	29,18	63,09	89,39
	(100,99)		(3,07)	(136,59)	(1,40)	(7,63)	(15,48)
	1535,17	D	21,85	778,63	24,22	85,94	64,90
	(109,78)		(2,54)	(108,54)	(1,22)	(7,95)	(15,15)
	1709,72	W	16,13	491,23	29,18	77,86	94,29
	(145,55)		(2,14)	(80,85)	(2,22)	(6,77)	(18,22)
	1998,83	D	22,44	829,14	25,32	82,02	76,73
	(70,90)		(1,26)	(73,03)	(2,18)	(15,03)	(18,46)
	2556,31	W	14,22	474,72	30,16	93,67	130,43
	(190,88)		(1,94)	(69,41)	(3,23)	(14,08)	(25,32)
S	456,93	D	15,46	252,96	49,18	25,86	37,53
	(45,05)		(1,14)	(30,44)	(2,30)	(3,72)	(5,11)
	NA	W	NA	NA	NA	NA	NA
	NA		(NA)	(NA)	(NA)	(NA)	(NA)
	675,88	D	15,84	312,74	46,44	33,48	39,62
	(49,28)		(0,87)	(28,00)	(1,81)	(3,31)	(4,13)
	774,22	W	12,12	167,78	44,28	37,95	73,82
	(93,98)		(1,17)	(24,40)	(2,84)	(5,58)	(13,06)
	864,52	D	16,28	347,31	44,73	38,70	48,75
	(69,70)		(0,94)	(31,00)	(1,81)	(3,92)	(7,01)
	1040,14	W	12,93	216,48	44,31	42,92	75,94
	(128,95)		(1,22)	(28,57)	(2,52)	(7,02)	(15,04)

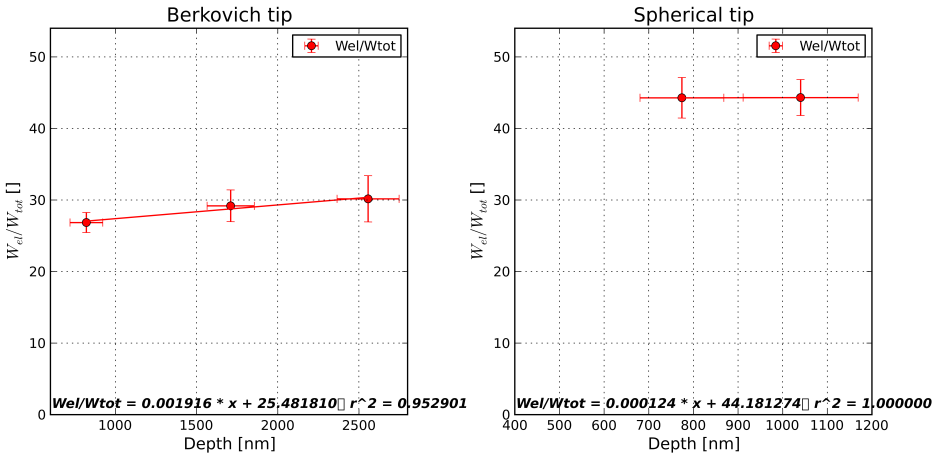

Figure 3.24: W_{el}/W_{tot} (mean and standard deviation) of wet bovine bone samples. The equation written below each graphic represents the linear regression line.

3.25 and 3.26 for dry and wet samples respectively. This method also allows plotting storage and loss modulus versus depth. The results for loss modulus are shown in Fig. (3.27) and (3.28) for the two hydration conditions.

3.2.4 Progressive Multi-Cycle

In this Section, results obtained with experimental set n°4 are presented. Examples of the resulted load-displacement curves for both Berkovich indenter and spherical indenter are shown in Figure 3.29.

After experiments, the material sample surface was observed with help of OM. Indentation modulus and hardness were extracted from the unloading segment of each cycle, using the Oliver and Pharr method (see Subsec. 2.1.3). Mean and standard deviation of E_{IT} and H_{IT} as a function of the penetration depth are shown in Figure 3.30 and 3.33 for dry and wet samples respectively. Creep and backcreep were measured in each cycle. Means and standard deviations of these parameters are shown in Figure 3.31 and 3.33 for dry and wet samples respectively. For each loading cycle the ratio, W_{el}/W_{tot}, to the total work of elastic work recovered during unloading and minimum-load holding period, is represented in Figure 3.32 and 3.33 as a function of the penetration depth.

Means and standard deviations of all the extracted values mentioned above are presented in Tables 3.7 and 3.8 for Berkovich and spherical tip respectively.

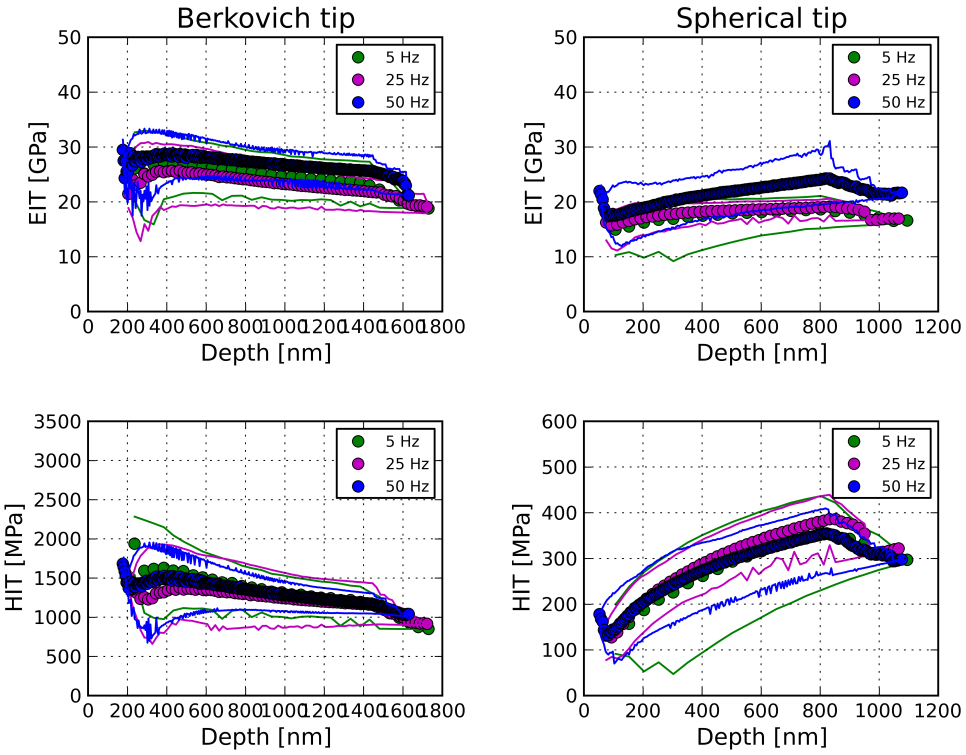

Figure 3.25: E_{IT} and H_{IT} of dry bovine bone samples calculated using a sinus mode loading history. Dotted lines represent means, while solid lines represent the 95% confidence intervals.

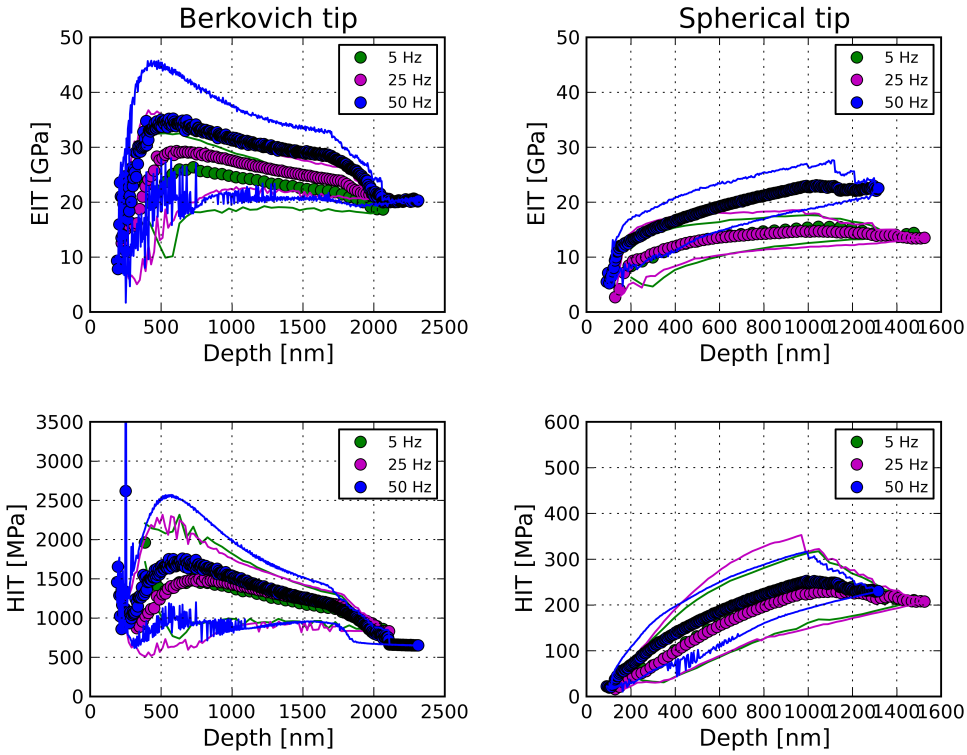

Figure 3.26: E_{IT} and H_{IT} of wet bovine bone samples calculated using a sinus mode loading history. Dotted lines represent means, while solid lines represent the 95% confidence intervals.

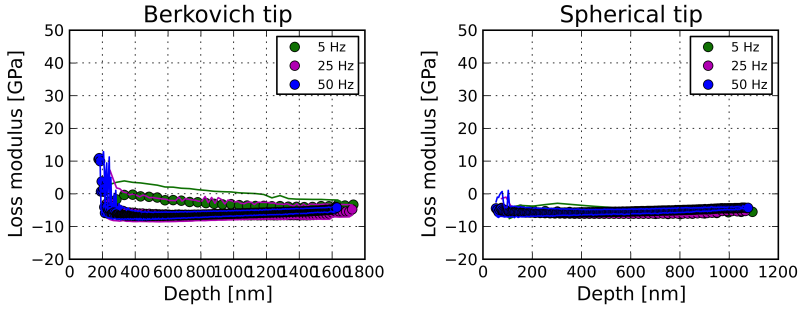

Figure 3.27: Variation of loss modulus E'' as function of the penetration depth in nanoindentation tests in dry conditions.

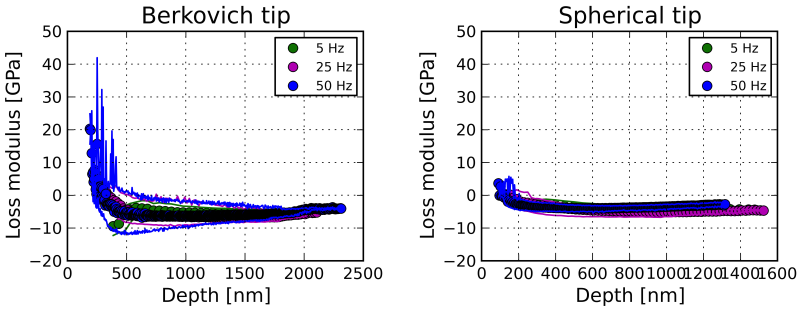

Figure 3.28: Variation of loss modulus E'' as function of the penetration depth in nanoindentation tests in wet conditions.

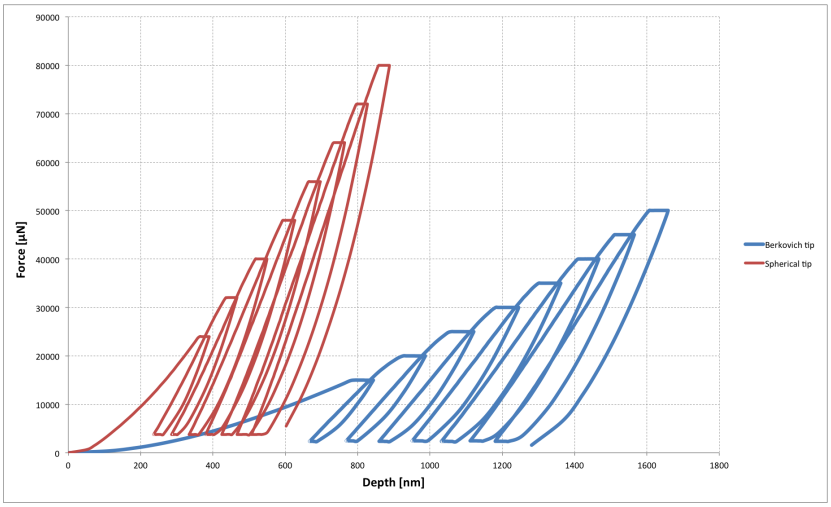

Figure 3.29: Example of P-h indentation curves for the Berkovich (blue) and spherical (red) tips in the experimental set n°4.

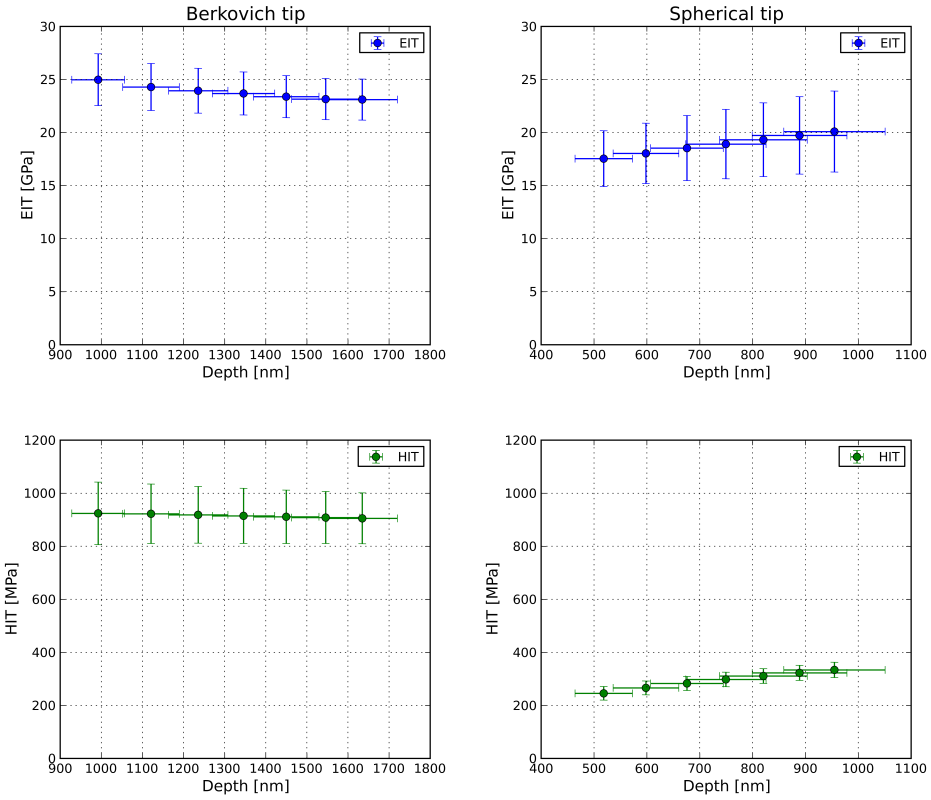

Figure 3.30: E_{IT} and H_{IT} (mean and standard deviation) of dry bovine bone samples calculated using a progressive multi-cycle loading history.

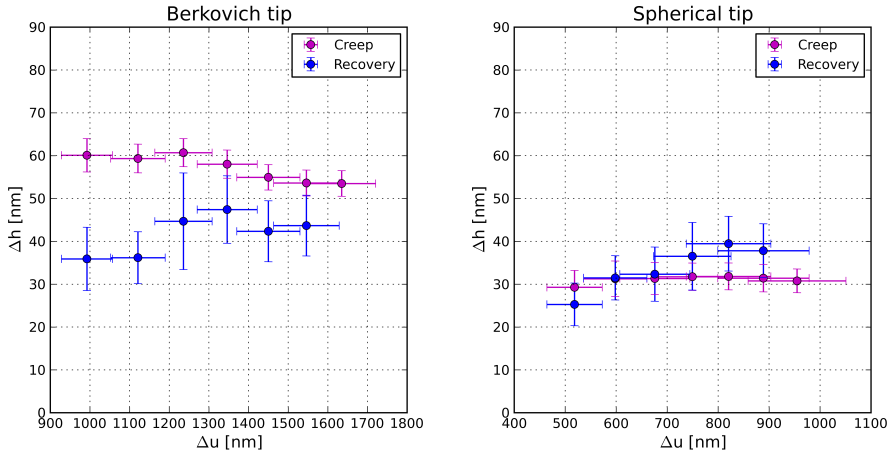

Figure 3.31: Creep and recovery (mean and standard deviation) of dry bovine bone samples.

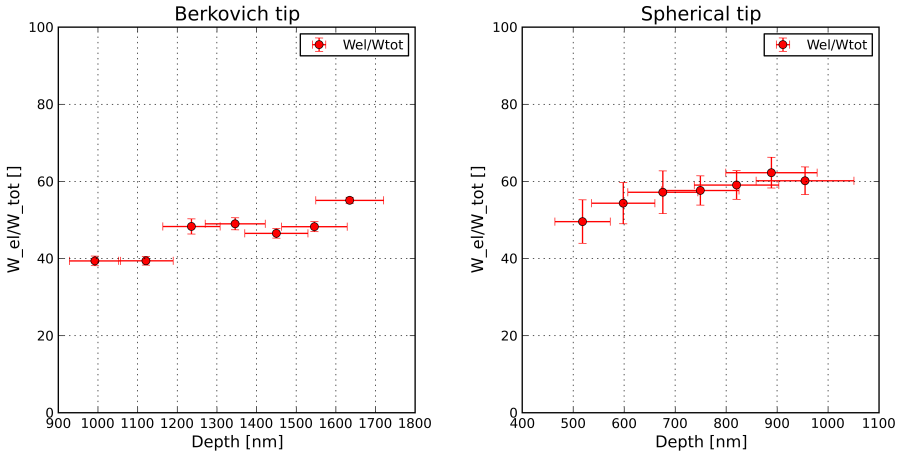

Figure 3.32: W_{el}/W_{tot} (mean and standard deviation) of dry bovine bone samples.

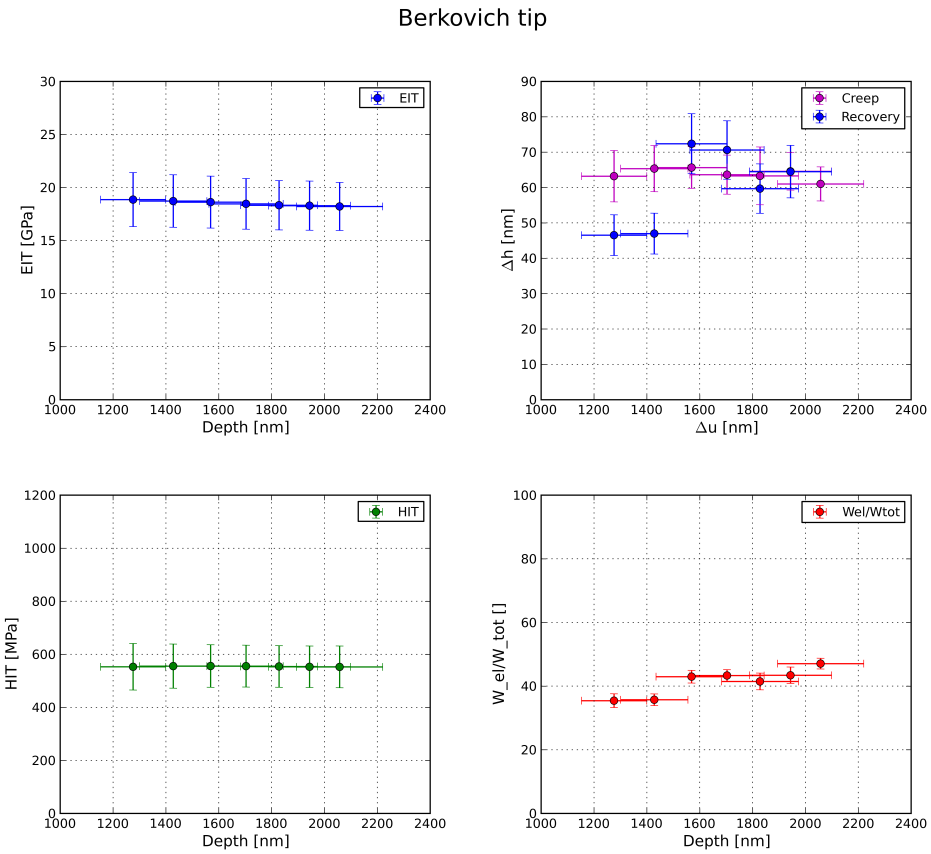

Figure 3.33: E_{IT}, H_{IT}, creep and recovery, and the ratio W_{el}/W_{tot} (mean and standard deviation) of wet bovine bone samples calculated using a progressive multi-cycle mode loading history.

Table 3.7: Means and standard deviations (in brackets) of parameters calculated from experimental set n°4 using a Berkovich indenter tip.

Tip	Value	Wet/Dry	1	2	3	4	5	6	7
B	Load [μN]		20000	25000	30000	35000	40000	45000	50000
	Depth [nm]	D	992,35 (64,37)	1120,86 (68,81)	1235,67 (72,20)	1345,97 (75,82)	1449,85 (79,59)	1545,77 (82,81)	1634,71 (85,62)
		W	1275,67 (123,51)	1427,73 (127,30)	1568,97 (134,39)	1703,13 (140,51)	1828,05 (145,58)	1943,41 (155,47)	2057,19 (163,05)
	E_{IT} [GPa]	D	24,98 (2,44)	24,29 (2,21)	23,94 (2,11)	23,68 (2,03)	23,38 (1,99)	23,15 (1,94)	23,11 (1,93)
		W	18,86 (2,55)	18,73 (2,47)	18,62 (2,45)	18,46 (2,39)	18,33 (2,32)	18,29 (2,31)	18,21 (2,26)
	H_{IT} [MPa]	D	924,02 (118,03)	922,38 (112,23)	918,44 (106,99)	914,54 (103,91)	911,08 (100,75)	908,29 (98,15)	905,27 (95,96)
		W	553,06 (87,69)	555,47 (83,36)	555,78 (80,18)	555,44 (78,88)	554,13 (78,42)	553,07 (78,39)	552,54 (78,74)
	$W_{el}/W_{tot}\%$ []	D	39,38 (1,25)	39,41 (1,12)	48,31 (1,98)	49,00 (1,55)	46,53 (1,25)	48,26 (1,30)	55,08 (0,79)
		W	35,43 (2,15)	35,74 (1,84)	42,97 (2,00)	43,34 (1,84)	41,48 (2,62)	43,42 (2,57)	47,07 (1,68)
	Δh_{creep} [nm]	D	60,10 (3,90)	59,33 (3,35)	60,70 (3,27)	58,01 (3,29)	54,95 (2,97)	53,63 (3,02)	53,50 (3,00)
		W	63,21 (7,26)	65,34 (6,54)	65,64 (5,89)	63,64 (5,54)	63,30 (8,16)	64,58 (5,31)	61,01 (4,82)
	$\Delta h_{recovery}$ [nm]	D	35,90 (7,39)	36,18 (6,05)	44,69 (11,29)	47,42 (7,87)	42,35 (7,11)	43,69 (7,09)	
		W	46,54 (5,76)	46,97 (5,76)	72,38 (8,50)	70,62 (8,26)	59,68 (6,99)	64,49 (7,42)	

Table 3.8: Means and standard deviations (in brackets) of parameters calculated from experimental set n°4 using a spherical indenter tip.

Tip	Value	Wet/Dry	1	2	3	4	5	6	7
S	Load [μN]		32000	40000	48000	56000	64000	72000	80000
	Depth [nm]	D	518,23 (54,31)	598,15 (62,11)	675,77 (68,74)	749,42 (75,89)	820,40 (82,94)	888,78 (89,64)	954,78 (95,94)
	E_{IT} [GPa]	D	17,54 (2,63)	18,03 (2,85)	18,53 (3,07)	18,91 (3,27)	19,32 (3,48)	19,73 (3,65)	20,09 (3,82)
	H_{IT} [MPa]	D	245,49 (25,60)	265,99 (26,02)	282,81 (26,48)	297,83 (27,33)	310,82 (27,82)	322,66 (28,36)	333,74 (28,74)
	$W_{el}/W_{tot}\%$ []	D	49,57 (5,64)	54,35 (5,34)	57,19 (5,54)	57,65 (3,80)	59,06 (3,72)	62,26 (3,99)	60,17 (3,57)
	Δh_{creep} [nm]	D	29,29 (3,94)	31,26 (4,15)	31,34 (3,71)	31,74 (3,19)	31,81 (3,14)	31,41 (3,21)	30,78 (2,78)
	$\Delta h_{recovery}$ [nm]	D	25,28 (4,98)	31,48 (5,16)	32,34 (6,33)	36,53 (7,90)	39,47 (6,39)	37,82 (6,29)	

CHAPTER 4

Discussion

Nanoindentation has become an increasingly popular technique for analyzing mechanical properties of bone at small length scales. A typical nanoindentation may penetrate shallowly into materials and thus may significantly be influenced by surface roughness due to specimen preparation and it may have a significant impact on the properties measured. Thus, in the present work, penetration depths lower than $\approx 500\,\text{nm}$ were not explored.

The penetration depths of 1000-2000 nm explored with the Berkovich tip correspond to a contact diameter of $\approx$ 6-11 µm, while the penetration depths of 500-1000 nm explored with the spherical tip correspond to a contact diameter of $\approx$ 14-20 µm. Thus, in the present study, the length scale probed is comparable with the size of one or more lamellae in a osteon (an average lamellar layer is between 3 and 7 µm), but the material properties reported at these specific penetration depths reflect the average material response from the initial point of contact down to the specific depth reported.

A strong point of this work is that smooth bone surfaces were achieved through a fast preparation procedure, which minimized dehydration and infiltration with PMMA. The final procedure for sample preparation was performed without using chemicals for cleaning and dehydration. In this way the mechanical properties of the microstructural features were kept as natural as possible. Usually, bone surface preparations involves polishing using glycol or aqueous solutions, but this repeated drying and wetting by the lubricant and cooling agents was found to introduce ultracracks in the bone surface. As nanoindentation operates at small length scale, those cracks potentially distort the measurements. This problem was avoid by smoothing the sample

surface at a wet state using an ultramiller system. Moreover, this system allows for a rather fast ($\approx 5 \pm 8$ minutes) smoothing, so that the dehydration is minimized. All bone samples used throughout the course of this research were embedded in an embedding medium mainly due to the need to have a big testing surface for the distance between the real tip and the reference in the UNNT. In the present study, highly viscous PMMA with rather short (≈ 30 min) curing time was employed, thus the bone was not reasonably infiltrated by the embedding medium and its mechanical properties were not influenced. PMMA infiltration is also prevented by the low porosity of the bovine cortical bone. Moreover in the present study both wet and dry samples were milled and the PMMA was completely removed from the bone surface, and care was also taken not to indent the specimens near Haversian canals and near the border between bone and PMMA. In fact, Zhao and coworkers [Zhao and Ovaert, 2010] found that errors in the computed mechanical properties may be introduced when indenting near the interface between two materials having different mechanical properties. In order to minimize the error, they suggested to maintain a separation distance from the interface of approximately 10 and 40 times the maximum indentation depth for the Berkovich and the spherical indenter respectively.

Some limitations must be considered in the interpretation of these results. Conventional nanoindentation testing is based on elastic contact mechanics and adapted for elastic-plastic contact. This approach has successfully been applied to a wide range of metallic and ceramic materials, but it doesn't account for time-dependent behavior such as creep. Strategies for viscoelastic materials have been recently explored and the most commonly used approach is to allow the material to creep while holding the maximum load constant. For viscoelastic materials, the effect of continued creep deformation during unloading is to increase the elastic recovery rate, the apparent depth of contact h_c, and hence the contact area A_c, which leads to overestimate the elastic modulus (see Eq. 2.7) [Bushby et al., 2004]. Moreover, during the nanoindentation tests, the samples were deformed beyond the elastic limit and were thus not only experiencing viscoelastic effects, but damage and viscoplastic behavior may have affected the measurements, especially in the earliest part of the holding period. During the hold period of nanoindentation, the force is held constant, while the stress is continually decreasing during the creep process and should minimize damage and plastic deformation [Shepherd et al., 2011]. Moreover, Isaksson et al. [Isaksson et al., 2010] employed semi-dynamic testing in their study and they observed that there was clearly a viscoelastic component that was consistent with the creep measurements, indicating that viscoplasticity in not the dominant factor in creep tests of bone. In the present study, two different indenter tip geometries were used:

the Berkovich indenter involves some plastic and damaging behavior in contrast to the spherical indenter, which produces smaller and smoother plastic imprints and is often used to attain (almost) purely elastic indentation.

The lack of a gold standard measurement is an important limitation of this study. Nanoindentation measurements of viscoelastic constant are consistent with the macroscopic measurements in polymers [Oyen, 2005]. In contrast, bone has a hierarchical structure and an agreement between macroscopic and nanoindentation results cannot be assumed.

This study has also several limitations as only the viscoelastic effects of the bone are studied, whereas plastic and poroelastic characteristics were not investigated. Other techniques yielding the information on bone samples composition and structure could be used in parallel to relate these informations to the parameters measured by nanoindentation. In this study average mechanical properties of different bone microstructures were reported. These properties depend on spatial variations in mineralization and variations in collagen/lamellar morphology [Feng et al., 2012]. Thus microstructural characterization of the indented regions would provide additional informations about bone's structure-property relations.

Water is an important contributor to the structure and mechanical behavior of bone. During dehydration, bone undergoes both structure and tissue-level changes which combine to alter the apparent properties. The primary strength of the present work was the direct comparison of moduli and viscoelastic parameters measured by nanoindentation in wet and dry conditions and with a Berkovich and a spherical indenter shape. In general, in hydrated samples, responses were found to be more variable than for dehydrated samples. It is well known that if a thin layer of liquid is present between contacting bodies, it contributes to their mutual attraction by its surface tension. This is also the case in nanoindentation. The tensile surface stress acts along the circumference of the liquid ring around the indenter-sample contact and attracts the indenter to the specimens. Moreover, when the liquid wets the indenter and the specimen, its shape is torroidal and the surface tension causes underpressure in it, which also attracts the indenter to the specimen [Mencík, 2012]. Hence, the contact load of the indenter approach in wet conditions was set five times greater than in dry conditions, but the contact detection was still a delicate point and it might be a source of error.

4.1 Indentation modulus and hardness

When the bovine axial specimens were examined using a trapezoidal load and a Berkovich tip, average indentation modulus was seen to decrease by $\approx 14\%$ as a function of increasing penetration depth in dry conditions, while it was seen to increase by $\approx 20\%$ in wet conditions. However, the strongest regression coefficient was seen in results from wet indentations ($r^2 = 0{,}95$), while the dry samples exhibit lower regression coefficient ($r^2 = 0{,}83$). The average E_{IT} at depths of 1000 nm, 1500 nm and 2000 nm, was found to be equal to $26{,}24 \pm 3.36$ GPa, $22{,}96 \pm 1.97$ GPa and $22{,}58 \pm 2.07$ GPa respectively in dry conditions, and $16{,}71 \pm 2.90$ GPa, $18{,}94 \pm 2.46$ GPa and $19{,}98 \pm 2.81$ GPa in wet conditions. The differences between dry and wet conditions lies around 36% at 1000 nm, and decrease to around 22% at 2000 nm.

Concerning the results of nanoindentation tests with a spherical tip, average indentation modulus was seen to slightly decrease in dry conditions and to increase in wet conditions. As in the previous case, the wet samples exhibited a strong regression coefficient ($r^2 = 0{,}92$), while a weak correlation was found testing dry samples ($r^2 = 0{,}55$). The average E_{IT} at depths of 500 nm, 750 nm and 1000 nm, was found to be equal to $13{,}53 \pm 1.32$ GPa, $13{,}73 \pm 0.99$ GPa and $12{,}86 \pm 1.23$ GPa respectively in dry conditions, and $9{,}46 \pm 1.86$ GPa, $12{,}57 \pm 1.76$ GPa and $13{,}62 \pm 1.35$ GPa in wet conditions. The difference between dry and wet conditions lies around 30% at 500 nm, while 1000 nm the indentation modulus in wet condition is $\approx 6\%$ higher than in dry conditions.

For the Berkovich tip, the standard deviations of the indentation modulus data tend to decrease as the test volume increases. This effect may in part be due to an averaging effect of the greater volume. In fact, as the volume increases, the differences in the degree of mineralization, and the presence of microstructural defects and canal spaces beneath the indentation site will be average over the larger volume. At the higher penetration depth, the standard deviation is comparable to the ones found with the spherical tip (which tested a larger volume even at lower penetration depth).

A two-way ANOVA demonstrated that penetration depth, hydration conditions and tip shape were highly significant factors ($p < 2e - 16$). Also the interaction between the tip shape and the hydration conditions was of high global significance ($p < 2e - 16$), and again the interaction between penetration depth and tip shape, and penetration depth and hydration conditions was significant ($p = 0{,}0015$ and $p = 0{,}0149$ respectively).

Due to the equality of the first part of nanoindentation protocols, the indentation modulus and hardness calculated in experimental set n°2 should be consistent with the values obtained from a trapezoidal loading history. Care

has to be taken when comparing the indentation depths, in particular indentations in wet conditions showed higher penetration depths than the ones in dry conditions. The only exception is the lower penetration depth explored with a Berkovich indenter, and this is probably due to a problem of the surface contact detection by the nanoindenter in wet conditions. In nanoindentations with a Berkovich tip, the average indentation modulus was seen to decrease by $\approx 4\%$ and $\approx 27\%$ as a function of the increasing depth in dry and wet conditions respectively. However, as expected from the previous results, a big difference was seen in regression coefficients between the two experimental conditions: r^2 was found to be equal to 0,37 and 0,98 in dry and wet conditions respectively. The average E_{IT} at depths of $\approx 1087\,\text{nm}$, $1535\,\text{nm}$ and $1999\,\text{nm}$, was found to be equal to $23{,}42 \pm 2.42\,\text{GPa}$, $21{,}85 \pm 2.54\,\text{GPa}$ and $22{,}44 \pm 1.26\,\text{GPa}$ respectively in dry conditions. Concerning the results in wet conditions at depths of $\approx 821\,\text{nm}$, $1710\,\text{nm}$ and $2556\,\text{nm}$, the average E_{IT} was found to be equal to $19{,}47 \pm 3.07\,\text{GPa}$, $16{,}13 \pm 2.14\,\text{GPa}$ and $15{,}22 \pm 1.94\,\text{GPa}$ respectively. In nanoindentations with a spherical tip, the average indentation modulus was seen to slightly increase as a function of the increasing depth in both dry and wet conditions. The average E_{IT} at depths of $\approx 457\,\text{nm}$, $676\,\text{nm}$ and $865\,\text{nm}$, was found to be equal to $15{,}46 \pm 1.14\,\text{GPa}$, $15{,}84 \pm 0.87\,\text{GPa}$ and $16{,}28 \pm 0.94\,\text{GPa}$ respectively in dry conditions. Concerning the results in wet conditions at depths of $\approx 774\,\text{nm}$ and $1040\,\text{nm}$, the average E_{IT} was found to be equal to $12{,}12 \pm 1.17\,\text{GPa}$ and $12{,}93 \pm 1.22\,\text{GPa}$ respectively.

In dry condition and with a Berkovich indenter tip, results from experimental set n°1 and 2 are comparable and E_{IT} is found to be approximately constant and equal to $\approx 22\,\text{GPa}$ at larger penetration depth. Using the same shape indenter tip in wet condition led to a big variability in the relationship between maximum load and penetration depth in experimental set n°1 and 2, and led to an opposite E_{IT} trend, but with the same value range of $\approx 15 - 20\,\text{GPa}$.

Concerning the results in dry conditions with a spherical tip, the average E_{IT} is equal to $\approx 13.37\,\text{GPa}$ for a trapezoidal load history, and $\approx 15.86\,\text{GPa}$ for the five-step protocol. In wet conditions, the E_{IT} value is approximately equal to $12 \div 13\,\text{GPa}$ for both protocols.

The fact that the wet measurements present lower force than their dry counter parts to reach the same penetration depth suggests a higher compliance for the former condition. Analougus observations can be made regarding the progressive-multycicle loading history and the DMA mode, where the wet measurements present $\approx 25 - 30\%$ higher penetration depths than the dry ones for the same indenter load. Water is known to plasticize collagen, to be a strong hydrogen bolding solvent and to prevent H-bonds forming between

peptides of adjacent triple helices leading to a more compliant structure. Free peptides bonds are created with dehydration, and new bonds, stronger than the H-bond with water, are formed between the peptide chains [Guidoni et al., 2010]. Moreover, the weak H-bonds could be broken by bone indentations and be restored upon removal the load as observed with the higher viscoelastic recovery of the wet condition. When drying, the increment of stronger peptide bonds should explain the higher force required to reach the same penetration depth as in wet condition. Additionally, aqueous solutions are known to demineralize the bone matrix by dissolution. For testing of whole samples, this has a little effect on measured properties, but nanoindentation is a surface sensitive technique and demineralization of the immediate surface layer would result in a reduced elastic modulus and more viscoelastic response [Bushby et al., 2004]. This effect may explain the increasing indentation modulus as function of the penetration depth for the spherical tip. However, this effect was also present when testing the dehydrated samples, implying that the softer surface may have resulted from mineral leaching during the specimen preparation. The spherical tip explored shallower depths than the Berkovich tip, and this may explain why results from the latter tip are not influenced by the reduced stiffness layer. These same trends were found by Bushby and colleagues [Bushby et al., 2004], who interpreted the experimental data using a "thin film model". The "thin film" was estimated to be of the order of several micrometers in depth and was attributed to several factors: the surface roughness, local demineralization and the mobility of of water near the free surface of the tissue. Furthermore, it is well know to exist an inverse relationship between water content and mineralization [Donnelly et al., 2006]. It is thus expected that the mechanical properties of less mineralized bone will undergo greater changes during dehydration, because a greater fraction of water is removed.

The present values for elastic modulus are within the range of those reported previously even if bone is heterogeneous in composition, structure, and mineral volume fraction, which leads to variations in material properties [Oyen, 2011]. Moreover, Zysset and colleagues [Zysset et al., 1999] noticed a marked variability of indentation modulus and hardness of cortical bone taken from selected sites within an individual. The modulus increase observed when drying is also qualitatively consistent with the nanoindentation results obtained in previous studies using a Berkovich indenter, whereas the results from using a spherical indenter could not be directly compared to those of other researchers due to the lack of published nanoindentation data on this material.

Previous research conducted by Wang et al. on zebrafish [Wang et al., 2002] and by Gleeson on human tibia [Gleeson, 2006] also found a trend of

decreasing stiffness as a function of increasing indentation depth. Similar studies have not been performed on bovine cortical bone tissue.

Guidoni et al. [Guidoni et al., 2010] found that the indentation modulus of bovine compact bone tested in dry conditions with a spherical tip is 40% higher than when measured immersed in buffer solution and they attributed this discrepancy to a marked change in the elastic properties of the organic matrix. In their work a penetration depth between around 300 nm and 500 nm, corresponding to a contact diameter of $\approx$ 11-14 µm.

Rho and Pharr [Rho and Pharr, 1999] observed that dehydration increased the elastic modulus by 15,4% (from $25{,}1 \pm 1{,}6$ to $27{,}5 \pm 1.2$ GPa) in interstitial lamellae in bovine femur cortical bone. The authors postulated that drying leads to contraction of the individual collagen fibrils and that the degree of contraction depends on the level of mineralization in the bone. Particularly, the mineral phase in hydrated bone provides a rigid scaffolding, and prevents the collagen fibrils from contracting and the bone from shrinking. Thus, small variations in the amount of mineral present in a section of bone can have a large influence on its mechanical properties. The greater degree of mineralization in interstitial bone can then explain the higher elastic modulus and hardness than those of osteons in the same region of the bone [Rho and Pharr, 1999].

A 26% elastic modulus increase in the interstitial bone and a 42% increase in the osteonal bone were observed after dehydrating porcine femoral cortical bone samples in the studies conducted by Feng and colleagues [Feng et al., 2012].

In general, drying increases the modulus of elasticity, while it reduces the fracture toughness [Isaksson et al., 2010]. Bembey et al. [Bembey et al., 2006a, Bembey et al., 2006b] showed that dehydration affects both the elastic and viscoelastic mechanical responses, in particular they noticed that the viscoelastic properties decreased with increasing dehydration. However, in order to closely control the experimental environment, most studies still use dehydrated bone tissue [Isaksson et al., 2010].

Carnelli et al. [Carnelli et al., 2011] found the bovine cortical bone indentation modulus equal to 21.65 GPa in axial direction, dry conditions and 300 nm deep with a Berkovich tip. In the same testing conditions, Carnelli [Carnelli, 2010] observed that the indentation modulus decreased from $26{,}19 \pm 0.49$ GPa at 50 nm deep to $19{,}72 \pm 0.54$ GPa at 300 nm deep, indicating a length scale effect of the mechanical properties bone tissue. The 24% decay in stiffness was attributed to the bone tissue deformation mechanisms at the microstructural level.

Isaksson and colleagues [Isaksson et al., 2010] in their study observed that the reduced modulus were dependent on the indentation depth and an

average value of $21{,}9 \pm 3.8$ GPa was found for bovine cortical bone. The same property was calculated separately in osteonal and interstitial bovine bone by Olesiak et al. [Olesiak et al., 2010], reporting values of $22{,}62 \pm 2.77$ GPa and $24{,}78 \pm 3.07$ GPa respectively.

The indentation modulus was seen to increase in the studies conducted by Paietta et al. [Paietta et al., 2011] over the large range of depths (from 100 to 2000 nm) tested with a spherical tip of 5 µm radius. However, the authors considered this stiffening as an artifact associated with greater plastic deformation and higher values of hardness.

Using a progressive multi-cycle protocol and a Berkovich tip, the average E_{IT} was seen to slightly decrease as a function of the penetration depth in both dry ($\approx -7{,}5\%$) and wet ($\approx -4{,}5\%$) conditions. In wet conditions the E_{IT} is equal to $18 \div 19$ GPa, and is $\approx 20\%$ lower than the value in dry conditions ($23 \div 24$ GPa). Concerning a spherical tip, an increase of $\approx 15\%$ from 18 to 20 GPa was observed in dry conditions. The results from the DMA mode reflect these same trends. Using a Berkovich tip, the E_{IT} curves seem to converge at higher penetration depth for different test frequencies. Moreover, at very low penetration depths the 95% CIs are wide and overlap, while a narrow width is observed at higher penetration depths. The high scatter in modulus at low contact depths (< 1000 nm) may suggest that roughness plays a major role in these variations. As expected, the CIs show a depth dependence because surface roughness changes its relative influence with increasing depth. On the contrary, using a spherical tip, the E_{IT} curve obtained with a frequency of 50 Hz diverges from the curves with lower frequencies, and at high penetration depths (> 1000 nm) the CIs do not overlap, then the difference between the values is significant at 95%.

Hardness and calcium content in bone are strongly related. Since a variations in mineralization produces variation in indentation modulus, there should be a relationship between this modulus and hardness. As expected, hardness values demonstrated trends comparable to indentation modulus in each test protocol, but in general with lower scatter. Since the hardness, unlike the modulus, is related to the displacement squared, squaring the fractional displacements uncertainties leads to smaller errors [Isaksson et al., 2010].Moreover, in homogeneous material, for perfectly sharp tip, the hardness is essentially independent of the indentation depth, while for spherical indenter the hardness is less at smaller indentation depths. In fact, at initial rise in hardness, in most cases and especially very hard materials, is entirely expected when, at very small scale of testing, the contact is elastic. The value of hardness calculated under these conditions is the mean contact pressure, which, for a given load, will be less than the hardness of the specimen material. Once we have a fully developed plastic zone, the hardness of the

sample should reach a plateau [Fischer-Cripps, 2011].

In experimental set n°1 for a Berkovich tip, the average hardness was seen to decrease by $\approx 11\%$ as a function of increasing penetration depth in dry conditions, while it was seen to increase by $\approx 75\%$ in wet conditions. In particular, the average H_{IT} reduce from $993{,}83 \pm 170.97$ MPa at 1000 nm depth to $822{,}04 \pm 106.73$ MPa at 2000 nm in dry conditions, while, considering the same penetration depths, the hardness rises from $382{,}33 \pm 121.68$ MPa to $670{,}68 \pm 162.03$ MPa in wet conditions. Thus, the difference between dry and wet conditions is approximately 62% at 1000 nm, and decrease to around 24% at 2000 nm. Concerning the results of nanoindentation tests with a spherical tip, the average hardness was seen to increase in both dry and wet conditions. The H_{IT} increase from $239{,}63 \pm 45.52$ MPa at 500 nm depth to $293{,}72 \pm 54.04$ MPa at 1000 nm in dry conditions, and from $87{,}80 \pm 40.45$ MPa to $224{,}41 \pm 29.49$ MPa in wet conditions. The different H_{IT} between the two conditions reduces from 63% to 24% increasing the indentation depth.

The strongest regression coefficients were seen in results from wet indentations ($r^2 = 0{,}99$ and 0,97 for Berkovich and spherical tip), while the dry samples exhibit lower regression coefficient ($r^2 = 0{,}67$ and 0,87).

As expected, a two-way ANOVA demonstrated that the hydration conditions was a highly significant factor ($p < 2e - 16$) for both the tip shapes. For results obtained with a Berkovich tip, the penetration depth was significant ($p = 0{,}0456$) and its interaction with the hydration conditions was highly significant ($p = 1{,}17e-5$). While for the spherical tip, the penetration depth was highly significant ($p = 1{,}04e - 15$) and its interaction with the hydration conditions was significant ($p = 0{,}0256$). The penetration depth was found to be more significant for the results from the spherical tip than from the Berkovich tip. As explained earlier, the indentation hardness is depth-dependent for a spherical tip, which shows important elastic deformations.

In experimental set n°2, care has to be taken to consider the different penetration depths explored in wet and dry conditions. For the Berkovich tip, the average hardness was seen to decrease of 2% and 17% in dry and wet conditions respectively. The average HIT reduce from $841{,}41 \pm 109.94$ MPa at ≈ 1000 nm depth to $829{,}14 \pm 73.03$ MPa at ≈ 2000 nm in dry conditions. Concerning the result in wet conditions at depth of ≈ 820 nm and ≈ 2550 nm, the average HIT was found to be equal to $574{,}46 \pm 136.59$ MPa and $474{,}72 \pm 69.41$ MPa. For the spherical tip, the average indentation modulus was seen to increase in both dry and wet conditions. In dry conditions, the HIT at approximately 450 and 860 nm is equal to $252{,}96 \pm 30.44$ MPa and $347{,}31 \pm 31.00$ MPa respectively. While in wet conditions, the H_{IT} at approximately 770 and 1040 nm is equal to $167{,}78 \pm 24.40$ MPa and $216{,}48 \pm 28.57$ MPa respectively.

Concerning the results obtained with a Berkovich tip, the hardness values are comparable to those reported previously. In particular, Rho and Pharr [Rho and Pharr, 1999] found that hardness increased by 18% (from 578 ± 52 MPa to 680 ± 102 MPa) after drying osteons, and by 12% (from 730 ± 48 MPa to 818 ± 49 MPa) after drying interstitial lamellae in bovine bone. While in the studies conducted by Isaksson and coworkers [Isaksson et al., 2010], the measured hardness was 790 ± 190 MPa in dry cortical bovine bone. On the contrary, there is a lack of published hardness data obtained with a spherical indenter. Hengsberger et al. [Hengsberger et al., 2002] found that hardness in human bone ranged between 480 ± 100 and 1250 ± 260 MPa for thin and thick lamellae respectively in dry conditions and between 290 ± 130 and 950 ± 440 MPa in wet conditions. Thus, the hardness increased by 65% and 32% after drying. Zysset and coworkers [Zysset et al., 1999] noticed that hardness in dry human bone increased by $30 - 40\%$ as compared to fresh bone. Moreover, in their studies an increase of hardness followed the progression of bone mineralization.

In experimental set n°3 and 4, the hardness values are within the range of those found in the first two test protocols. Concerning a progressive multi-cycle loading history and a Berkovich tip, the average H_{IT} slightly decreases from 924 MPa to 905 MPa in dry conditions, while it is approximately constant and equal to 553 MPa in wet conditions. The three hardness curves obtained with the DMA mode seem to converge to these same results for each hydration condition. As expected, the 95% CIs width decreases at higher penetration depths. For a spherical tip and dry conditions, the hardness increase from 245 to 322 MPa in experimental set n°3. In DMA mode, the curves converge approximately to this value and it is interesting to note that the CIs are very narrow even at low penetration depths.

The H_{IT}/E_{IT} ratio is a quantitative measure of the relationship between a material's plastic and elastic deformation behavior [Gleeson, 2006]. In both experimental set n°1 and 2, this ratio was seen to increase as function of the penetration depth, exhibiting greater permanent deformation at higher contact depths. The only exception was for the trapezoidal loading history in dry condition and with a Berkovich tip, but the corresponding regression coefficient was very weak ($r^2 = 0{,}25$) compared with the others ($r^2 > 0{,}90$). As expected, the ratios H_{IT}/E_{IT} obtained with the Berkovich tip ($\approx 2 - 4\%$) were higher than the ones obtained with the spherical tip ($\approx 0{,}5 - 2{,}5\%$), which produces smaller plastic deformation than the former one. Moreover, the H_{IT}/E_{IT} ratios in dry condition were greater than the ones in wet condition, and this is consistent with the higher viscoelastic recovery observed in the latter condition.

4.2 Viscoelastic solution

Bone is well known to be a hierarchical composite, then the viscoelastic properties may different between microstructural and macroscopic levels, with the overall behavior depending on their interactions. Investigation of viscoelasticity at microstructural level can be done with nanoindentation. By considering the creep response at constant load, it is possible to explore the viscoelastic behavior within the bone tissue. In particular, the depth vs. time data can be fit to theoretical model based on combination of elastic and viscous element in order to determine parameters that describe the viscoelastic behavior [Fischer-Cripps, 2004]. However, the holding time may affect the curve fit to the viscoelastic model. The instantaneous elastic modulus E_1 is calculated from the indentation modulus EIT, thus fast unloading is essential in determining E_1 from initial unloading slope. In fact, the viscoelastic models used in the present work take the initial unloading process to be elastic, and don't account for any plastic deformation that affects the contact area during unloading. The delayed elastic deformation is described by E_2 and η, these parameters are calculated from fitting the displacement vs. time curves with the viscoelastic analytical model described in Section 2.2. For the Berkovich tip, E_1 and E_2 were significantly influenced by the hydration state ($p < 2e-16$), but not by the penetration depth ($p = 0{,}92$ and $0{,}25$ respectively). Whereas the two factors were highly significant for the viscosity η ($p = 1{,}05e-5$ and $5{,}89e-10$). E_1 was found to be higher than E_2 at each penetration depth. The three parameters E_1, E_2 and η calculated in dry conditions were greater than the corresponding values calculated in wet conditions, but the discrepancy between the two values decreased while increasing the penetration depth. In particular, the discrepancy in E_1 fell from 58 to 13%, in E_2 from 191 to 23%, and in η from 707 to 47%. η increased while increasing the penetration depth in both the hydration states. For the spherical tip, E_2 and η were significantly influenced by the hydration state ($p < 2e-16$) and by the penetration depth ($p = 5{,}35e-5$ and $p < 2e-16$ respectively). The hydration condition was a highly significant factor also for E_1, but the penetration depth was not. The three parameters E_1, E_2 and η calculated in dry conditions were greater than the corresponding values calculated in wet conditions, but the discrepancy between the two values decreased while increasing the penetration depth. E_2 decreased in dry conditions and increased in wet conditions, so that the the difference between the two states fell from 327% to 62%. The viscosity increased in both conditions, but the dry augmentation was lower than the wet one, hence the difference decreased. E_1 was found to be greater than E_2 at each penetration depth in wet conditions, while it was the opposite in dry conditions.

The moduli E_1 and E_2 obtained in dry conditions from both tips are much lower than the ones obtained in wet state, and this is reasonable since bone has more significant time-dependent behavior when immersed in a fluid. However the percentage difference was higher for E_2, thus the delayed creep compliance was greater influenced by the hydration condition. Concerning the results for viscosity, η was significantly lower in wet conditions, which means that the bone creeps more quickly. However, in both hydration conditions η increased while increasing the penetration depth, suggesting the creep rate slackened. At small indentation depth and wet conditions, η shows very small values, thus it seems that the model fit gives a mostly elastic curve, which is a power curve with exponent 2 for the Berkovich tip and 1,5 for the spherical one.

For both the indenter shape, the difference between the parameters in wet and dry conditions are smoothed while exploring higher penetration depths. These results could be explained by the fact that the Vandamme-Ulm and Cheng models assume that the deformations are purely viscoelastic, which is approximately true for spherical indentation at low loads. For spherical indenter at higher loads or for Berkovich indenter, the loading part of the curve contains permanent deformation when indenting bone. However, the spherical indentations are less effected by the lumping of elastic and plastic deformation. Moreover, one big limitation of the standard linear solid model is the presence of a single damping coefficient and a single retardation time, whereas real viscoelastic materials tend to have a relatively broad retardation spectrum [Kruijer et al., 2006]. Visco-elastic-plastic constitutive models should be used to fit the viscoelastic parameters to the full nanoindentation curves.

An alternative method to study viscoelasticity of bone tissue is the DMA [Lakes and Katz, 1979a]. The loss tangent, $\tan\delta$, measured by DMA was found to depend on loading frequency in both macroscopic and nanoindentation testing [Wu et al., 2011, Isaksson et al., 2010] Garner et al. [Garner et al., 2000] found that wet bone exhibits greater viscoelastic damping than dry bone over a broad range of frequency based on DMA analysis. Macroscopic viscoelasticity at low frequency has been attributed to fluid motion through the pore space and at interfaces between microstructural components, which may not be captured during nanoindentation [Lakes and Katz, 1979a, Garner et al., 2000]. Due to the independence of macroscale and microscale viscoelasticity, care should be taken to use measures at the scale of interest when assessing the effects of viscoelasticity on bone mechanics.

The loss modulus E'' represents the capacity of the material to dissipate energy, i.e. the viscous portion, while the loss tangent, $\tan\delta$, is often used as a measurement of damping in a linear viscoelastic material [Isaksson et al.,

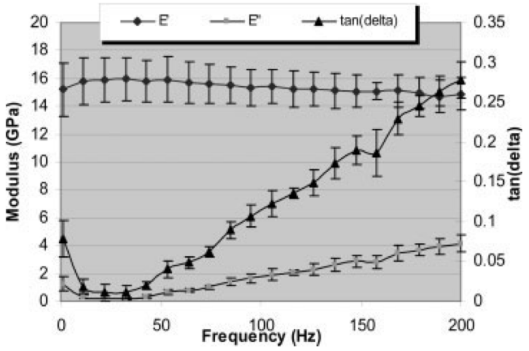

Figure 4.1: Variation of storage modulus, loss modulus, and loss factor with the frequency of the dynamic load for bovine plexiform bone [Lewis and Nyman, 2008].

2010]. The results obtained from Lewis and Nyman [Lewis and Nyman, 2008] using plexiform bone specimens are presented in Figure 4.1.

Using the sinus mode in the UNHT, frequencies lower than 5 Hz and higher than 50 Hz could not be explored. As already explained, the method allows for a continuous acquisition of hardness, elastic modulus, storage and loss modulus data as a function of indentation depth. Looking at Figure 4.1, very low E'' values should be expected at the tested frequencies. Unfortunately, the nanoindenter software provided negative loss moduli, which have no physical meaning. Except for a few positive values at very low penetration depths, the loss modulus was always negative and no value variations were found in changing the penetration depth, the indenter tip and the frequency. This abnormal phenomenon could be explained by the presence of an error inside the model implemented in the software.

4.3 W_{el}/W_{tot}

The ratio W_{el}/W_{tot} is a measure of the reversible elastic contribution to the total work. In experimental set n°1, the ratio is included between 44 and 50% for the spherical indenter tip, and between 25 and 29% for the Berkovich tip. As expected, more energy is dissipated in the indentation with Berkovich indenter shape. For the spherical tip, significant differences were seen in increasing the penetration depth ($p = 4,86e-8$), in particular the ratio decreased by 10 and 6% in dry and wet indentations respectively. In fact, it is well known that at the higher contact depths the spherical indents exhibit greater plastic deformation than at low penetration depths,

which remain relatively elastic. On the contrary, no significant difference were seen in changing the hydration condition ($p = 0{,}22$), which means that there was no higher viscoelastic recovery in wet conditions. On the contrary, for the Berkovich tip, the penetration depth was found not to be significant (0,85), while the hydration condition was highly significant ($2,58e-9$). In particular, the mean ratio W_{el}/W_{tot} in wet conditions (27,6%) was found to be 10% higher than in dry conditions (25,2) and this can be explained by an higher viscoelastic recovery. Concerning the results from experimental set n°2, they are approximately the same than in experimental set n°1, even if the protocol provided a 30 s holding phase at 10% of the maximum load. The only noticeable difference is the increased gap (now 20%) between wet and dry indentation with a Berkovich indenter, which can also be explained by an higher viscoelastic contribute during the holding phase at lower load. As explained in section 4.1, a Berkovich indenter contributes to wedging open and breaking the weak H-bonds between peptides. The bonds are restored after removing the load and a viscoelastic recovery is observed. On the contrary, the spherical tip is blunt and breaks a lower number of H-bonds, this may explain why no viscoelastic recovery is observed in wet conditions. Moreover, since the elastic work is calculated as the area below the unloading part of the P-h curve, the small contribution of the recovery during the second holding phase is due to the low load.

Applying a progressive multi-cycle loading history yields to different values and trends. Care has to be taken in comparing the results from the first and the last cycle to the other ones. In particular, the loading part of the first cycle starts from 0 µN, thus a greater plastic work is expected and, accordingly, a lower ratio W_{el}/W_{tot}. The last cycle doesn't provide an holding period during the unloading phase, but the load goes down to zero. For a Berkovich indenter, the ratio W_{el}/W_{tot} ranges from 39 to 55% in dry conditions, and from 35 to 47% in wet conditions. In both cases the trends of the work ratio reflects the one of the recovery distance, while the creep distance shows a small variability and doesn't follow the same trend. Hence, the W_{el}/W_{tot} changes are attributed to changes in viscoelastic recovery, which is more prominent during the first few cycles due to the little difference between the maximum and the minimum load. A considerable W_{el}/W_{tot} ratio increasing (more than 20%) is observed between the the second and the third cycle, which means a significantly reduction of the energy dissipated by the viscous damage mechanism occurring in the bone tissue. In wet conditions the W_{el}/W_{tot} ratio is $\approx 11\%$ lower than in dry conditions, and this difference cannot be explained by considering the creep and recovery distances. In fact, recovery and creep are higher in the former state than in the latter one of $30 \div 50\%$ and of $5 \div 20\%$ respectively. For a spherical indenter, the W_{el}/W_{tot}

ratio ranges from 49 to 62% in dry conditions, which, as expected, is higher than for the Berkovich tip. Moreover, a significant increasing trend can be revealed. A considerable ratio increasing (10%) is observed between the first and the second cycle, which reflects a high increase of the recovery distance. The creep distance is approximately constant, while the recovery distance increases and exceeds the corresponding creep value in the second cycle. Fan and colleague [Fan and Rho, 2003] noticed that the effects of time-dependent plasticity can be diminished by multiple loading,Äìunloading cycles, but the cycles of the protocol employed in the present study have an increasing maximum load, thus a higher plastic contribute is expected.

4.4 Creep and recovery

Creep and recovery are forms of time-dependent viscoelastic deformation. In experimental set n°2, the penetration depth was found to be an highly significant factor for creep and recovery, in particular a direct relationship between creep/recovery and penetration depth has been recognized. Also the hydration condition was recognized to have a high significance, except for the creep values obtained in dry condition with a Berkovich indenter. The interaction between indentation depth and hydration state was of high significance for the Berkovich tip, but it was not for the spherical one. For a Berkovich tip, in dry conditions the creep distance increased by 16% from 70 to 82 nm, while the recovery distance increased by 36% from 56 to 77 nm. In wet conditions, the creep distance increase by 48% from 63 to 94 nm and the recovery distance by 46% from 89 to 130 nm. However, care has to be taken in comparing these results to the ones in dry conditions due to the wide difference in the indentation depths explored. It is interesting to notice that in dry conditions the recovery distance was lower than the corresponding creep distance at each penetration depth, while in wet conditions it was the opposite. This result is consistent with the greater viscoelastic recovery that is expected in wet condition and that explained also the lower dissipated energy (see Section 4.3). Concerning the results for the spherical tip, in dry conditions the creep distance increased by 50% from 26 to 39 nm, while the recovery distance increased by 30% from 38 to 49 nm. In wet conditions, the creep distance was slightly higher than the corresponding value in dry conditions, while the recovery distance was definitely higher and equal to 74 ÷ 76 nm. The same considerations can be made as in the previous case, even if the recovery distance is higher than the creep one also in dry conditions, but the gap reduces increasing the penetration depth. In fact, a greater plastic contribute is contemplated at higher indentation depth.

In experimental set n°3, it has already been pointed out that the recovery distance and the W_{el}/W_{tot} ratio have the same trend as function of the penetration depth. For a Berkovich tip in both hydration conditions, the creep and the recovery distances seem to increase during the first few cycle and to decrease during the last ones. In dry conditions, the highest creep and recovery values were found in cycle n°3 and 4 respectively, and the recovery distance was lower than the corresponding creep distance at each cycle. In wet conditions, the two parameters were seen to be maximum in cycle n°3, and the recovery distance was higher than the creep distance in cycle n°3 and 4. The recovery distance was found to be between -40% (in the first cycle) and -12% (in the fourth cycle) than the creep distance in dry conditions, and between -26% (in the first cycle) and $+24\%$ (in the third cycle) in wet conditions. For the spherical tip, the same trends as for the Berkovich tip can be identified, but the higher recovery and creep distances were seen in the fifth cycle. Moreover, starting from the second cycle the recovery distance is higher than the corresponding creep distance in dry conditions. The creep distance had a lower variation, the values ranged from 29 to 32 nm. The recovery distance ranged from 25 to 39 nm, and these values correspond to -14% (in the first cycle) and $+24\%$ (in the fifth cycle) of the creep values. Using a spherical tip the plastic effect is significantly smaller than using a Berkovich tip. As already observed discussing the W_{el}/W_{tot} ratio, the plasticity can be decreased by multiple loading-unloading cycles.

Conclusions

Nanoindentation provides a means to investigate the viscoelastic properties of dry and wet bone at a small scale. However, because of the heterogeneous nature of this tissue at small scales, the testing protocol can affect the measured quantities [Isaksson et al., 2010]. Cortical bone has a very intricate structure and factors such as anatomy locations, age, gender and different microstructures, might affect nanoindentation measurements. However, how these factors influence the viscoelasticity of bone has not been explored systematically. A simple and relatively fast procedure has been developed for bone sample preparation, which doesn't involves dehydration and chemicals utilization. In this way the mechanical properties of the microstructural features are kept as natural as possible.

In the present study, the viscoelasticity of plexiform bovine bone has been investigated in dry and wet conditions and with two different indenter shapes. The spherical tip is well known to minimize plastic deformations, in fact it exhibited a greater viscoelastic behavior than the Berkovich tip, which is "sharp" and causes permanent deformations. However, the spherical tip exhibited not negligible plastic deformation at high contact depth. For the Berkovich tip, percentage difference between the results in dry and wet conditions was equal to $\approx 36\%$ at low penetration depth and it fell to $\approx 20\%$ while increasing the depth. For the spherical indenter, the percentage difference showed the same trend as in the previous case. At low penetration depth E_{IT} of the wet bone was $\approx 30\%$ lower than the dry conditions, but it was $\approx 6\%$ higher at 1000 nm depth. Hardness values demonstrated trends comparable to indentation modulus in each test protocol. The indentation modulus and hardness in dry conditions was significantly greater than in dry conditions, and this may be explained by the replacement of the weak hydrogen

bonds with stronger inter-peptide bonds during dehydration. Moreover, the fact that the wet measurements presented lower force than their dry counter parts to reach the same penetration depth suggested a higher compliance for the former condition. The degree of mineralization is believed to be another important factor. In liquid environment, mineral may be lost from the near-surface region yielding to a reduced elastic modulus and a more viscoelastic response from this region. The E_{IT}/H_{IT} ratio is a quantitative measure of the relationship between a material's plastic and elastic deformation behavior. This ratio was higher in dry state than in wet conditions, and this means the the wet bone was more affected by viscoelastic recovery.

Concerning the results for the viscoelastic analytical solutions, the hydration condition was the highly significant factor for all the parameters calculated. The elastic moduli and the viscosity were found to be higher in dry conditions, and the instantaneous elastic modulus was greater than the corresponding delayed elastic modulus. These results reflected a more significant time-dependent behavior of wet bone. However, all the differences reduced while increasing the penetration depth, suggesting a gain of plastic effects. In particular, the viscosity in wet conditions was found to be very small, thus the material response was mainly elastic. The creep behavior was investigated using a standard linear solid rheological model applied at holding phase. However, the viscoelastic behavior of bone could not be adequately described by a simple linear model [Currey, 1964, Lakes and Katz, 1979a]. Thus, the Burgers model or the generalized Maxwell model, which include two independent viscous parameters should be employed in future works.

The ratio W_{el}/W_{tot} is a measure of the reversible elastic contribution to the total work. This ratio ranged from 44 to 50% for the spherical indenter tip, and from 25 to 29% for the Berkovich tip. The results for the spherical tip was significantly influenced by the penetration depth, but not by the hydration condition. At higher contact depth, the spherical indent exhibited more plastic deformation. On the contrary, the hydration condition was found to be an highly significant factor for the Berkovich tip, and wet bone exhibited a ratio W_{el}/W_{tot} 10% higher than in dry conditions.

Creep and recovery are forms of time-dependent viscoelastic deformation. These factor were seen to be highly influenced by both the penetration depth and the hydration state. In dry conditions the recovery distance was lower than the corresponding creep distance at each indentation depth, while it was the opposite in wet conditions. This results agree with the greater viscoelastic behavior in wet bone again.

Microstructural characterization of the indented regions would provide additional important informations about bone's structure-property relation-

ship.

A complete understanding of the viscous, elastic, and plastic material properties of bone is important in understanding the complex heterogeneous properties of bone and many clinical problems, such as wound healing, tissue engineering, and disease processes. It is suggested that nanoindentation in physiological conditions gives a better estimate of the mechanical properties of the microstructural components of bone in vivo rather than nanoindentation under conventional conditions.

Bibliography

[Lys, 1949] (1949). *Indentation Hardness Testing.* Reinhold Publishing Corp., New York.

[Ascenzi and Bonucci, 1967] Ascenzi, A. and Bonucci, E. (1967). The tensile properties of single osteons. *Anat. Rec.*, 158:375–386.

[Ascenzi et al., 1978] Ascenzi, A., Bonucci, E., Ripamonti, A., and Rovery, N. (1978). X-ray diffraction and electron microscope of osteons during calcification. *Calcif. Tissue Int.*, 25:133–143.

[Auerbach, 1893] Auerbach, F. (1893). *Smithsonian report for 1891.* Government printing office, Washington.

[Bailey et al., 2002] Bailey, A. J., Sims, T. J., Ebbesen, E. N., Mansell, J. P., Thomsen, J. S., and Mosekilde, L. (2002). Age-related changes in the biochemical properties of human cancellous bone collagen: relationship to bone strength. *Calcif. Tissue Int.*, 65:203–210.

[Bayraktar et al., 2004] Bayraktar, H. H., Morgan, E. F., Niebur, G. L., Morris, G. E., Wong, E. K., and Keaveny, T. M. (2004). Comparison of the elastic and yield properties of human femoral trabecular and cortical bone tissue. *Journal of Biomechanics*, 37(1):27–35.

[Bembey et al., 2006a] Bembey, A. K., Bushby, A. J., Boyde, A., Ferguson, V. L., and Oyen, M. L. (2006a). Hydration effects on the micro-mechanical properties of bone. *Journal of Materials Research*, 21:1962–1968.

[Bembey et al., 2006b] Bembey, A. K., Oyen, M. L., Bushby, A. J., and Boyde, A. (2006b). Viscoelastic properties of bone as a function of hydration state determined by nanoindentation. *Philosophical Magazine*, 86:5691–5703.

[Brinell, 1900] Brinell, J. A. (1900). In *Second Cong. Int. Méthodes d'Essai*, Paris.

[Briscoe et al., 1998] Briscoe, B. J., Fiori, L., and Pelillo, E. (1998). Nanoindentation of polymeric surface. *Appl. Phys.*, 31:2395.

[Bromage et al., 2003] Bromage, T. G., Goldman, H. M., McFarlin, S. C., Warshaw, J., Boyde, A., and Riggs, C. M. (2003). Circularly polarized light standards for investigations of collagen fiber orientation in bone. *The Anatomical Record*, 274B:157–168.

[Bronzino, 2000] Bronzino, J. D. (2000). *The biomedical engineering handbook, second edition*, volume 1. CRC Press LLC.

[Bushby et al., 2004] Bushby, A. J., Ferguson, V. L., and Boyde, A. (2004). Nanoindentation of bone: Comparison of specimens tested in liquid and embedded in polymethylmethacrylate. *Journal of Materials Research*, 19(1):249–259.

[Carnelli, 2010] Carnelli, D. (2010). *Orientation and length-scale dependent mechanical properties in lamellar bone at the micro and nanostructural hierarchical levels.* PhD thesis, Politecnico di Milano.

[Carnelli et al., 2011] Carnelli, D., Lucchini, R., Ponzoni, M., Contro, R., and Vena, P. (2011). Nanoindentation testing and finite element simulations of cortical bone allowing for anisotropic elastic and inelastic mechanical response. *Journal of Biomechanics*, 44:1852–1858.

[Cheng et al., 2005] Cheng, L., Xia, X., Scriven, L. E., and W., G. W. (2005). Spherical-tip indentation of viscoelastic material. *Mechanics of Materials*, 37:213–226.

[Cheng et al., 1999] Cheng, L., Xia, X., Yu, W., Scriven, L. E., and W., G. W. (1999). Flat-punch indentation of viscoelastic material. *Journal of Polymer Science Part B: Polymer Physics*, 38(1):10–22.

[Choi et al., 1990] Choi, K., Kuhn, J. L., Ciarelli, M. J., and Goldstein, S. A. (1990). The elastic moduli of human subchondral, trabecular, and cortical bone tissue and the size-dependency of cortical bone modulus. *Journal of Biomechanics*, 23(11):1103–1113.

[Chudoba and Richter, 2001] Chudoba, T. and Richter, F. (2001). Investigation of creep behavior under load during indentation experiments and its influence on hardness and modulus results. *Surface and Coatings Technology*.

[Cowin, 1989] Cowin, S. C. (1989). *Bone Mechanics*. CRC Press.

[Cowin, 1999] Cowin, S. C. (1999). Bone poroelasticity. *Journal of Biomechanics*, 32:217–238.

[Cowin and Doty, 2007] Cowin, S. C. and Doty, S. B. (2007). *Tissue Mechanics*. Springer.

[Currey, 1964] Currey, J. (1964). Three analogies to explain the mechanical properties of bone. *Biorheol.*, 2:1–10.

[Currey, 1965] Currey, J. D. (1965). Anelasticity in bone and echinoderm skeletons. *Journal of Experimental Biology*, 43:279–292.

[Currey, 2002] Currey, J. D. (2002). *Bones: Structure and Mechanics*. Princeton and Oxford: Princeton University Press.

[Dempster and Liddicoat, 1952] Dempster, W. and Liddicoat, R. T. (1952). Compact bone as a nonisotropic material. *American Journal of Anatomy*, 91:331–362.

[Doerner and Nix, 1986] Doerner, M. F. and Nix, W. D. (1986). A method for interpreting the data from depth-sensing indentation ins t rurnen ts. *J. Mater. Res.*, 1(4).

[Donnelly et al., 2006] Donnelly, E., Baker, S. P., Boskey, A. L., and van der Meulen, M. C. (2006). Effects of surface roughness and maximum load on the mechanical properties of cancellous bone measured by nanoindentation. *Journal of Biomedical Materials Research*, 77A(2):426–435.

[Ebenstein and Pruitt, 2006] Ebenstein, D. M. and Pruitt, L. A. (2006). Nanoindentation of biological material. *Nanotoday*, 1(3):26–33.

[Erben, 1997] Erben, R. G. (1997). Embedding of bone samples in methylmethacrylate: an improved method suitable for bone histomorphometry, histochemistry, and immunohistochemistry. *The Journal of Histochemistry & Cytochemistry*, 45(2):307–313.

[Evans, 1973] Evans, F. G. (1973). *Mechanical Properties of Bone*. Thomas, Springfield.

[Evans and Lebow, 1951] Evans, F. G. and Lebow, M. (1951). Regional differences in some of the physical properties of the human femur. *Journal of Applied Physiology*, 3:563–572.

[Fan and Rho, 2003] Fan, Z. and Rho, J. Y. (2003). Effects of viscoelasticity and time-dependent plasticity on nanoindentation measurements of human cortical bone. *Journal of Biomedical Materials Research*, 67A(1):208–214.

[Feng and Ngan, 2002] Feng, G. and Ngan, A. H. W. (2002). Effects of creep and thermal drift on modulus measurement using depth-sensing indentation. *Journal of Materials Research*, 17(3):660–668.

[Feng et al., 2012] Feng, L., Chittenden, M., Schirer, J., Dickinson, M., and Jasiuk, I. (2012). Mechanical properties of porcine femoral cortical bone measured by nanoindentation. *Journal of Biomechanics*, 45:1775–1782.

[Ferry, 1980] Ferry, J. D. (1980). *Viscoelastic properties of polymers.* Wiley, New York.

[Fischer-Cripps, 2004] Fischer-Cripps, A. C. (2004). *Nanoindentation.* Mechanical Engineering Series. Springer, second edition edition.

[Fischer-Cripps, 2011] Fischer-Cripps, A. C. (2011). *Nanoindentation.* Mechanical Engineering Series. Springer, New York.

[Franzoso and Zysset, 2009] Franzoso, G. and Zysset, P. (2009). Elastic anisotropy of human cortical bone secondary osteons measured by nanoindentation. *J. Biomech. Eng.*, 131(2).

[Fratzl, 2004] Fratzl, P. (2004). *Hierarchical structure and mechanical adaptation of biological materials.* Kluwer Academic Publishers.

[Fratzl and Gupta, 2007] Fratzl, P. and Gupta, H. S. (2007). *Nanoscale mechanisms of bone deformation and fracture. Handbook of Biomineralization*, volume 1. E. Bäuerlein editor.

[Garner et al., 2000] Garner, E., Lakes, R., Lee, T., Swan, C., and Brand, R. (2000). Viscoelastic dissipation in compact bone: implications for stress-induced fluid flow in bone. *J. Biomech. Eng.*, 122:166–172.

[Gebhardt, 1906] Gebhardt, W. (1906). Uber funktionell wichtige anordnungsweisen der feineren und groberen bauelemente des wirbeltierknochens. ii. spezieller teil. l. der bau der haverssohen lamellensysteme und seine funktionelle bedeutung. *Arch. Entwickl. Mech. Org.*, 20:187–322.

[Gillham et al., 1997] Gillham, B., Wills, E. D., Papachristodoulou, D. K., and Thomas, J. H. (1997). *Will's Biochemical Basis of Medicine*. Oxford University Press.

[Giraud-Guille, 1988] Giraud-Guille, M. M. (1988). Twisted plywood architecture of collagen fibrils in human compact bone osteons. *Calcif. Tissue Int.*, 42:167–180.

[Gleeson, 2006] Gleeson, J. P. (2006). *Composition and mechanical properties of osteoarthritic subchondral trabecular tibial bone*. PhD thesis, Trinity College Dublin.

[Guidoni et al., 2010] Guidoni, G., Swain, M., and Jäger, I. (2010). Nanoindentation of wet and dry compact bone: influence of environment and indenter tip geometry on the indentation modulus. *Philosophical Magazine*, 90(5):553–565.

[Habelitz et al., 2002] Habelitz, S., Marshall, G., W., Balooch, M., and Marshall, S. J. (2002). Nanoindentation and storage of teeth. *Journal of Biomechanics*, 35(7):995–998.

[Hardin et al., 2011] Hardin, J., Bertoni, G., and Kleinsmith, L. (2011). *Becker's World of the Cell*. Pearson, 8 edition.

[Hengsberger et al., 2002] Hengsberger, S., Kulik, A., and Zysset, P. (2002). Nanoindentation discriminates the elastic properties of individual human bone lamellae under dry and physiological conditions. *Bone*, 30(1):178–184.

[Herman, 2008] Herman, I. P. (2008). *Physics of the human body*. Biological and Medical Physics, Biomedical engineering series. Springer.

[Herring, 1977] Herring, G. M. (1977). Methods for the study of the glycoproteins and proteoglycans of bone using bacterial collagenase. *Calcified Tissue Research*, 24(1):29–36.

[Hertz, 1896] Hertz, H. (1896). *Miscellaneous paper*. MacMillan, New York.

[Hoyt, 1924] Hoyt, S. L. (1924). *The ball indentation hardness test*, volume 6. Trans. Am. Soc. Steel Treating.

[Instruments, 2010] Instruments, C. (2010). *Indentation-Software manual*. CSM Instruments, Peseaux (Switzerland).

[Isaksson et al., 2010] Isaksson, H., Nagao, S., Malkiewicz, M., Julkunen, P., Nowak, R., and Jurvelin, J. S. (2010). Precision of nanoindentation protocols for measurements of viscoelasticity in cortical and trabecular bone. *Journal of Biomechanics*, 43:2410–2417.

[Katz and Yoon, 1984] Katz, J. and Yoon, H. (1984). The structure and anisotropic mechanical properties of bone. *IEEE Tans. Biomed. Eng.*, 31:878–884.

[Khurana, 2009] Khurana, J. S. (2009). *Bone Pathology*. Springer.

[Kruijer et al., 2006] Kruijer, M. P., Warnet, L. L., and Akkerman, R. (2006). Modelling of the viscoelastic behaviour of steel reinforced thermoplastic pipes. *Composites*, 37:356–367.

[Lakes, 2009] Lakes, R. (2009). *Viscoelastic materials*. Cambridge University Press.

[Lakes and Katz, 1979a] Lakes, R. S. and Katz, J. L. (1979a). Viscoelastic properties of wet cortical bone-ii. relaxation mechanisms. *J. Biomech.*, 12:679–687.

[Lakes and Katz, 1979b] Lakes, R. S. and Katz, J. L. (1979b). Viscoelastic properties of wet cortical bone-iii. a nonlinear constitutive equation. *J. Biomech.*, 12:689–698.

[Lakes et al., 1979] Lakes, R. S., Katz, J. L., and Sternstein, S. S. (1979). Viscoelastic properties of wet cortical bone-i. torsional and biaxial studies. *J. Biomech.*, 12:657–678.

[Landis et al., 1996] Landis, W. J., Hodgens, K. J., Arena, J., Song, M. J., and McEwen, B. F. (1996). Structural relations between collagen and mineral in bone as determined by high voltage electron microscopic tomography. *Microscopy Research and Technique*, 33:192–202.

[Lee and Radok, 1960] Lee, E. and Radok, J. (1960). The contact problem for viscoelastic bodies. *J. Appl. Mech.*, 27:438–444.

[Lewis and Nyman, 2008] Lewis, G. and Nyman, J. S. (2008). The use of nanoindentation for characterizing the properties of mineralized hard tissue: state-of-the art review. *Journal of Biomedical Materials Research Part B: Applied Biomaterials*, 87(1):286–301.

[Li and Bhushan, 2002] Li, X. and Bhushan, B. (2002). A review of nanoindentation continuos stiffness measurement technique and its applications. *Materials Characterization*, 48:11–36.

[Liebschner and Wettergreen, 2003] Liebschner, M. A. K. and Wettergreen, M. A. (2003). Optimization of bone scaffold engineering for load bearing applications. In Ashammakhi, N. and Ferretti, P., editors, *Topics in tissue engineering.*, chapter 22. University of Oulu.

[Manilay et al., 2012] Manilay, Z., Novitskaya, E., Sadovnikon, E., and McKittrick, J. (2012). *A comparative study of young and mature bovine cortical bone.* Acta Biomaterialia.

[Martin et al., 1998] Martin, R. B., Burr, D. B., and Sharkey, N. A. (1998). *Skeletal tissue mechanics.* Springer.

[Mase and Mase, 1999] Mase, G. T. and Mase, G. (1999). *Continuum mechanics for engineers, second edition.* CRC Press.

[McCrum et al., 1997] McCrum, N. G., Buckley, C. P., and Bucknall, C. B. (1997). *Principles of polymer engineering.* Oxford University Press, 2nd edition edition.

[Meares, 1965] Meares, P. (1965). *Polymers: Structure and bulk properties.* Van Nostrand.

[Mencík, 2012] Mencík, J. (2012). *Nanoindentation in materials science.*, chapter Uncertainties and Errors in Nanoindentation. InTech.

[Mencík et al., 2011] Mencík, J., Hong He, L., and Nemecek, J. (2011). Characterization of viscoelastic-plastic properties of solid polymers by instrumented indentation. *Polymer Testing*, 30:101–109.

[Mow and Huiskes, 2004] Mow, V. C. and Huiskes, R. (2004). *Basic orthopaedic biomechanics and machano-biology.* Lippincott Williams & Wilkins.

[Murugan and Ramakrishna, 2005] Murugan, R. and Ramakrishna, S. (2005). Development of nanocomposites for bone grafting. *Composites Science and Technology*, 65:2385–2406.

[Nikolov and Raabe, 2008] Nikolov, S. and Raabe, D. (2008). Hierarchical modeling of the elastic properties of bone at submicron scales: the role of extrafibrillar mineralization. *Biophysical Journal*, 94:4220–4232.

[Nyman et al., 2006] Nyman, J. S., Roy, A., Shen, X., Acuna, R. L., Tyler, J. H., and Wang, X. (2006). The influence of water removal on the strength and toughness of cortical bone. *J. Biomech.*, 39(5):931–938.

[Olesiak et al., 2010] Olesiak, S. E., Oyen, M. L., and Ferguson, V. L. (2010). Viscous-elastic-plastic behavior of bone using berkovich nanoindentation. *Mechanics of Time-Dependent Materials*, 14:111–124.

[Oliver and Pharr, 1992] Oliver, W. C. and Pharr, G. M. (1992). An improved technique for detrmining hardness and elastic modulus using load and displacement sensing indentation experiments. *Journal of Materials Research*, 7:1564–1583.

[Ottani et al., 2002] Ottani, V., Martini, D., Franchi, M., Ruggeri, A., and Raspanti, M. (2002). Hierarchical structure in fibrillar collagens. *Micron*, 22:587–596.

[Oyen, 2005] Oyen, M. L. (2005). Spherical indentation creep following ramp loading. *Journal of Materials Research*, 20(8):2094–2100.

[Oyen, 2006] Oyen, M. L. (2006). Analytical techniques for indentation of viscoelastic materials. *Phil. Mag.*, 86(33-35):5625–5641.

[Oyen, 2011] Oyen, M. L. (2011). *Handbook of nanoindentation: with biological application.* Pan Stanford Publishing.

[Paietta et al., 2011] Paietta, R. C., Campbell, S. E., and Ferguson, V. L. (2011). Influences of spherical tip radius, contact depth, and contact area on nanoindentation properties of bone. *Journal of Biomechanics*, 44:285–290.

[Parsamian and Norman, 2001] Parsamian, G. P. and Norman, T. L. (2001). Diffuse damage accumulation in the fracture process zone of human cortical bone specimens and its influence on fracture toughness. *Journal of Materials Science: Materials in Medicine*, 12:779–783.

[Rauber, 1876] Rauber, A. A. (1876). *Elasticitat und Festigkeit der Knochen. Anatomisch-Physiologische studie.* Engelmann, Leipzig.

[Reilly et al., 1974] Reilly, D. T., Burstein, A. H., and Frankel, V. H. (1974). The elastic modulus for bone. *Journal of Biomechanics*, 7:271–275.

[Rho et al., 1998] Rho, J., Kuhn-Spearing, L., and Zioupos, P. (1998). Mechanical properties and the hierarchical structure of bone. *Medical Engineering & Physics*, 20:92–102.

[Rho and Pharr, 1999] Rho, J. Y. and Pharr, G. M. (1999). Effects of drying on the mechanical properties of bovine femur measured by nanoindentation. *Journal of Materials Science: Materials in Medicine*, 10:485–488.

[Rho et al., 1999] Rho, J. Y., Roy II, M. E., Tsui, T. Y., and Pharr, G. M. (1999). Elastic properties of microstructural components of human bone tissue as measured by nanoindentation. *Journal of Biomedical Materials Research*, 45(1):48–54.

[Rho et al., 1997] Rho, J. Y., Tsui, T. Y., and Pharr, G. M. (1997). Elastic properties of human cortical and trabecular lamellar bone measured by nanoindentation. *Biomaterials*, 18(20):1325–1330.

[Rho et al., 2002] Rho, J. Y., Zioupos, P., Currey, J. D., and Pharr, G. M. (2002). Microstructural elasticity and regional heterogeneity in human femoral bone of various ages examined by nano-indentation. *Journal of Biomechanics*, 35:189–198.

[Sasaki, 2012] Sasaki, N. (2012). *Viscoelasticity - From theory to biological applications.*, chapter Viscoelastic properties of biological materials. Number 5. InTech.

[Sasaki et al., 2002] Sasaki, N., Tagami, A., Goto, T., Taniguchi, M., Nakata, M., and Hikichi, K. (2002). Atomic force microscopic studies on the structure of bovine femoral cortical bone at the collagen fibril-mineral level. *J. Mater. Sci. Mater. Med.*, 13:333–337.

[Scheiner et al., 2010] Scheiner, S., Théoval, A., Pivonka, P., Smith, D. W., and Bonewald, L. F. (2010). Investigation of nutrient transport mechanisms in the lacunae-canaliculi system. *Materials Science and Engineerin*, 10:012129.

[Sedlin and Hirsch, 1966] Sedlin, E. D. and Hirsch, C. (1966). Factors affecting the determination of the physical properties of femoral cortical bone. *Acta Orthopaedica Scandinavica*, 37:29–48.

[Sharpe, 2008] Sharpe, W. N. (2008). *Springer Handbook of experimental solid mechanics*. Springer.

[Sheperd et al., 2011] Sheperd, T. N., Zhang, J., Ovaert, T. C., Roeder, R. K., and Niebur, G. L. (2011). Direct comparison of nanoindentation and macroscopic measurements of bone viscoelasticity. *Journal of the Mechanical Behavior of Biomedical Materials*, 4:2055–2062.

[Smith and Walmsley, 1959] Smith, J. W. and Walmsley, R. (1959). Factors affecting the elasticity of bone. *Journal of Anatomy*, 93:503–523.

[Smith and Sandland, 1925] Smith, R. L. and Sandland, G. E. (1925). Some notes on the use of diamond pyramid for hardness testing. *J. Iron. Steel Inst.*, 3:285–301.

[Sperling, 1986] Sperling, L. H. (1986). *Interpenetrating Polymer Networks.*, volume 3 of *Encyclopedia of Materials Science and Engineering.* Pergamon Press Ltd.

[Tabor, 1951] Tabor, D. (1951). *The hardness of metals.* Clarendon Press.

[Tai et al., 2005] Tai, K., Qi, H. J., and Ortiz, C. (2005). Effect of mineral content on the nanoindentation properties and nanoscale deformation mechanisms of bovine tibial cortical bone. *Journal of Materials Science: Materials in Medicine*, 16:947–959.

[Team, 2008] Team, R. D. C. (2008). *R: A Language and Environment for Statistical Computing.* R Foundation for Statistical Computing, Vienna, Austria.

[Townsend et al., 1975] Townsend, P. R., Rose, R. M., and Radin, E. L. (1975). Buckling studies of single human trabeculae. *Journal of Biomechanics*, 8:199–201.

[Vandamme and Ulm, 2006] Vandamme, M. and Ulm, F. J. (2006). Viscoelastic solutions for conical indentation. *Int. J. Solids Struct.*, 43(10):3142–3165.

[Wang et al., 2010] Wang, X., Nyman, J. S., Dong, X., Leng, H., and Reyes, M. (2010). *Fundamental Biomechanics in Bone Tissue Engineering.* Morgan & Claypool Publishers.

[Wang et al., 2002] Wang, X. M., Cui, F. Z., Ge, J., Zhang, Y., and Ma, C. (2002). Variation of nanomechanical properties of bone by gene mutation in the zebrafish. *Biomaterials*, 23:4557–4563.

[Weiner et al., 1997] Weiner, S., Arad, T., Sabanay, I., and Traub, W. (1997). Rotated plywood structure of primary lamellar bone in the rat: orientations of the collagen fibril arrays. *Bone*, 20:509–514.

[Weiner and Price, 1986] Weiner, S. and Price, P. A. (1986). Disaggregation of bone into crystals. *Calcified Tissue International*, 39:365–375.

[Weiner and Traub, 1986] Weiner, S. and Traub, W. (1986). Organisation of hydroxyapatite crystals within collagen fibrils. *FEBS Letters*, 206(2):262–266.

[Weiner and Traub, 1989] Weiner, S. and Traub, W. (1989). Crystal size and organization in bone. *Connect Tissue Res.*, 21:259–265.

[Wolff, 1986] Wolff, J. (1986). *The law of bone remodelling.* Springer-Verlag, Berlin.

[Wu et al., 2011] Wu, Z., Ovaert, T. C., and Niebur, G. L. (2011). Viscoelastic properties of human cortical bone tissue depend on gender and elastic modulus. *Wiley Online Library.*

[Yamada and Evans, 1970] Yamada, H. and Evans, F. G. (1970). *Strength of Biological Materials.* Williams & Wilkins, Baltimore.

[Yamashita et al., 2001] Yamashita, J., Furman, B. R., Rawls, H. R., Wang, X., and Agrawal, C. M. (2001). The use of dynamic mechanical analysis to assess the viscoelastic properties of human cortical bone. *Journal of Biomedical Materials Research*, 58:47–53.

[Yamashita et al., 2002] Yamashita, J., Li, X., Furman, B. R., Rawls, H. R., Wang, X., and Agrawal, C. M. (2002). Collagen and bone viscoelasticity: a dynamic mechanical analysis. *Journal of Biomedical Materials Research*, 63:31–36.

[Zhao and Ovaert, 2010] Zhao, Y. and Ovaert, T. C. (2010). Error estimation of nanoindentation mechanical properties near a dissimilar interface via finite element analysis and analytical solution methods. *Journal of Materials Research*, 25(12):2308–2316.

[Zioupos, 2005] Zioupos, P. (2005). In vivo fatigue microcracks in human bone: material properties of the surrounding bone matrix. *European Journal of Morphology*, 42(1/2):31–41.

[Zioupos and Currey, 1998] Zioupos, P. and Currey, J. (1998). Changes in the stiffness, strength, and toughness of human cortical bone with age. *Bone*, 22(1):57–66.

[Zysset et al., 1999] Zysset, P. K., Guo, X. E., Hoffler, C. E., Moore, K. E., and Goldstein, S. A. (1999). Elastic modulus and hardness of cortical and trabecular bone lamellae measured by nanoindentation in the human femur. *Journal of Biomechanics*, 32:1005–1012.